Cu_2O Substrates and Epitaxial Cu_2O/ZnO Thin Film Heterostructures for Solar Energy Conversion

Thesis by
Davis Solomon Darvish

In Partial Fulfillment of the Requirements
for the Degree of
Doctor of Philosophy

California Institute of Technology
Pasadena, California

2013

(Defended Dec 17, 2012)

In dedication to the Sun

for without this huge spheical plasma in the center of our solar system, life would cease to exist on earth.

Fiat Lux!

יְהִי אוֹר

Let there be light!

Acknowledgements

It feels like only a couple months ago I was a senior at Cal applying to grad schools when my Dad asked if I applied to Caltech. I am thankful he brought up the topic that day because I would have surely missed the application deadline which was the end of the next day had he not said anything.

My time at Caltech has been interesting to say the least. These past years have brought many delightful surprises as well as several unexpected challenges. If it was not for each and every one of the many people who lent me a hand when I needed one I would not be here today. First and foremost I would like to thank my advisor, Professor Harry Atwater, for his guidance and support. When time came to chose a grad school to go to I wanted to pick a place and research group that I could be excited about waking up for it every day. Harry has provided a place for his grad student to excel, providing them with the tools they need to do cutting edge research and make great scientific contributions to society.

I would like to thank the US DOE for start the funding for this project my first couple years! I am forever grateful that the project was later picked up by the Dow Chemical Company which provided an extra supportive layer whether it be access to analysis and equipment that did not have or were not trained on to the informative and bi-weekly meetings.

I would like to thank the following people who had a direct impact on the technical aspect of my graduate career. Harry Atwater, Marty DeGroot, Jim Stevens, Rebekah Feist, Gregory Kimball, Mathew Dicken, Carrie Hofmann, The Dow Chemical Company, The Earth Abundant Subgroup, Atwater Research Group.

I would also like to thank all the people in my life who were there when I needed strength, courage, advice, honesty, friendship, and love. Sarah Hanna Bigle my fiancee then girlfriend, my mother and father Moez and Shahanaz Darvish, my brother Ryan Darvish, my friends since childhood Arya Tabibnia, David Yadegaran, Ramin Kohansedgh, and new friends JK, Danny Rubin, Ramin Haverim, and everyone else who made life what it was outside of Caltech.

As for what is next? I will be traveling a path I did not necessarily expect traveling only a year ago. The Portland metro area is where I will soon call home, working at Logic Technology Development at Intel, a childhood dream of mine now come true. I am extremely excited about the next chapter and can not wait to see what is in store for me.

Davis S. Darvish

Dec. 2012

Pasadena, CA

Abstract

Future fossil fuel scarcity and environmental degradation have demonstrated the need for renewable, low-carbon sources of energy to power an increasingly industrialized world. Solar energy with its infinite supply makes it an extraordinary resource that should not go unused. However with current materials, adoption is limited by cost and so a paradigm shift must occur to get everyone on the same page embracing solar technology. Cuprous Oxide (Cu_2O) is a promising earth abundant material that can be a great alternative to traditional thin-film photovoltaic materials like CIGS, CdTe, etc. We have prepared Cu_2O bulk substrates by the thermal oxidation of copper foils as well Cu_2O thin films deposited via plasma-assisted Molecular Beam Epitaxy. From preliminary Hall measurements it was determined that Cu_2O would need to be doped extrinsically. This was further confirmed by simulations of ZnO/Cu_2O hetero-junctions. A cyclic interdependence between, defect concentration / minority carrier lifetime, film thickness, and carrier concentration has been the primary reason why efficiencies well above 6-7% have not been realized. Our thin-film hetero structures may be able to kinetically control growth thus preventing the number of defects that arise as a result of the material being allowed to reach equilibrium. While the efficiencies of the cells were not high at all (most of the power lost is due to series and contact resistance which hopefully would be rectified, open circuit voltages above 500mV are very promising and show signs of progress in the right direction.

Contents

List of Figures

List of Tables

Chapter 1

Introduction

This thesis details the fabrication, characterization, and device performance of solar cells based on cuprous oxide (Cu_2O), a non-traditional semi-conductor. Chapter 1 provides an introduction to Cu_2Os discovery and details the importance of Cu_2O's use as an earth abundant, low cost, and scalable material. The chapter continues with providing a brief review of Cu_2O's properties pertinent to its use in photovoltaic applications such as crystal structure, opto-electronic properties and band stucture. Chapter 2 calculates and discusses both a detailed balance and device physics model for efficiency of a Cu_2O heterostructure solar cell. Chapter 3 investigates the epitaxial growth of high quality Cu_2O and epi-ZnO\epi-Cu_2O thin films on MgO templated and bulk substrates by plasma-enhanced molecular beam epitaxy. The chapter finishes with device design and device results. Chapter 4 reviews methods of creating bulk Cu_2O substrates, and investigates the growth of doped and undoped Cu_2O bulk substrates via thermal oxidation of copper thin films and copper foils. Finally, Chapter 5 attempts to summerize the highlights and the important findings that will help Cu_2O technology to get near or pass the 10% efficiency mark.

1.1 Cu_2O: A Brief Background of Many Firsts

Cuprous oxide (Cu_2O) is the oldest semiconductor known to man, yet until recently very little was understood about its electronic properties. Both rectifying diodes and solar cells based on Cu_2O were fabricated in the 1920's [12] and much of the data collected on these devices were used as the basis in developing the theory of semiconductors. By the 1950's Cu_2O devices slowly faded into the background as

their short minority carrier lifetime[13] and device performance could not compete with the recent advancements made in purification and doping of both silicon and germanium which allowed fabrication of devices from those two materials to be far superior than those made by Cu_2O. Cu_2O has a rich history in semiconductor physics whose research has discovered many phenomena studied today such as Bose-Einstein condensates, excitons, and phonoritons yet there are still many basic properties of this material that are not well understood or measured.

1.2 Elemental Abundance, Scalability, Toxicity and their Cost Impact on Photovoltaics

Today's natural disasters and their socioeconomic policies have made it clear that the world's dependence on oil and fossil fuels must come to end. Not only is climate change slowly killing our planet by increasing the average temperature, it is thought to also have a significant impact in the frequency and severity of many natural disasters that have occurred in our recent past. In addition, cost of fossil fuels have dramatically increased as resources have become limited due to several natural and artificial causes. Because of these reasons it is now important more than ever that the world transitions to a new source of energy; the direct source of all energy in our solar system. Not only is solar energy the most abundant source of energy on our planet, it is also the primary source of energy for our planet as the energy stored in fossil fuels at some point and time came from the sun. The sun provides 1.2×10^5 TW of energy at the earths surface, a number that is over 10,000 times the current worlds energy use. Photovoltaics allow the direct conversion of sunlight (photons) to a form of energy that we can use (electricity). Unfortunately, the energy from the sun is diffuse, thus requiring systems with a very low cost per square meter. If solar technology is to take over or at least make a big impact in our energy needs, it must be deployed at a massive scale. An estimate of the total area of photovoltaics required to completely supplant fossil fuel use in the United States is roughly ⅔'s the total area of developed urban land in the

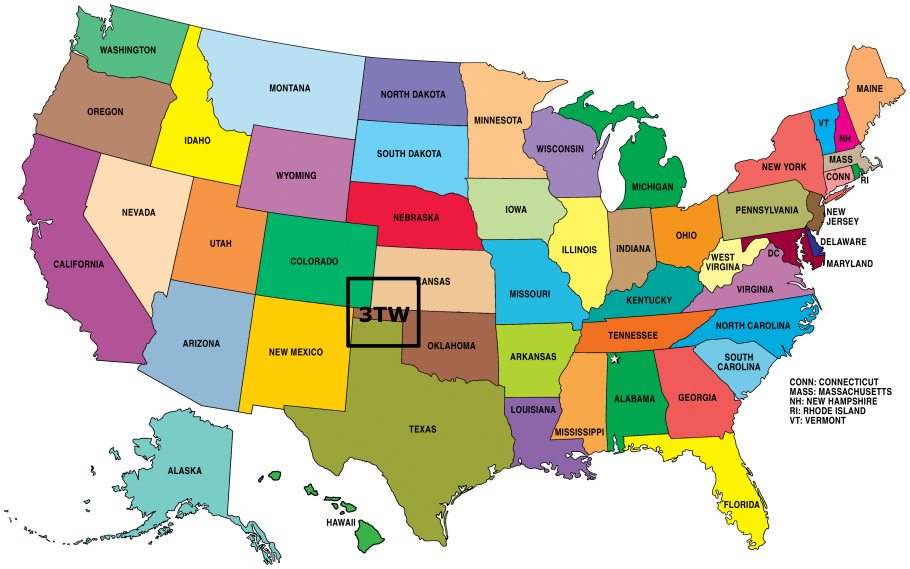

Figure 1.1. The area enclosed within the black square shows the amount of land needed for a solar energy farm to match the 3 TW of power currently used in the United States if the solar farm had an operating efficiency of only 10%.

United States. Figure 1.1 shows a map of the United States with a box outlining the area of land that needs to be covered in solar cells with 10% conversion efficiency to supply all of the United States current energy needs.For reasons of scalability it is then important that the materials chosen are both abundant in the earth's crust and also easily extractable. "Easily extractable" simply means that there are known methods or industries that extract the element needed in a cost effective manner and for its availability not to be completely dependent on the use/extraction of some other mineral or element. It is also important that the materials do not consist of any toxic elements. Solar panels have a finite lifetime before they must be thrown out and replaced. Therefore, it is advantageous to use a material that can be easily disposed of or recycled, as opposed to an environmentally unfriendly material which would have an expensive and complicated disposal protocol. Finally figure 1.2 is a plot made by the United States Geological Survey which shows the relative abundance of elements in the earths crust normalized to the abundance of Si. A line is drawn at y=1. This choice is a good approximation used to determine if terawatt scaling of photovoltaics

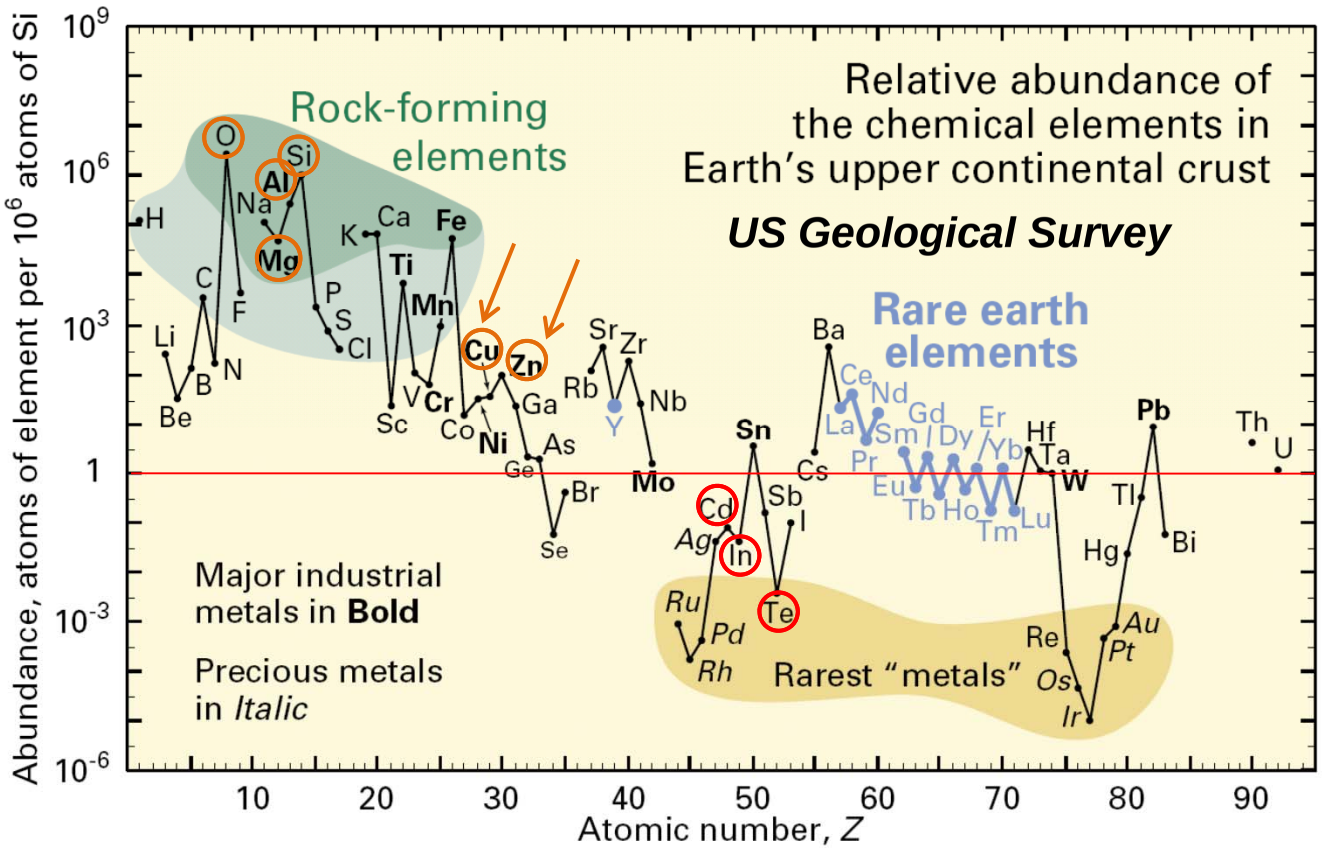

Figure 1.2. Abundance (atom fraction) of the chemical elements in Earths upper continental crust as a function of atomic number normalized to silicon.

would be possible if that element was chosen as one of the materials needed to make solar cells. Everything above the line is fine while we would like to avoid everything below it. The circled elements in the plot are in materials discussed throughout this thesis and were highlighted so that they are brought to your attention.

1.3 Cu_2O as a Photovoltaic Material

There are several important characteristics of Cu_2O that make it a great candidate for use as a solar cell. Cuprous oxides band-gap of 2.0eV [14], though not optimal (1.5eV), can convert an acceptable fraction of solar spectrum to energy when operated in a single junction configuration yielding a theoretical efficiency that is around 20%. When used as a top cell in a dual junction solar cell, its band gap is nearly ideal. Its direct band gap and optical absorption coefficients make it a suitable material for use in thin-film cells. Deposition of thin layers of any material is an important fabrication technique, especially in the photovoltaic industry where it is meant to dramatically lower costs. Its bandgap is also nearly ideal for use as photo-electrochemical cell which would be used to create hydrogen based fuels by splitting water, an important topic that needs further investigation. If it is our intention to use solar energy as our primary and only source of energy, then the excess energy produced sunlight must be stored in the form of chemical potential energy such as fuel for use in applications where a fuel is absolutely necessary.

Other less favorable characteristics of Cu_2O have prevented the realization of a Cu_2O solar cells. Several factors contribute to Cu_2O's poor showing of efficiency, which currently is only at a world record 3.89% [15]. Point defects in cuprous oxide play a dominate role in preventing the fabrication of high efficiency cells. Copper vacancies are the main mechanism by which Cu_2Os p-type conductivity is observed. In addition Cu_2O is a self-compensating semiconductor. Self-compensation is a process that occurs when the free energy of formation for point defects varies linearly with the Fermi level. As a result of this phenomena, an increase in the concentration of donor impurities lowers the free energy of formation of acceptors, thus it is always

more favorable to have more acceptors than donors. The inability to dope Cu_2O n-type means that there likely will not be a way to fabricate homojunctions with rectifying behavior and thus attention must be turned to Cu_2O Schottky junctions or semiconductor heterojunction. Specifically considering Cu_2O solar cells, the general consens is that a heterojunction will not out perform its homojunction counterpart. This is due to many reason including differences in the energy band alignment between Cu_2O and its heterojunction partner, which manifests itself as loss in the open-circuit potential. An idealized view of band offsets, known as the Anderson rule, states that the conduction band offset depends only on the electron affinity difference between the two semiconductors. Anderson's idealized model also ignores the quantum size effect, defect states and other perturbations, which in many cases do affect the bandstructure model quite a bit. In addition, the junction is now a non-continuous interface, which causes carrier recombination and loss of current. These point defects also present another problem which has to do with minority carrier lifetime of the material. It is typically desirable to increase the doping of a semiconductor which increases the the open circuit voltage via the relation:

$$V_{oc} = \frac{kT}{q} ln(\frac{((N_A + \Delta n)\Delta n)}{n_i^2}). \tag{1.1}$$

In the case of Cu_2O, that is not the case as its conductivity is dominated by copper vacancies, whose acceptor levels are much greater than traditional shallow acceptor energy levels within the bandgap, essentially destroying the minority carrier lifetime as doping increases.

1.4 Cu_2O: A Review of Properties

The remaining sections of this chapter will focus on properties and growth/synthesis of Cu_2O. We will first review physical properties of Cu_2O as a bulk material, synthesized at equilibrium or near equilibrium conditions as it pertains to its use as a photovoltaic material. Immediately proceeding will be a review of growth methods.

1.4.1 Crystal Structure

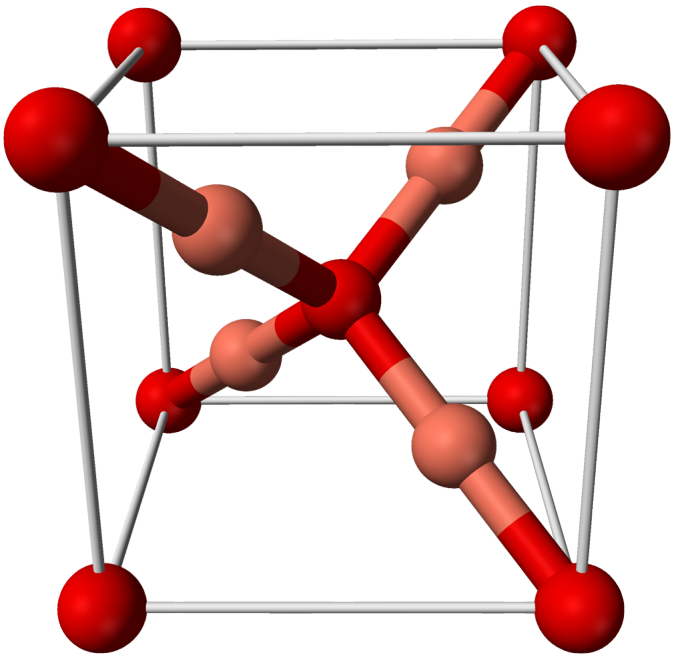

Figure 1.3. Representation of the simple cubic crystal structure of Cu_2O with the red spheres correspond to oxygen atoms and the pink spheres correspond to copper atoms.

Cu_2Os crystal structure has 2 molecules (i.e. 6 atoms) in its simple cubic unit cell which crystallizes in a structure known as cuprite shown in Figure 1.3. It has the symmetry of the 224th space group (O_h^4, $Pn\overline{3}m$). If an oxygen atom is chosen to be at the origin, the structure can then be thought of as a bcc oxygen sub-lattice interpenetrating a fcc copper sub-lattice that has been translated by $a(\frac{1}{4}, \frac{1}{4}, \frac{1}{4})$, where a is the unit cell lattice constant. The only other compounds with the same structure are Pb_2O, Ag_2O, $Cd(CN)_2$, and $Zn(CN)_2$ with the cyanides being anti-structures [16].

Based upon x-ray diffraction studies using a Cu Kα radiation source, the lattice constant was determined to be $a = 4.27$Å and bond lengths based on d-spacings as $d_{\text{Cu-O}}$=2.85Å, $d_{\text{O-O}}$=3.68Å, and $d_{\text{Cu-Cu}}$=3.02Å[11, 17]. By simple calculation, the density of the material is ρ=6.10 g/cm^3, which agrees with our experimentally calculated values[18] as well as others [17]. Using Bragg's law, one can then determine

the h,k,l values that satisfy the equation's conditions such that Bragg peaks exist. A table of the Miller indices as well as d-spacing, and 2θ, are calculated and are consistent with the observed peaks seen experimentally listed in Table [11].

Table 1.1. ICSD powder diffraction table for Cu_2O based off the data collected by M.L. Foo et al. [11]

h	k	l	2θ	d	Mult	Intensity
1	1	0	29.60	3.0176	12	41.4
1	1	1	36.47	2.4639	8	1000.0
2	0	0	42.36	2.1338	6	382.0
2	1	1	52.52	1.7422	24	10.9
2	2	0	61.45	1.5088	12	358.9
2	2	1	65.63	1.4225	24	0.0
3	1	0	69.67	1.3495	24	3.5
3	1	1	73.61	1.2867	24	329.2
2	2	2	77.48	1.2320	8	77.6
3	2	1	85.05	1.1406	48	3.4

Note: The lattice constant and crystal structure data tabulated by us and other sources used Cu Kα radiation and collected a powder diffraction spectra in the $\theta/2\theta$ mode.

Finally we will note that like many other materials, when Cu_2O is subject to extreme pressures the crystal structure undergoes a phase change to a hexagonal crystal structure [17].

1.4.2 Optoelectronic Properties and Electronic Band Structure

While Cu_2Os band gap may not be ideal for a single junction solar cell it certainly has potential as top subcell in multijunciton solar cell or as a photocathode in splitting water. The electrical potential of a cell as well as many other properties are related

to its band gap and band structure. An extremely oversimplified understanding of semiconductor band structures could be understood from the vibrational modes of atoms in a lattice known as phonons. Phonons play an important role as they provide the means for energy to transfer via a change in momentum. A a very basic quantum mechanical treatment of the band structure is necessary in order to fully understand what is going on. The Bloch theorem uses the fact that the Bravais lattice of a material is a periodic potential of many electron wave functions, which then can be written in the form of a plane wave, multiplied by a function with the periodicity of the lattice for all lattice vectors $\mathbf{R}$:

$$\psi_{n,k}(\mathbf{r}) = e^{i\mathbf{k}\bullet\mathbf{r}} u_{n,k}(\mathbf{r}) \text{ with } u_{n,k}(\mathbf{r}+\mathbf{R}) = u_{n,k}(\mathbf{r}) \tag{1.2}$$

The wave vector $\mathbf{k}$ is then used to solve the Eigenvalue problem:

$$H_k u_k(\mathbf{r}) = E_n(\mathbf{k}) u_k(\mathbf{r}) \tag{1.3}$$

This E vs. $\mathbf{k}$ relationship, also known as the dispersion relation or band structure and for each quantum number n, there exists a set of electronic levels specified by $E_n(\mathbf{k})$ which is called the band structure. Using information about the degeneracy of the valance and conduction band spatial wave functions, along with measured photoluminescence (PL) spectra of exciton emission, [9, 19, 20] one can construct the electronic band structure of Cu_2O at the Brillouin zone (gamma point) as seen in Figure 1.4. The measured band gap E_g=2.17eV at 4.2 K is obtained as the limit of the yellow exciton series[21]. Using first principles band structure methods, theorists develop computational models to calculate the electronic band structure. One of the more popular models known as the local density approximation (LDA) [22, 23], does a fair job of calculating the semirelativistic electronic band structure for Cu_2O except for the calculated band gap which is smaller than the experimental value. However, the error in the calculation of the band gap is a known flaw of this model. The correct band

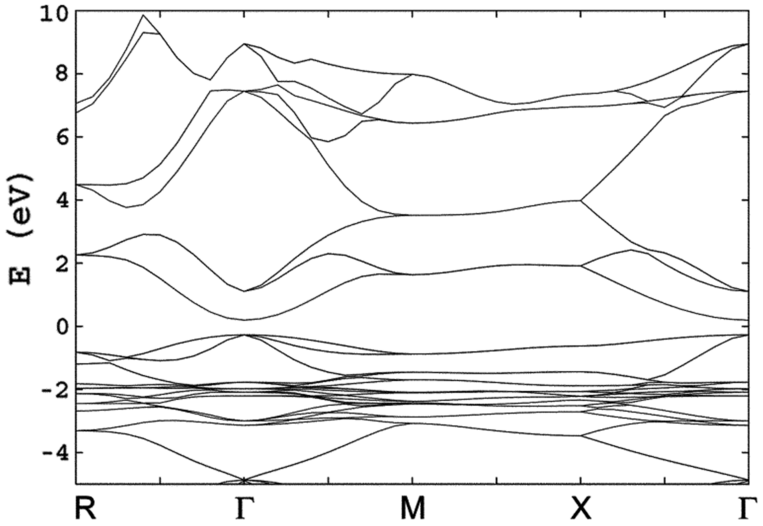

Figure 1.5. Calculated semirelativistic electronic band structure for Cu_2O which underestimates the band gap by downward shift of 1.5eV[9].

structure can be obtained simply by shifting all the conduction bands upward (in this case by 1.5eV) to correct the error[9]. Figure 1.5 shows the calculated band structure using LDA. In order to obtain the corrected band structure, the conductions bands simply need to be shifted upward by 1.5eV, such that the fundamental direct band gap at the center of the Brillouin zone is equal to the experimentally measured value of the band gap. The band structure brings crucial insight about the optoelectronic properties.

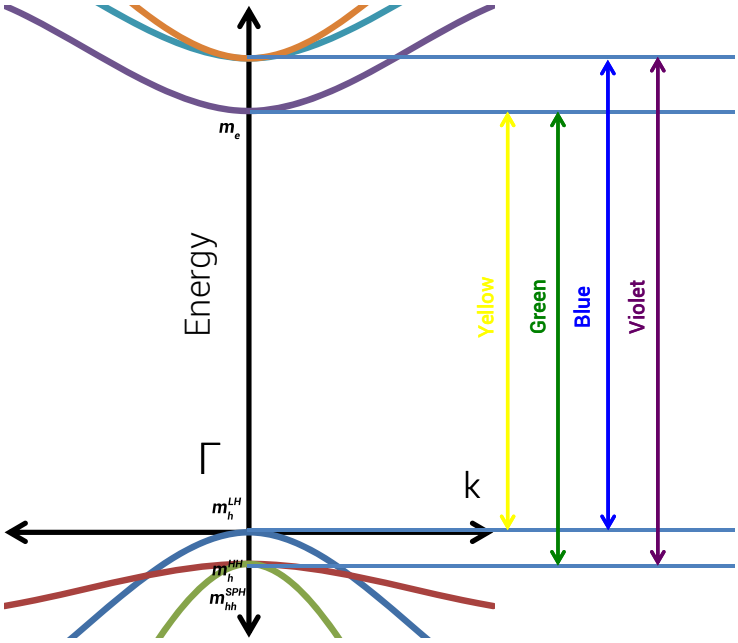

Figure 1.4. Band structure of Cu_2O near the Γ point labeld with the transitions that give rise to the 4 exciton series.

As a result of the band structure calculation, we already know that Cu_2O is a direct gap semiconductor and thus an electrons probobility of transition from the valence band to conduction band does not require a substantial change in the electron's momentum **k**, unlike indirect band gap semiconductors, which would require the absorption or emission of a phonon, making the absorption process of a indirect semiconductor much less likely to occur. The main advantage of a direct band gap semiconductor is that the incident light can be absorbed in the few microns of thickness, whereas several hundred microns of material is required for the absorption of all the

light in the indirect band gap semiconductor.

Two other important material properties can be extracted from the electronic band structure. The first property is known as the effective mass of the charged carrier, and the second is known as the mobility of the charged carrier, which is a function of the effective mass by the equation:

$$\mu = \frac{q\tau}{m^*} \tag{1.4}$$

The two can easily be solved for by using equation 1.3, the solution to the Eigen value problem, as well as Newton's second law of motion

$$F = ma = \frac{dv}{dt} \tag{1.5}$$

$$F = \frac{dp}{dt} = \frac{\hbar k}{dt} \tag{1.6}$$

and solving for m^* yields

$$m^* = \frac{\hbar^2}{(\frac{d^2E}{dk^2})} \tag{1.7}$$

where the quantity $(\frac{d^2E}{dk^2})$ is the curvature of the band. Thus highly parabolic curves indicate smaller effective mass for the charge carriers, hence high mobility. High mobility may as well be a requirement in the case of indirect gap semiconductors where the charged carriers must travel a long distance through the thickness of the material to be collected before they recombine. The likelihood for carriers to recombine is expressed in terms of either minority carrier diffusion length L_D or minority carrier lifetime τ_r ($L_D = \sqrt{D\tau_r}$) where diffusivity of the charge carriers D is related to mobility through the Nernst-Einstein relation:

$$D = \frac{k_b T \mu}{e^-}. \tag{1.8}$$

Minority carrier properties reported for Cu_2O are quite good and allow for high quantum efficiency yields, an important figure of merit needed for practical solar conversion. Diffusion lengths have been measured to be greater than 5μm, which is greater than the optical absorption depth. The valence and conduction bands in Figure 1.4 are labeled with their respective effective mass, where LH is light hole, HH is heavy hole, and SPH is Split-off hole. The effective masses of the free carriers are measured by cyclotronic resonance to be m_e=.99, m_h=.58 expressed in units of the free electron mass m_o[24].There is no experimental data for electron mobility in Cu_2O simply because the lack of n-type Cu_2O prohibits the experiment to be done. However, there is plenty of experimental data measuring the mobility of holes. Typical values range between 10-100 $\frac{cm^2}{V \cdot sec}$[25, 26, 27]which spans an order of magnitude, and often times gives a clue as to what process or processes are contributing to hole scattering, resulting in lower quality material[28]. Masumi et al.[29] conducted temperature dependent Hall measurements. As the temperature is lowered in a crystal, thermalized vibrations (phonons) start to freeze out and if the temperature is low enough, the mobility eventually becomes constant and no longer varies with temperature, and the only scattering process is due to neutral impurities. An interesting relation can be derived by knowing the the mobility of charge carriers when the only scattering mechanism is by neutral defects by using equation 1.4, and substituting in for τ, which is a function of carrier concentration. After a few simple substitutions it can be shown that

$$N_{defect} = \frac{1}{20 a_{def} \hbar \mu}. \tag{1.9}$$

A surprising result of this derivation is that it not only gives an estimate for defect concentration knowing the mobility, but the expression is independent of temperature. This result, along with the substitutions used to obtain it, will later be used in the following chapter, 2, where crystal defects, scattering cross sections, and defect densities are inputs into our device physics model.

1.4.3 Copper-Oxygen Equilibrium Phase Diagram

The copper-oxygen system naturally exists in only two chemical compounds known as Cu_2O (cuprite, κ) and CuO (Tenorite, τ) [30].

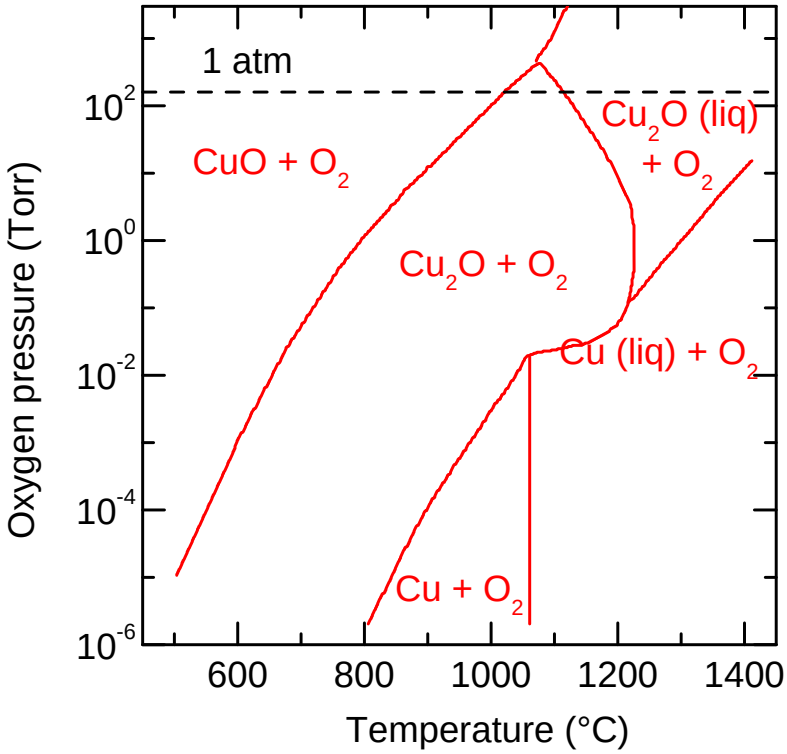

Figure 1.6. $P(O_2)$-T phase diagram for the Cu-O compound phases.

The copper-oxygen binary phase diagram is shown in Figure 1.6 as a function of temperature and the partial pressure of oxygen $P(O_2)$. The other important regions of the phase diagram are the areas to the right and left of Cu_2O. There are obvious difference between copper metal, Cu_2O, CuO and although phase space can be controlled to select Cu_2O, the conditions necessary to make Cu_2O an attractive material to synthesize border near these other phases. In particular, it is preferable to synthesize Cu_2O at 1 atm. Because of this, similar conditions can result in a mixture of the three different phases, which is not only undesirable, but often times difficult or impossible to remove in subsequent processing steps. Note that the phase diagram suggests that at one atmosphere, Cu_2O is thermodynamically stable only in

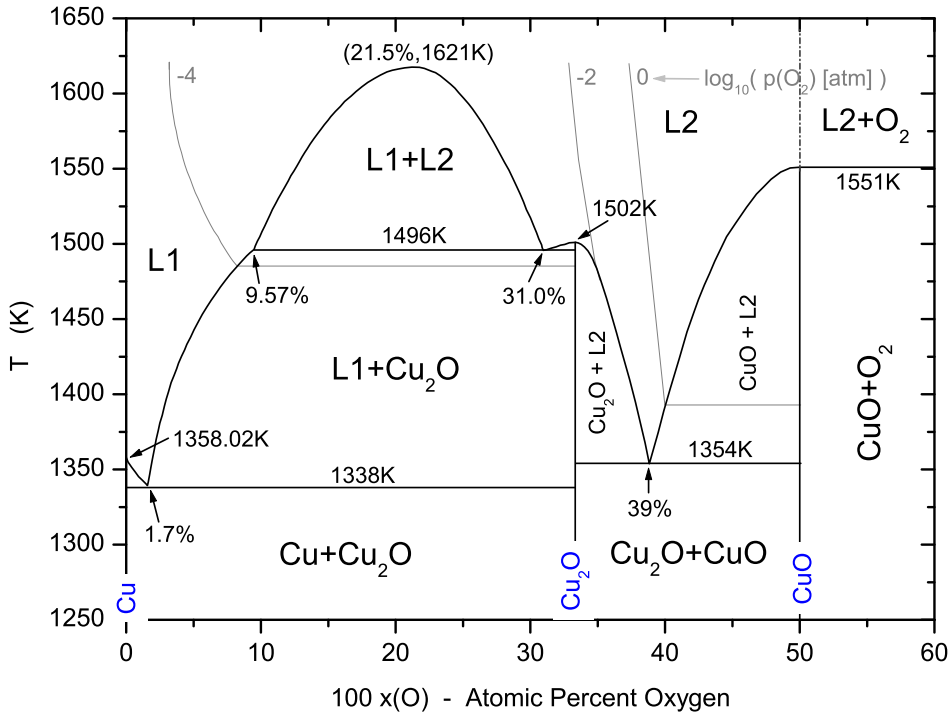

Figure 1.7. T-at% O Binary phase diagram after [31]

a small temperature range near 1025 °C. However, because of slow reaction kinetics, the phase transformation of Cu_2O to CuO at room temperature is virtually non existent, and Cu_2O is considered meta-stable as a bulk material. Observation of the p-T phase diagram tells us that there exists a large window of temperatures and pressures at which one could produce Cu_2O. This unfortunately does not translate in the practicality during crystal growth of the material. The temperature and pressure at which processing occurs has profound impacts on both its structural and electronic properties. Most of the properties of Cu_2O are determined by the conditions at which the material is processed. The area bounded within the Cu_2O+O_2 region of Figure 1.6 is of course all pure phase Cu_2O, but small deviations from stoichiometry exist, depending on where the material in that region was fabricated. Knowing information about the materials stoichiometry and conductivity as a function of the oxygen partial pressure and temperature, are important to identify the dominate defects in the material.

Very basic knowledge of inorganic chemistry explains that cations have multiple

oxidation states and because the existence of a material with higher oxidation number exists Cu(II), the oxide has the tendency to be more cation deficient and thus brings about a deviation from equilibrium. These deviations from equilibrium impose the condition for other atoms to rearrange from their previous positions in order for the system to minimize its chemical potential / Gibbs free energy (ΔG). Atoms that have moved from their ideal position introduce two defects, one at their new location and one at where they were supposed to be and these are refered to as point defects. Point defects are defects that occur only at or around a single lattice point and are not extended in space in any dimension. Special notation is used to describe the different type of point defects and some have been named after those who discovered them. There three basic types of point defect and a few different defect complexes are as follows:

- Vacancies are lattice sites in the crystal where one would expect an atom in a defect-free perfect crystal but the atom is not there.
- Interstitial defects are atoms that occupy space in the crystal lattice where usually there is no atom. They are high energy configurations and often times tend to be atoms with small Bohr radii so they may fit in the space in between atoms in their normal crystal lattice sites without introducing an unreasonable amount of strain to the lattice.
- Defect complexes and pairs, which are some combination of the three point defects described above. These include anti-site defects, Frenkel defect (a nearby pair of a vacancy and an interstitial), etc.

We introduce the following notation used throughout the thesis to represent a particular type of point defect. Using A_y^x as a generic example, A is the symbol that identifies the nature of the defect, the subscript y describes the location of the point defect, and the superscript x describes the electrical charge of the defect with respect to the ideal crystal. The most common point defect observed in Cu_2O is V_{Cu}^0, which is a Cu vacancy. There are seven possible point defects or complexes that exist for pure Cu_2O

at thermodynamic equilibrium. $V_{Cu}, V_O, Cu_i, O_i, (2V_{Cu} - V_O), (V_{Cu} - Cu_i), (V_O - O_i)$ with the latter three being non stoichiometrical defects. Using the stoichiometry equation for our compound $Cu_{2\text{-}y}O$ in equation: 1.10 , in addition to the law of mass action and neutrality conditions at equilibrium the concentration of the seven point defects mentioned above can be calculated and mapped out on top of a phase diagram, giving insight to the types of defects that can be expected for a sample processed in a particular way. Experimentalist have devised several different methods for determining

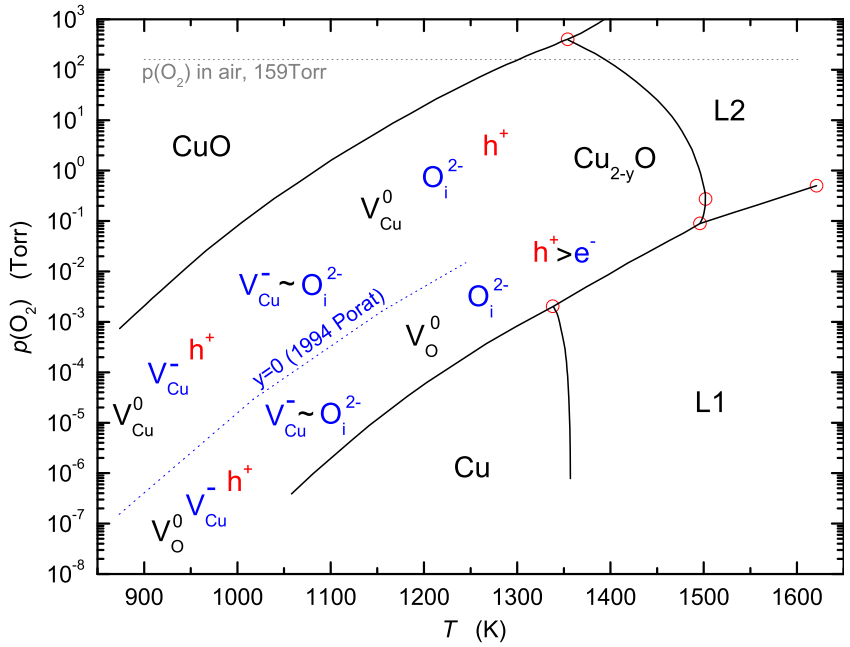

Figure 1.8. Binary phase diagram overlayed with map of predominate point defects that form at equilibrium[10].

the deviation from stoichiometry and while their data can all be expressed using the same best-fit equation, the constant used in their fit vary quite a bit, thus leading to the speculation that the variation from stoichiometry is greatly influenced by the grain size of the samples they were making [32, 33].

$$y = 2 - \frac{[Cu]}{[O]} \qquad -\infty \leq y \leq 2 \tag{1.10}$$

It was observed that the variation in y was much greater in smaller grained samples compared to larger grain samples and there as a limit at witch grain size no longer

play a role. This confirms suspicions that there are a higher density of defects at grain boundaries. Of course method of growth, kinetics, and equilibrium play a big role in determining the final microstructure of the material. A review of oxidation kinetics was conducted by Yongfu Zhu et. al. [34] and the following conclusions where made:

- The rate determining step in the oxidation of copper is the outward diffusion of Cu.
- Lattice diffusion contributes to high temperature diffusion while at low temperatures grain boundaries do. In the intermediate temperature range it is somewhat of an equal contribution.
- Impurities play an important role of impeding growth because at high temperatures they slow down the diffusion of Cu, while at lower temperatures they impede the diffusion of atoms through the grain boundaries; this is where they tend to segregate, thus only enhancing a small intermediate temperature range between the two.

It is extremely important that one understands defects and their capabilities in Cu_2O as they can be both detrimental and beneficial. As previously mentioned, attempts at doping Cu_2O n-type has been futile. Though there are a handful of reports claiming successfully doping Cu_2O n-type, the source of n-type doping and voltage observed in their measurements remain controversial[35]. The fact that n-type doping has yet to be achieved successfully is no surprise. The free energy of formation ΔG can be calculated for each defect using the either experimental or theoretical values of both enthalpies and entropies. Soon et al.[36] used density functional theory (DFT) to theoretically calculate these values.

Figure 1.4.3 shows their calculation for the free energy of formations under both copper-rich and oxygen-rich conditions. The figure shows that the copper vacancy has the lowest formation energy under both copper-rich and oxygen-rich conditions. The copper vacancy acts as a moderately shallow electron acceptor and accounts for Cu_2Os intrinsic p-type semiconductivity. Another important observation is that the

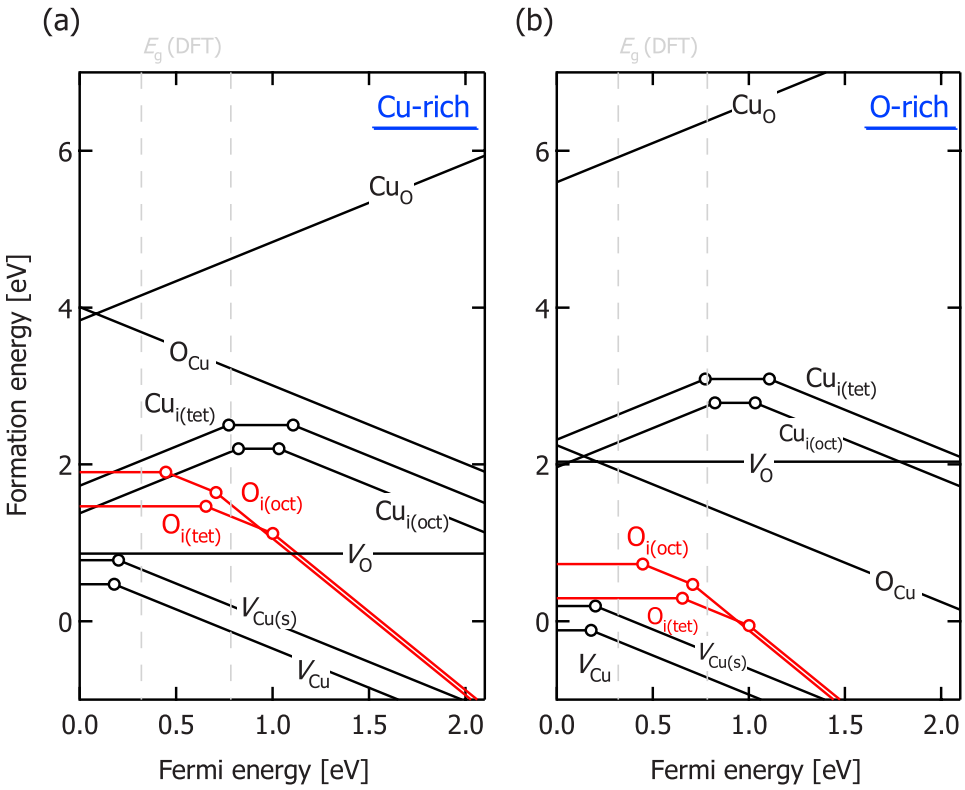

Figure 1.9. A 48 atom super-cell with native defects to calculate defect formation energies as a function of Fermi level for both a)copper-rich and b) oxygen-rich conditions.

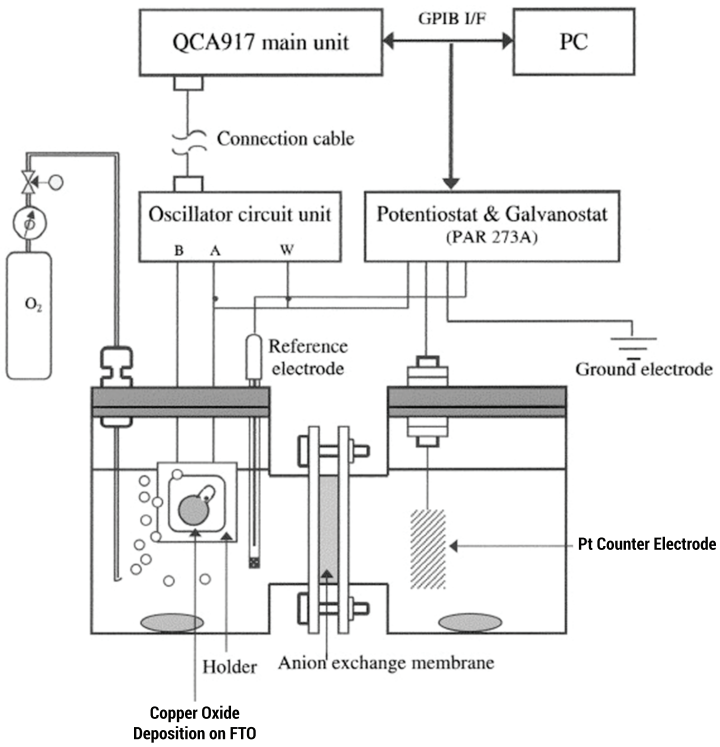

Figure 1.10. A schematic of a typical setup used for electrochemical deposition.

formation energy of charged defects varies linearly with the Fermi level and as the Fermi-level nears 1eV (around the where the oxygen vacancy defect energy lies in the bandgap) the free energy of formation for creating copper vacancies is now zero or negative which means the crystal prefers, because of both entropy and enthalpy, to compensate the increasing fermi-level. This is what is meant by "self-compensation" and is the basis for intrinsic doping in Cu_2O. A more detail discussion of Cu_2O doping will continue in Chapter 4.

1.4.4 Review of Growth Methods and Cu_2O Heterojunctions.

The growth of synthetic Cu_2O has been done using several methods, though mainly by oxidation of copper in a furnace [37, 38, 39], by electrodeposition [40, 41], and sputtering[42, 43]. More specialized techniques for both growth and purification such as hydrothermal growth[44], floating zone[24] are also used but often times are too

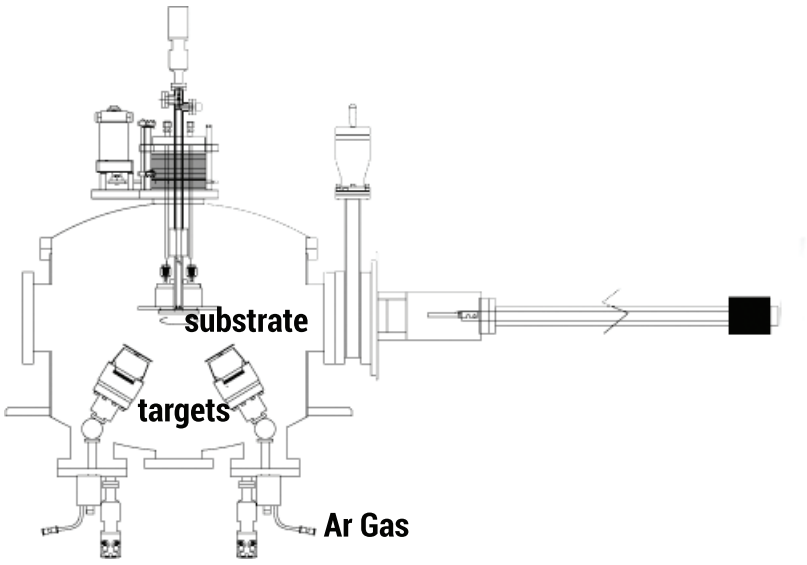

Figure 1.11. Cross sectional view of inside a sputtering chamber.

complex and do not yield results significantly different than the methods mentioned above. Of the three most popular growth methods, we will review electrodeposition and RF-Sputtering in this section. The review and discussion of Cu_2O grown by thermal oxidation will be deferred to Chapter 4. Electrodeposition is a deposition technique used for well over a couple hundred years with a variety of different materials. It has the advantages of low cost of operation and source material. It also has the advantage of being a low temperature non vacuum technique. It is versatile in the sense that it can be done via both anodic oxidation of a copper sheet or cathodic reduction of a copper salt solution[40, 41]. Unfortunately, Cu_2O solar cells fabricated by Electrodeposition have not shown much promise in terms of their efficiencies because the technique generally does not offer control of orientation and epitaxial growth. In addition, the surface roughness becomes a big problem for films that are thicker than several hundred nanometers, thus creating interface issues at both the heterojunction and surface of the solar cell. For those reasons, efficiencies greater than .5% have not been realized [45].

Reactive Sputtering or RF sputtering are two similar techniques used to make thin films of Cu_2O on a substrate. Reactive sputtering uses a Cu metal target as the source material, and that material reacts with oxygen that is leaked into the chamber

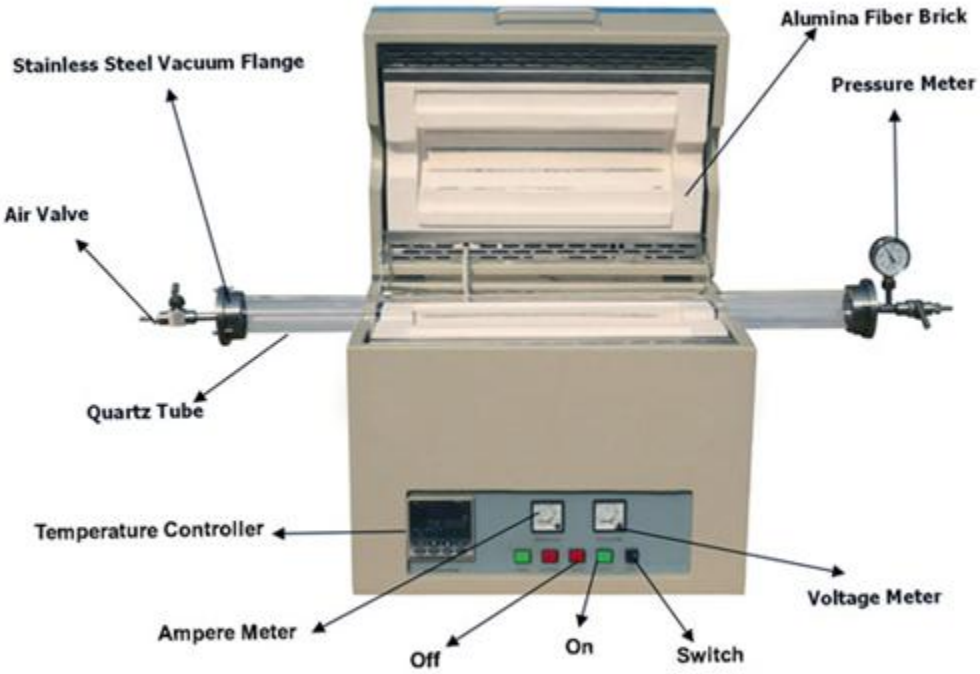

Figure 1.12. This figure illustrates the typical setup of a commercially available vacuum furnace setup. It is quite possibly the easiest, fastest, and cheapest method of fabricating Cu_2.

to create Cu_2O thin films. RF sputtering uses a Cu_2O target instead of a Cu target. The use of a radio frequency (RF) generator is essential to maintain the discharge and to avoid charge buildup when sputtering semiconducting or insulating materials such as Cu_2O. The sputtering process consists of initiating a glow discharge in the vacuum chamber under pressure controlled gas.

The glow discharge consists of partially ionized gas ions, electrons and neutral species.The ions are then accelerated at very high voltages to the target material where they bombard the target and eject atoms from the source, which then go across the chamber and nucleates on the substrate. Since process is conducted in vacuum,

control of the crystal orientation, growth rate, and whether the films growth was kinetically controlled or thermodynamically controlled. One of the biggest advantages sputtering has over the previous technique, is the species of gas and their partial pressure are all completely controlled by the user. Unfortunately, there are a few serious problems with sputtering, and one must make sure to design their experiments such that they minimize their effect. Because atoms are being accelerated at high speeds, there is the potential that they will damage the surface of the sample. More importantly, any atoms that are in the discharge area have the potential of being incorporated into your film via ion implantation. While both of these methods would be wonderful if they could be implemented in commercial manufacturing, their current state of progress makes it not vary likely. Using new age scientific tools and fabrication techniques we hope to progress the field in understand the fundamental issues that prevent higher efficiency cells. Two of the chapters in the remainder of this thesis will focus on growth of Cu_2O using two additional techniques which have already shown the prospect of great progress in this field.

Chapter 2

Detailed Balance Efficiency and Band Transport Model for ZnO/Cu_2O Solar Cells

This chapter explores two different modeling techniques for determining the efficiency of a copper oxide heterojunction solar cell in order to determine if there is sufficient opportunity for efficiency improvements over existing devices, or if there is any way to enhance the efficiency of an existing device by coupling it with a Cu_2O solar cell. This first half of this chapter introduces detailed balance efficiency modeling, which is also known as the thermodynamic efficiency limit of solar cell, for both a single-junction and doubled junction cell. The second half of this chapter will focus on a band transport model for a ZnO/Cu_2O heterojunction solar cell. While both models calculate the efficiency for a Cu_2O solar cell, the detailed balance model gives the theoretical maximum or asymptotic limit of efficiency for an ideal cell, while the device physics model calculates an efficiency for realistic cell and is great for determining the suitability of various real materials . Details of each model will be outlined in their respective sections.

2.1 Detailed Balance Model for a Cu_2O Solar Absorber

The detailed balance limit, also known as the Shockley-Queisser limit[46], is a technique used to calculate the efficiency of a photovoltaic cell. This method was proposed by Shockley and Queisser in 1961. The model is an excellent tool for gauging the promise

of different solar materials and is valuable in assessing if further optimization of a given cell is beneficial given the cost and time as one approaches the asymptotic efficiency limited. Efficiency limits of a solar cell can be calculated either by thermodynamic or by detailed balance approaches. These approaches are equivalent, but the detailed balance model allows the calculation to be made without explicit calculation of entropies by making the following fundamental assumptions:

- All recombination of carriers occurs radiatively. There are no recombination centers such that the minority carrier lifetime is infinite.
- The radiation is non-thermal with a chemical potential that is equal to the separation of the quasi-Fermi energy levels, also known as the voltage of the cell.
- The number of photons absorbed by the cell must be equivalent to the number of photons that are re-emitted through the radiative recombination process, plus the number of electron-hole pairs extracted from the cell.

The original model only accounted for a single-junction cell and one sun. A modified version of the detailed balance method presented by C. Henry in 1980[47], extends the model to include efficiency calculations for multijunction/tandem cells and concentrator cells (i.e. more than one sun). The efficiency of a solar cell is calculated by dividing the power extracted from the cell by the integrated power of the solar spectrum incident up on the cell.

$$\eta = \frac{J(V) \cdot V}{P} \tag{2.1}$$

Where, V is the operating voltage of the cell and $J(V)$ is the current density generated by the solar cell as a function of operating voltage. For the work presented in this section, the measured solar spectra for AM 1.5, as measured by the National Renewable Energy Laboratory will be used (figure reffig:am1.5) as opposed to the sun's black a body spectrum originally used by Shockley and Queisser. This spectrum takes into account absorption of photons in the atmosphere before they are incident upon the solar cell surface. Using the spectra, the number of photons arriving in the cell can be

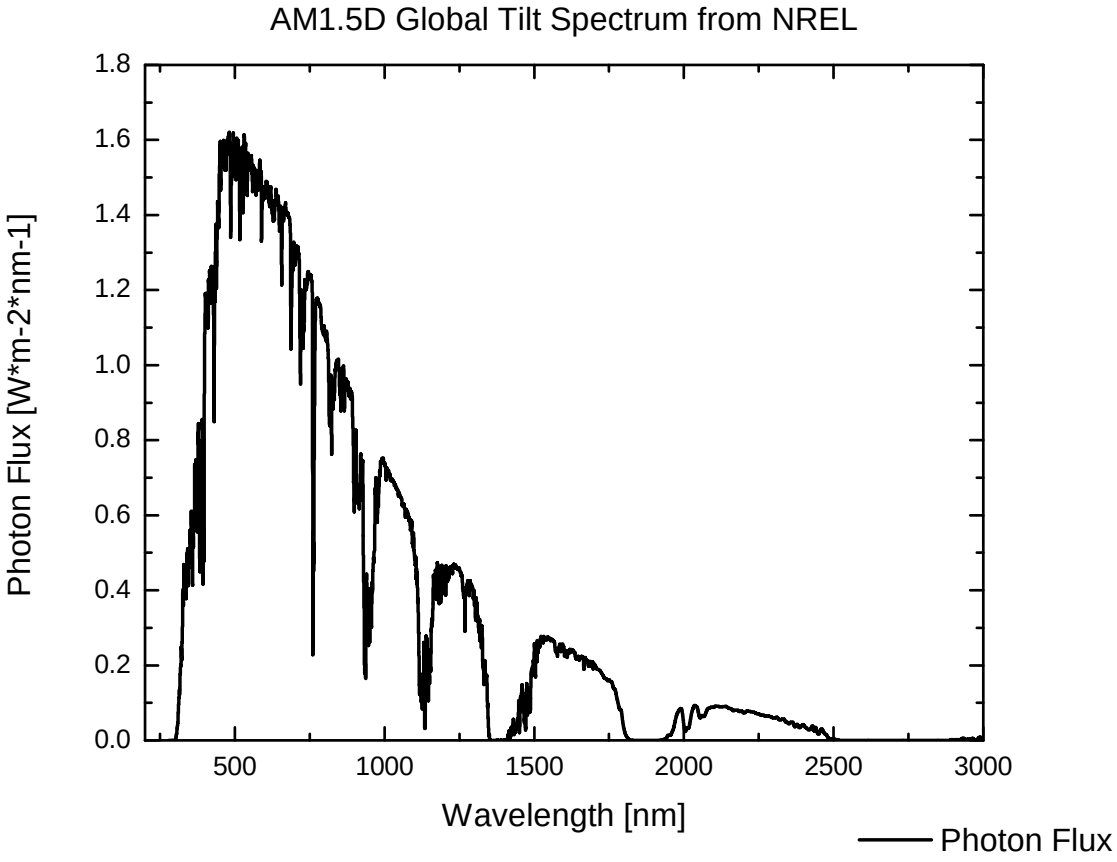

Figure 2.1. NREL's AM1.5D golbal tilt solar spectrum used in the calculation of the detailed balance efficiency

determined as a function of energy, thus a generation profile and number of carriers generated by solar illumination is given by

$$^{AM1.5}N(E_g, \infty, C) = C \sum_{E=E_g}^{\infty} \rho(E)\Delta(E) \tag{2.2}$$

where,

E_g = the band gap of the cell.

C= The concentration of the incident solar spectrum.

$\rho(E)\Delta(E)$ = the number of photons per delta unit energy for the AM1.5 spectrum.

The number of carriers lost due to radiative recombination is given by the generalization of Kirchoff's law for selective photon emission in the equation below

$$^{rad}N(E_g, \infty, T, V, \epsilon) = \frac{\epsilon}{4\pi^3\hbar^3c^2} \int_{E_G}^{\infty} \{(\hbar\omega)^2[\exp \frac{\hbar\omega - qV}{kT} - 1]^{-1}\} d\hbar\omega \tag{2.3}$$

where,

T = the operating temperature of the cell.

V= the operating voltage of the cell.

$\epsilon = \pi n^2 sin^2(\theta_c)$ a factor which characterizes how "spread out" light is in area and angle known as the ètendue.

θ_c=the critical angle for emission to a medium of a different refractive index.

thus for a single-junction cell the operating current is

$$\frac{J}{q} = ^{AM1.5} N(E_g, \infty, C) - ^{rad}N(E_G, \infty, T, V, \epsilon) \tag{2.4}$$

and thus the efficiency can be calculated using equation 2.1. The ètendue is an important factor that describes how light leaves the cell once radiative recombination takes place. When calculating the detailed balance efficiency, it is important to calculate the ètendue correctly by carefully considering the geometry that is going to be simulated. For example, a thin single-junction cell on a low-index support substrate would require that the emission from the back surface into the cell be altered by the critical angle for emission into the support material. Using an approximate value of 2 for the refractive index of a typical low index substrate material (MgO, glass, sapphire) the ètendue for the back surface is calculated to be 4π; a significant reduction when compared to a thin single junction on a thick substrate which can have a ètendue of 12π. This information is used to not only optimize efficiency, but also to lower the cost of the cell itself. The cost of the main absorber materials can be nearly cut in half by having to use less material as an optimized back surface would likely be a light reflector (a mirror), essentially causing any light to be refelect back into the cell and thus effectively doubling the material thickness. This engineering design is one many designs that tries to confine light within the cell in a technique known as light trapping. Of course the ètendue is just as important in multijunction solar cell calculations, as its value (a function of index matching the different layers) will determine how many photons with energy less than the band gap of the top cell in the tandem will be able to be absorbed in the lower layer. Because of Cu_2Os high band gap it will always be considered the top cell in a two or three-junction solar cell. It is important to note that the distribution of power in the solar spectrum is broad, and cannot be efficiently harnessed using a single band gap cell. the work being presented is not intended to displace any present and mature technology such as Si, but to possibly supplement and enhance it. Using the work of prior group member Brendan Kayes as reference, Matlab code for a detailed balance model of a single and dual-junction Cu_2O solar cell was written. The generic code for the model is located in A. Using the simulation program in Matlab, we calculate the detailed balance efficiency for a Cu_2O/ZnO on MgO substrate single junction cell to be 22%. For comparison the calculated detailed balance efficiency for a silicon single junction cell is 29.17% which is in agreement

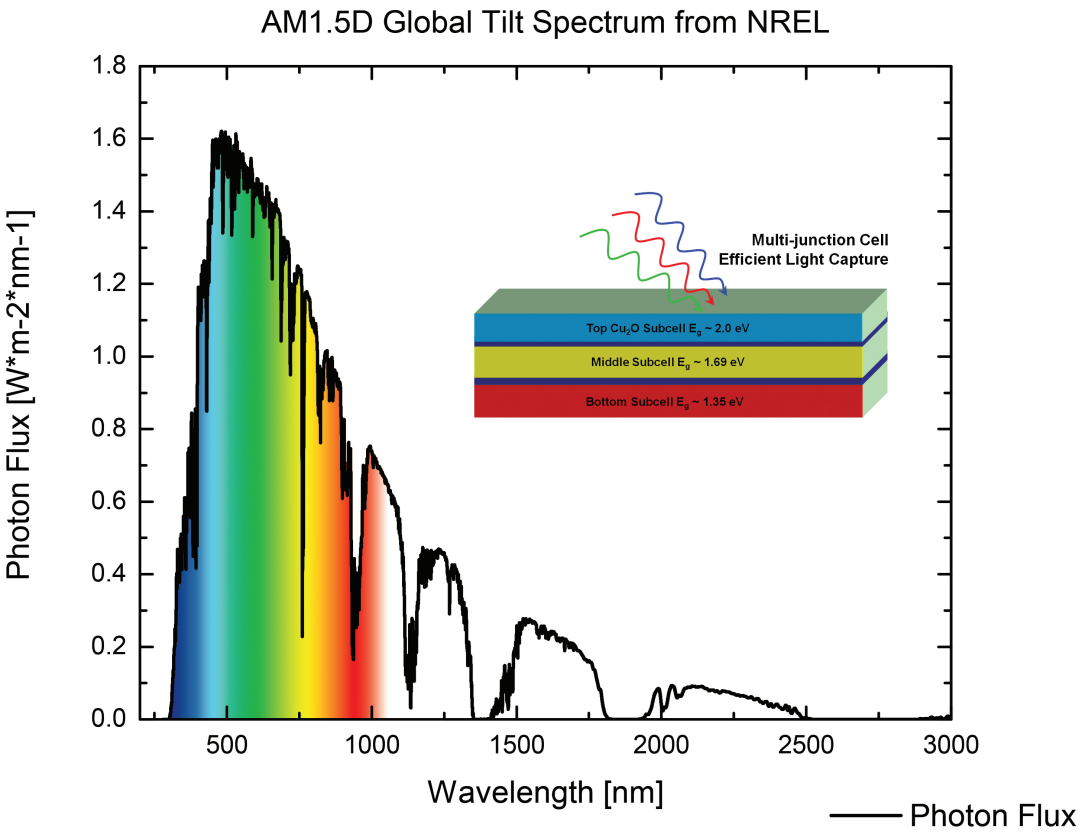

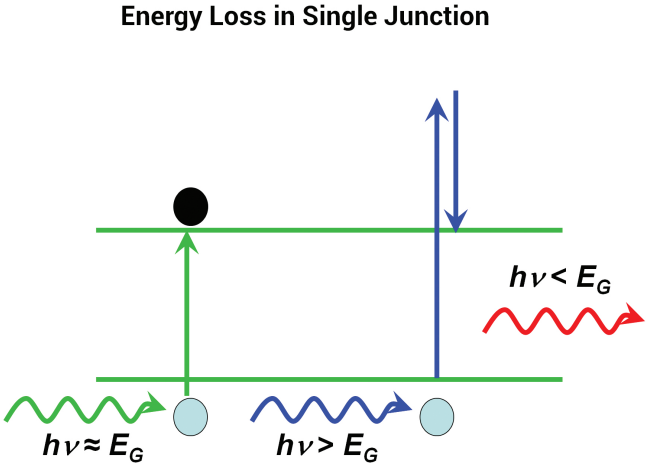

Figure 2.2. The top figure illustrates spectrum splitting in order to increase efficiency of solar cells; the principal behind multijunction cells, the image below shows why spectrum splitting is needed as solar cells are not great broadband absorbers and therefore are either unable to absorb light or lose energy from photons whose bandgap is much greater than the solar absorber through thermalization.

with previous detailed balance model calculations[47]. The reason why the detailed balance efficiency of Cu_2O is not as high other solar materials like silicon, is because of its band gap. The sun is a broadband light source while our solar cell Cu_2O (but true of any other material) is only a really good narrow band collector. Looking at the AM1.5D spectrum in figure 2.1, Cu_2O is unable to absorb any photon less than its bandgap energy which is 2eV or less greater 619nm in wavelength which is equivalent to the integrated area under the curve to the right of 619nm in figure 2.1. While photons greater than the bad gap get absorbed by the material, there is a point at which it is wasteful to absorb those higher energy photons as they must release energry in the form of heat to thermalize down from their incident energy to the operating voltage of the cell; so for example a 3eV photon would waste 1eV of energy in the form of heat if incident upon a copper oxide cell. One method, to more efficiently capture the photons from the sun is to split its broadband light spectrum and use a solar cell that is optimized to each respective section of the spectrum. This design is known as multijunction or tandem photovoltaic cells. Simulation were conducted for a dual-junction cell. The plot shown in figure **??** shows two curves. The solid curve calculates the efficiency of a tandem Cu_2O/PV

This section has been broken down into several subsections. First is a section generally describes the band transport model implemented and its assumptions. The next section outlines our model in specific, and describes the inputs, materials parameters, and changes to the standard model the programs expects in order to properly simulate our cell structure, whose results and discussion are saved for the last section.

2.1.1 Model Background

The modeling conducted in this chapter was done using the software AFORS-HET v 2.2[48] (**a**utomat **for** **s**imulation of **het**erostructures), designed and distributed by the Helmholtz-Zentrum Berlin fur Materialien und Energie. AFORS-HET is a one dimensional numerical simulation program designed to model multilayer homo/heterojunction solar cells as well as providing tools to "characterize" the cells virtually. The

simulation is composed of two part: optical and electrical sub-simulations. The optical sub-simulation calculates the generation rate of carriers (electron-hole pairs) per second per unit volume at a certain depth (x) of the model structure. In addition the standard optical model of Lambert-Beer absorption can be modified to include affects such as reflections, scattering, and etc. The electrical sub-simulation calculates the charged carriers densities, and the electric potential at any given depth (x) of the structure while operating under specific conditions such as open-circuit voltage. In order to conduct an electrical simulation, an optical simulation must be carried out first the create the generation profile of the charged carriers and a recombination rate has to be stated in terms of the unknown independent variables n, p, electric potential and can be designed by the user of the software to include effects such as radiative recombination, Auger recombination, Shockley-Read-Hall recombination, and dangling bond recombination. The program numerically solves the one dimensional differential equations equations with boundary conditions under steady state at discretized points x_i along the depth of the structure. All other unknown quantaties in the equations can be written in terms of the free electron and free hole density, n_i, p_i and the cell potential ϕ_i at each gridpoint x_i.The equations are solved using Newton-Raphson method. This methods solves for the internal cell characteristics such as the generation and recombination profiles, carrier densities and band diagrams. In order to calculate certain properties, the time-dependent differential equations would be typically needed, but using instead can be accomplished using small sinusoidal perturbations to the boundary conditions. Only first order terms are considered and allow the quantities to be described the equations below:

2.1.1.1 Bulk

$$n(x,t) = n(X) + \tilde{n}(x)e^{\iota\omega t} \tag{2.5}$$

$$p(x,t) = p(x) + \tilde{p}(x)e^{\iota\omega t} \tag{2.6}$$

$$\varphi(x,t) = \varphi(x) + \tilde{\varphi}(x)e^{\iota\omega t} \tag{2.7}$$

The solution to the three differential equations that describe the characteristics of the bulk of the material use Poisson's equation and the transport equations for holes and electrons.

$$\frac{\varepsilon_0\varepsilon_r}{q}\frac{\partial^2\varphi\,(x,t)}{\partial x^2} = p\,(x,t) - n\,(x,t) + N_D - N_A + \sum_{defect}\rho_t\,(x,t) \tag{2.8}$$

$$\frac{-1}{q}\frac{\partial j_n\,(x,t)}{\partial x} = G_n\,(x,t) - R_n\,(x,t) - \frac{\partial}{\partial t}n\,(x,t) \tag{2.9}$$

$$\frac{1}{q}\frac{\partial j_p\,(x,t)}{\partial x} = G_p\,(x,t) - R_p\,(x,t) - \frac{\partial}{\partial t}p\,(x,t) \tag{2.10}$$

The variables n, p, and φ are the independent variables solved in the system. The remaining variables such as the layer's absolute and relative dielectric constant, concentration of donors and acceptors N_D , N_A and defect concentration are variables assigned a value by the user prior to the simulation being conducted. The electron/hole currents are determined from the gradient set by the quasi-Fermi energy which is equivalent to the summation of the drift and diffusion currents with their corresponding mobilities.

$$j_n(x,t) = q\mu_n n(x,t)\frac{\partial E_{Fn}(x,t)}{\partial x} = -\frac{\mu_n kT\partial n(x,t)}{q\partial x} + \mu_n n(x,t)\frac{\partial\varphi(x,t)}{\partial x} \tag{2.11}$$

$$j_p(x,t) = q\mu_p p(x,t)\frac{\partial E_{Fp}(x,t)}{\partial x} = -\frac{\mu_p kT\partial p(x,t)}{q\partial x} - \mu_p p(x,t)\frac{\partial\varphi(x,t)}{\partial x} \tag{2.12}$$

2.1.1.2 Generation

There are several methods by which a generation profile can be generated. In order to not digress too far off topic we describe the most common method. A simple model is used where the incoming photon flux is a function of wavelength, a parameter that is set by the user by selecting a particular spectra. Photons with energy $E \geq \frac{hc}{\lambda}$ then are exponentially absorbed by the Lambert-Beer Law.

2.1.1.3 Recombination

In the model to be presented at the end of this chapter, only Radiative and Schokley-Read-Hall recombination are considered. The former is built-in to the recombination profile automatically and thus the user must only concern themselves with SRH recombination. As discussed earlier in section 1.4.3 there are plenty of point defects in copper oxide and they are responsible not only for the materials conductivity but ultimately also responsible for SRH recombination. The program places and arbitrary number of defects, distributed arbitrarily withing the bandgap. The SRH recombination then is required to specify the distribution of the defects in energy space. The emission rate is calculated using the defects electron/hole capture coefficients which then is used in conjunction with the distribution of occupied defect states to calculate the SRH recombination rate due to defect. The result of the derivation for both n and p type carriers is shown in equation 2.13.

$$\tilde{R}^{SRH}_{p/n}(x) = \int dE\{c_{p/n}N_t(E)f_t(E,x)(\tilde{p}/\tilde{n})(x)+c_{p/n}N_t(E)\tilde{f}_t(E,x)+e_{p/n}(E,x)N_t(E)\tilde{f}_t(E,x)\} \tag{2.13}$$

2.1.1.4 Heterojuntion Interface

AFORS-HET uses one of two models for transport of carriers across the interface. The first is a model that uses an interface layer of a certain thickness specified by the user when creating the mesh, in which the material properties change linearly across the junction from the values of the properties of semiconductor A to semiconductor B with

defect that are homogeneously distributed through out this thin layer. The carrier transport then is simply thought of as bulk-like (drift/diffusion driven). The band alignment is treated as simple as possible by using differences in electron affinities in order to establish the quasi-Fermi level, thus establishing the maximum operating voltage of the cell. The current then is simply calculated as the gradient of the quasi-Fermi levels. The second model for transport across the heterojuntion interface is currents driven by thermionic emission which is an appropriate model when the band alignment of your heterojunction includes energetic barriers such as spikes or cliffs where a probability factor for thermionic tunneling is included in the solution. In addition the interface is not considered continuous in this calculation but rather a boundary condition. The built-in module for simulating interface defects was giving unphysical results. We were able to work around this issue by including our own Δ X layer at the interface that had the same characteristics as what is described in the documentation and were able to to continue our calculations, obtaining results that were expected.

2.1.1.5 Contacts and Boundary Conditions

The electric potential is fixed at 0V on one contact. A boundary condition must then be specified at the second contact so that there can be a relation between the external current/voltage and internal quantities. These are the final sets of conditions needed in order to solve the differential equations to calculate n(x), p(x), and φ(x)

$$\varphi(0) = \phi_{front} - \phi_{back} + V_{ext} \tag{2.14}$$

$$\varphi(L) = 0 \tag{2.15}$$

$$j_n(0) = qS_n^{front}(n(0) - n_{eq}(0)) \tag{2.16}$$

$$j_n(L) = -qS_n^{back}(n(L) - n_{eq}(L)) \tag{2.17}$$

$$j_p(0) = -qS_p^{front}(p(0) - p_{eq}(0)) \tag{2.18}$$

$$j_p(L) = qS_p^{back}(p(L) - p_{eq}(L)) \tag{2.19}$$

Where the following variables are inputs into the model; φ : metal work function, S: surface recombination velocity). The density of majority carriers are either (n_{eq} or p_{eq}) which is determined by the energy barrier height of the contact/semiconductor interface. Then the minority carrier density can be derived from the law of mass action;

$$n_{eq} = N_c exp\frac{q\phi - q\chi}{kT} \quad \text{or} \quad p_{eq} = N_V exp\frac{E_g - q\phi + q\chi}{kT}$$

$$n_{eq}p_{eq} = N_c N_V exp\frac{E_g}{2kT} \tag{2.20}$$

2.2 Cu_2O\ZnO Materials Models and Simulation Parameters

Using Afors-Het, a device physics model of a Cu_2O /ZnO heterojunction cell was developed and allowed us to gain a better understating of how the defects and band structure of the heterojunction affect the efficiency of the cell. Most often, if Cu_2O is being used as a solar absorber in a heterojunction it is usually paired to ZnO. This is because the Cu_2O/ZnO heterojunction is the material system to be studied in most detail and still offers the most promise in making higher efficiency heterojunctions. To simplify the simulation ZnO was not included in the numerical calculation as an electrical layer since it gives a negligible contribution to the photocurrent. Instead, the effect of Air/ZnO stack on the optical absorption of the Cu_2O layer was included in the simulations. The main effect of the ZnO is the generation of a built-in voltage (band bending) in the Cu_2O layer and so we employed the Schottky heterojunction interface approximation where the following conditions are set.

1. ZnO is modeled as a metal (that means it is degenerately doped) whose work function is equal to the electron affinity of ZnO.

2. Optical absorption of ZnO is still taken into account via an optical layer on top of our solar cell.

3. Interface defects can be controlled by both inserting a thin Cu_2O defect layer or by varying the surface recombination velocity at the heterojunction interface.

Table 2.1. AFORS-HET model Parameters & Cu_2O Properties

Optical Data Input = Spectroscopic Ellipsometry Data
$Nc/Nv = 2.44x10^{19}/1.1x10^{19}$
$E_{Cu}^{Vac}/E_{Cu}^{DiVac}/E_{O}^{Vac} = .45eV/.25eV/.91eV$
$E_g = 1.95eV$
$\chi = 3.3eV$
$m_e/m_h = .59m_e/.98m_e$
The parameters below were varied in the simulation if and where appropriate.
$\chi, \mu_n, \mu_p, N_a, N_d, N_{trap}$, thickness $= x$

The materials models used in the simulation were developed from both optical and electronic measurements of thin film samples primarily fabricated in our labs using plasma-assisted molecular beam epitaxy of Cu_2O, and ZnO. When characterized these thin film samples had a range of different properties dependent on their deposition conditions. In addition the proper deposition conditions were determined for fabricating thin film samples such that their electrical and optical properties properties were reaching the bulk like limit. Certain measurements were not conducted on our samples, either because they had well established values which were obtained from literature, or because their value was a variable or directly dependent on a variable that was being varied in the simulations. The values that were obtained from literature were electron affinity and the effective mass of holes and electrons. Table 2.1 shows the information that was inputted into the simulation software. The adjusted model as well as our materials models was evaluated in order to determine if the solution produced were both valid and accurate. This evaluation was conducted by importing the simulated structures of several different published Cu_2O/ZnO heterojunction solar cells and and simulating several different characteristics for result. Specifically the model was

used to simulate their IV characteristics under AM1.5D illumination as well as their spectral response. The results of our validity simulations conducted was in close

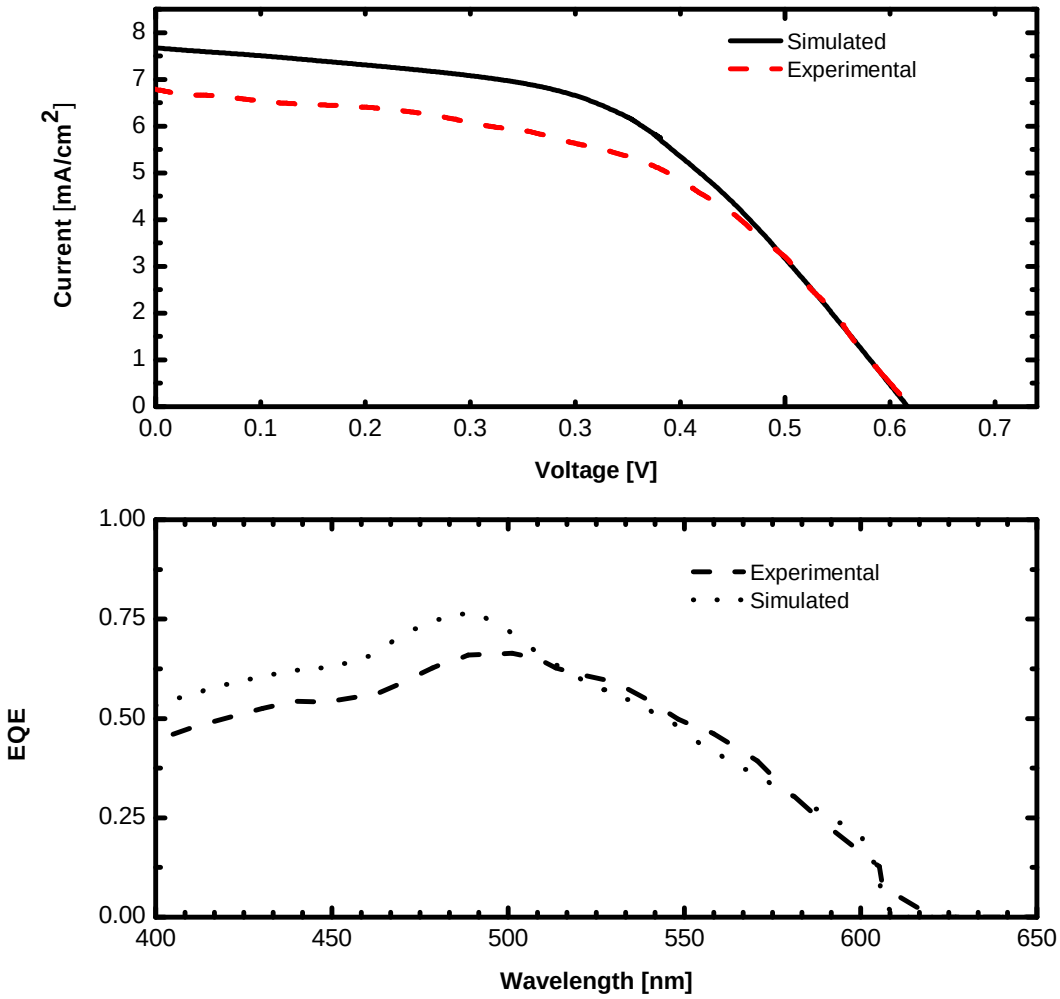

Figure 2.3. IV characteristics and external quantum efficiency plots for simulated Mittiga heterostructure vs their published experimental results. The shape of the curves are nearly identical and are slightly different due to the omission of some optical layers in our simulation.

agreement (well within a small margin of error) to efficiency calculations and produced nearly identical IV and Q.E. curves when compared to the results and curves in the published work we simulated. One such set of validity data is included in figure 2.3, which show our simulated data in comparison to the experimental work and data published by Mittiga[37]. These results seemed to validate our model which made us

comfortable enough to proceed using the model for a series of simulation with a high degree of confidence that those results outputted by the simulation would be would be correct and accurate. Another example of a Cu_2O/ZnO heterostructure is listed in appendix C which includes all input parameters of our model as well as a simulated output in text mode. Content with the accuracy of the validation simulations, our materials models were implemented into a new generic structure often referred to as the "typical" Cu_2O/ZnO heterojunction, because of the number of groups and people who have experimentally fabricated and reported values for a very similar if not exact structure. The crucial choice of our base simulation, which will be the start point or reference point for all the simulations conducted, was thought through very carefully because it is one of only a few points that allows easy comparison between important properties without too much convolution and because of that allows one to essentially rank in order which parameters have the most or least affect on the performance of the cell. These results would point out the critical parameters or properties of a Cu_2O/ZnO heterojunction solar cell and serve as cost benefit guidelines for further optimization and research of these cells. The five properties which have are believed to have the greatest impact on solar cell performance were varied in our Cu_2O/ZnO heterojunction model and simulated I-V and quantum efficiency plots were generated to determine effect on solar cell efficiency. The five parameters varied were thickness, p-type carrier concentration, diffusion length, band offset, and heterojunction interface recombination velocity (a figure of merit for heterojunction interface quality) of the Cu_2O. For most of the results presented, the simulations were conducted four times for differing minority carrier diffusion lengths, significant of poor quality material when the diffusion length is at 100nm diffusion and very high quality material at diffusion lengths reaching near 10μm . It has been long speculated that the Cu_2O/ZnO heterojunction interface, or lack thereof, has been the most detrimental effect to the devices performance. The interface has two primary effects on the cell, both of which have been modeled. The more obvious problems are the interface are defects and traps which facilitate recombination of charged carriers in the cell. Because of our earlier choice to simplify the simulation so that we did not need to include ZnO in any

numerical calculation due to its negligible contribution to photocurrent, we are not able to simply obtain efficiency as function of varying N_{trap}. Instead we simulate the efficiency of the cell vs. surface recombination velocity at the heterojunction interface as seen in figure 2.4 and use relation refeq:ntrap to back calculate the number of traps present at the interface.

$$N_{trap} = \frac{S_{interface}}{V_{th}\sigma_{trap}} \tag{2.21}$$

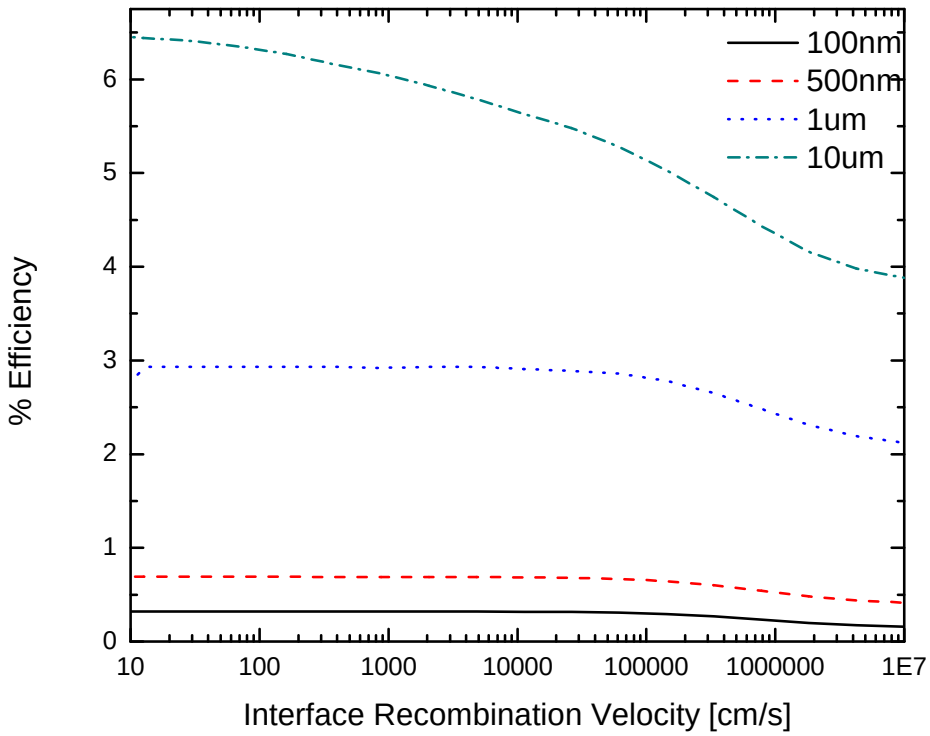

Figure 2.4. The efficiency of a ZnO/Cu_2O heterostructure vs interface recombination velocity which can be converted to trap density at the heterostucture interface. This plot shows results for four different minority carrier diffusions lengths.

At 100nm minority carrier diffusion length the material is essentially bulk recombination limited while at 10μm it is interface recombination limited. Most experimental cells are closer to the bulk recombination limit where minority carrier diffusion lengths are in the 100-500nm range[49]. The other important feature the heterojunction interface creates is band bending. To simulate band bending, the electron affinity of Cu_2O was

artificially changed and brought closer to the value of the ZnO electron affinity. Figure 2.5 shows that the efficiency increases significantly as the heterojunction bands go from being almost a type II to type I heterojunction. Because of Cu_2O low electron affinity (3.3 eV) compared to ZnO (wide range) the maximum voltage a Cu_2O solar cell cannot be realized in this heterojunction [14]. Unfortunately, there is very little that can be done for a particular heterojunction in terms of changing the band bending at the interface for a particular heterojunction pair. The exception is when one has complete control over the texture of the thin films. Certain crystal orientations of ZnO have different values of electron affinity due to the polar nature of its crystal lattice [50]. Before conducting these simulations, we believed that these two properties would have the greatest effect on the efficiency of the solar cell. However another

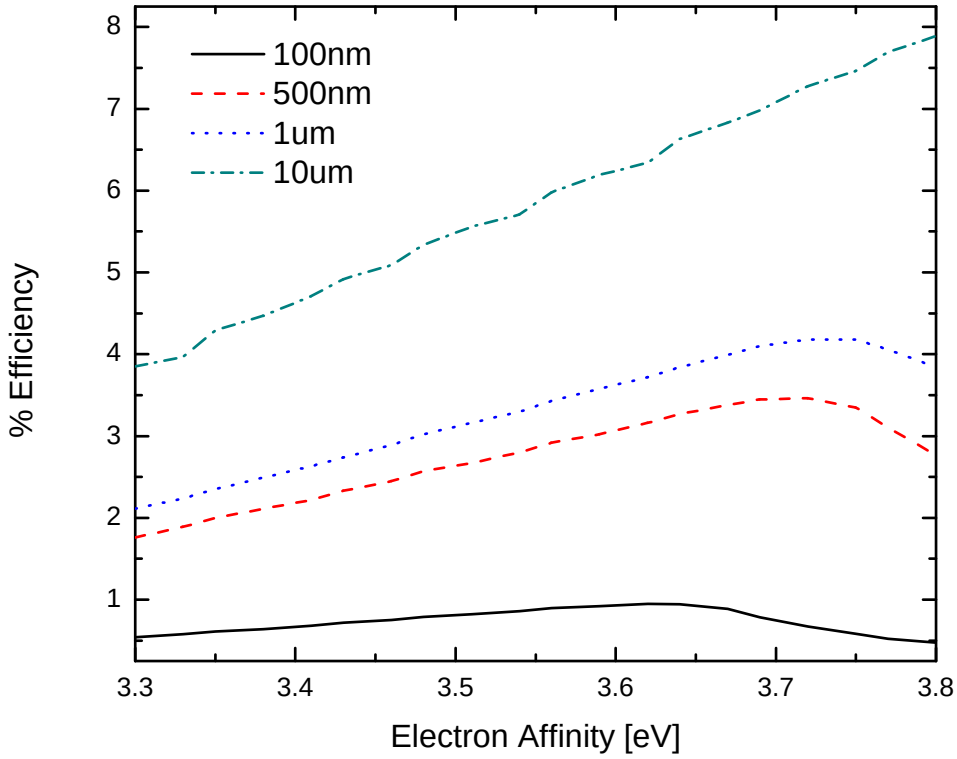

Figure 2.5. The efficiency of a ZnO/Cu_2O heterostructure vs the electron affinity of the Cu_2O layer. This plot demonstrates how Cu_2O low electron affinity is unfavorable for this heterostructures band bending. This plot also shows results for four different minority carrier diffusions lengths.

property of the solar cell clearly dominated its performance. The doping, and more importantly type of dopant, plays an integral role. The simulated model only took into account Cu_2Os intrinsic doping mechanism where equilibrium point defects determine the carrier concentration. These point defects are outlined in Table 2.1 and have energies deep in the forbidden band gap of Cu_2O. Copper vacancies are responsible for Cu_2Os conductivity and were used in the materials defect and doping model as well as including the self-compensating mechanism that produces oxygen vacancies. Both of these defects play a critical role in the conductivity and lifetime of a Cu_2O cell. Copper and oxygen vacancies were varied along with the carrier concentration N_a. Figure 2.6 shows when Cu_2Os carrier concentration is low, it behaved like an intrinsic semiconductor and as the doping increased so did the cells conductivity and open-circuit voltage thus increasing the efficiency. An unexpected feature was discovered in the simulation. When the doping reached $1x10^{14}$ carriers/cm^3 any increase seen in the cells current was at the expense of the cell's open circuit voltage. This phenomenon can be explained by an indirect connection between bulk minority carrier diffusion length and the p-type intrinsic carrier concentration. As previously mentioned, it has been established that Cu vacancies are the main mechanism which leads to Cu_2O's p-type conductivity. This equilibrium point defect mediates Cu_2O's self-compensation mechanism where the more acceptor impurities are inserted (Cu_{vac}), the more the energy of formation of donors are lowered and more donor defects are formed thus increasing the number of traps in the midgap of Cu_2O and decreasing the cell's mobility, and minority carrier lifetime. The cell's efficiency as a function of diffusion length which is related to the cell minority carrier lifetime is shown in figure 2.6 as well on the top axis. From this plot it can be deduced that the two parameters are intimately connected to one another in the particular case where no extrinsic dopant was used. Using the diffusion length corresponding to a particular intrinsic doping concentration, one can go back to any of the previous plots to get an idea of the efficiency of the cell with those given parameters. The plot demonstrates how the efficiency is most greatly affected by diffusion length and how the cell efficiency increases dramatically if one could dope the cell without creating additional defects.

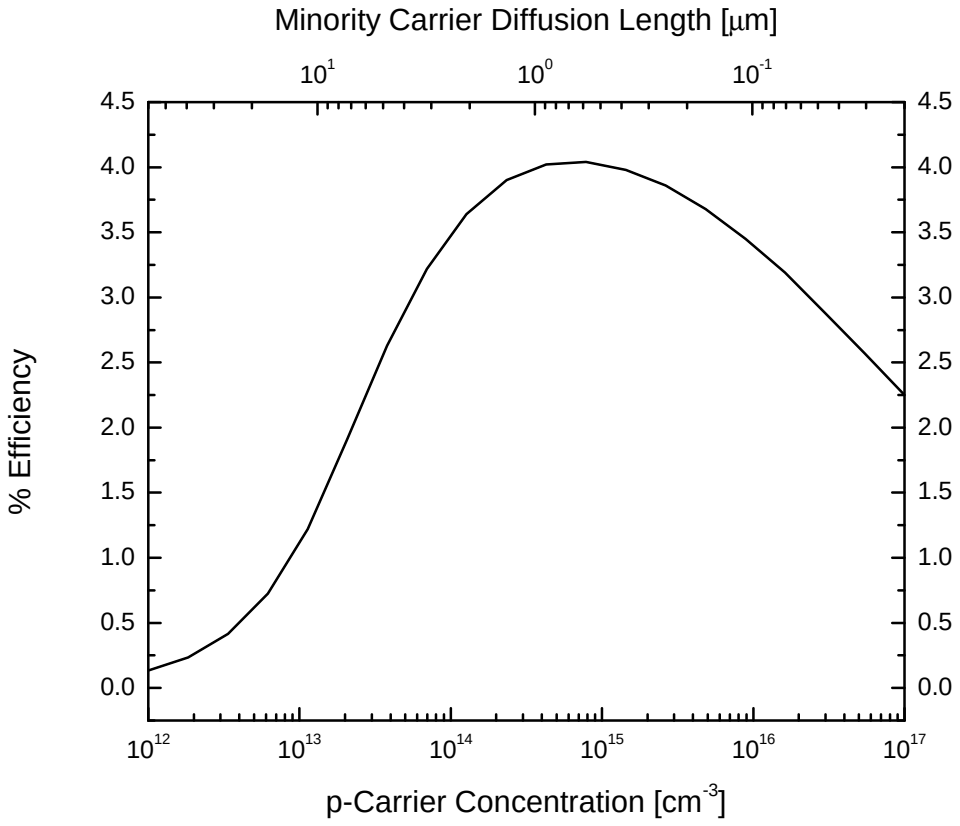

Figure 2.6. Efficiency of the Cu_2O/ZnO cell as a function of intrinsic carrier concentration as well as diffusion length. This is because intrinsic dopants act as deep level traps which destroy minority carrier diffusion lengths in the bulk.

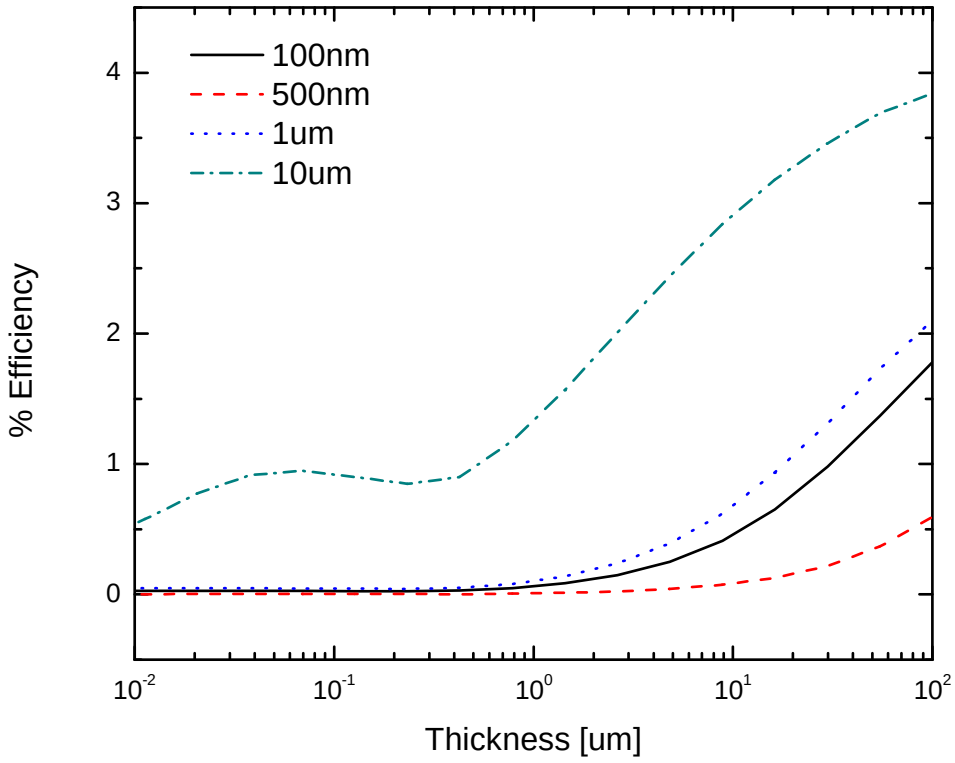

Figure 2.7. The efficiency of a ZnO/Cu2O cell vs thickness of the cell. This plot shows results for four different minority carrier diffusions lengths.

Unfortunately as it stands now no dopant has been found which introduces a shallow acceptor level and does not introduce a new recombination channel for the minority carries. For that reason, having a large N_a is undesirable which makes the Cu_2O layer very resistive. For that reason, the thickness of the cell played a more important role than expected. When the Cu_2O layer was too thin the cell simply could not absorb enough light and created negligible current. As the cell thickness increased so did the efficiency, but at some point the cell became too thick as demonstrated by the inflection point at roughly $1x10^5$cm in figure 4d. This feature is attributed to a decrease in the cells fill factor as the minority carrier collected by the junction must traverse the thickness of a fairly resistive semiconductor to be extracted from the cell. Therefore the final three parameters discussed above have an indirection relation with one another that greatly affect the efficiency of the cell.

2.3 Conclusion

By conducting these simulations of a Cu_2O/ZnO heterojunction, we have identified the critical properties and parameters of the heterojunction that have been keeping efficiencies far from their theoretical values. More importantly the results of these simulations have allowed us to rank the importance of tweaking these parameters/properties in order to obtain higher efficiencies. The simulations revealed the most important property to focus on is the urgency of finding an extrinsic dopant, as current intrinsic doping limits both diffusion length of our material due to them acting as deep level traps as well as lowering our open circuit voltage as it pins the firm level away from the valence band edge. We also discovered the importance of having a defect free interface as the number of traps at the heterojunction interface also greatly affects the efficiency of the cell. This issue may be overcome by using growth methods such as MBE or clever oxidation techniques that allow epitaxial growth of our heterojunction layers thus dramatically lowering the concentration of interfacial defects at the heterojunction interface. Attempting to solve these problems, Cu_2O/ZnO heterojunction solar cells will be able to achieve efficiencies well above 10%.

Chapter 3

Growth of High Quality Cu_2O Thin Films via Plasma-Assisted Molecular Beam Epitaxy

Molecular Beam Epitaxy (MBE) is one of the more difficult fabrication techniques to use and master. However, it allows precise control over almost any parameter one can think of. In addition, MBE systems often include a vast variety of *in-situ* characterization tools, which provide real time information on the evolution of growth and state of the sample. It is not necessary for one to wait for a deposition process to be complete before being able to probe the material in order to determine the phase material grown; whether or not it is strained, possibly because of impurities, or if the material is crystalline or amorphous. This chapter begins with an introductory section on vacuum science, and thin film deposition; specifically the fabrication of thin films using molecular beam epitaxy. The chapter continues with a description of the experimental setup used to fabricate Cu_2O/ZnO heterojunctions and investigates the epitaxial growth of high quality Cu_2O and ZnO thin films on both bulk MgO substrates as well as biaxially textured ion-beam assisted MgO templated substrates using plasma enhanced molecular beam epitaxy. The structural, optical and electrical characterization conducted on these thin films will be discussed. Finally, we present a process for creating a Cu_2O/ZnO heterojunction device with 0% shadowing loss using an interdigitated metallization contacts scheme, and present device results.

3.1 Vacuum Science Basics[1, 2, 3]

In its most basic definition, a vacuum is space that is empty of matter and that is extremely important in the discussion of thin films. Because it is impossible to achieve a perfect vacuum , there will always be some "matter" in space; and typically it is matter that we do not want there when we are talking about thin film deposition systems. The quality of a vacuum is often divided into several categories and while the there is no official standard for the ranges of quality, they are most often the same, even across scientific disciplines. The four main ranges are rough vacuum (RV) from 1 atm to approx 1torr, medium vacuum (MV) from 1 torr to 1mtorr, high vacuum (HV) from 1mtorr to .1μtorr, and finally ultra high vacuum (UHV) from μtorr to essentially perfect vacuum. While these pressures are general guidelines, most people prefer to delineate the pressure regime they are in by the nature of gas flow. There are two main flow regimes that are encountered in vacuum technology: viscous or continuous flow, and molecular flow. Some may consider Knudsen flow, which is the transition between the two flow regimes; its own type of flow, but that label is unnecessary. Viscous flow is the type of flow that is determined by the interaction of molecules. That is because the mean free path λ of atoms or molecules is much less than the chamber or pipe diameter d (λ¡¡d). Molecular flow begins to prevail when the mean free path of atoms is on the order of or greater than the size of the chamber or pipe. The mean free path λ describes the distance an atom or molecule can move freely in space without interference of any other molecule or atom. In molecular flow that distance is often on the order of meters, and this regime is typically what allows high quality defect free films to be fabricated. In order to achieve a vacuum in space, a pump must be used to evacuate the air present in the chamber. There are a plethora of pump to pick from, and each type of pump is specifically designed and fitted for a particular application. A combination of pumps must be used in order to typically reach and maintain HV and UHV systems. The final stage pump on these type of systems are always oil free and are typically backed by other pumps in case of a catastrophic failure of the main pump. There are so many different pumps that taking the time to discuss all of them

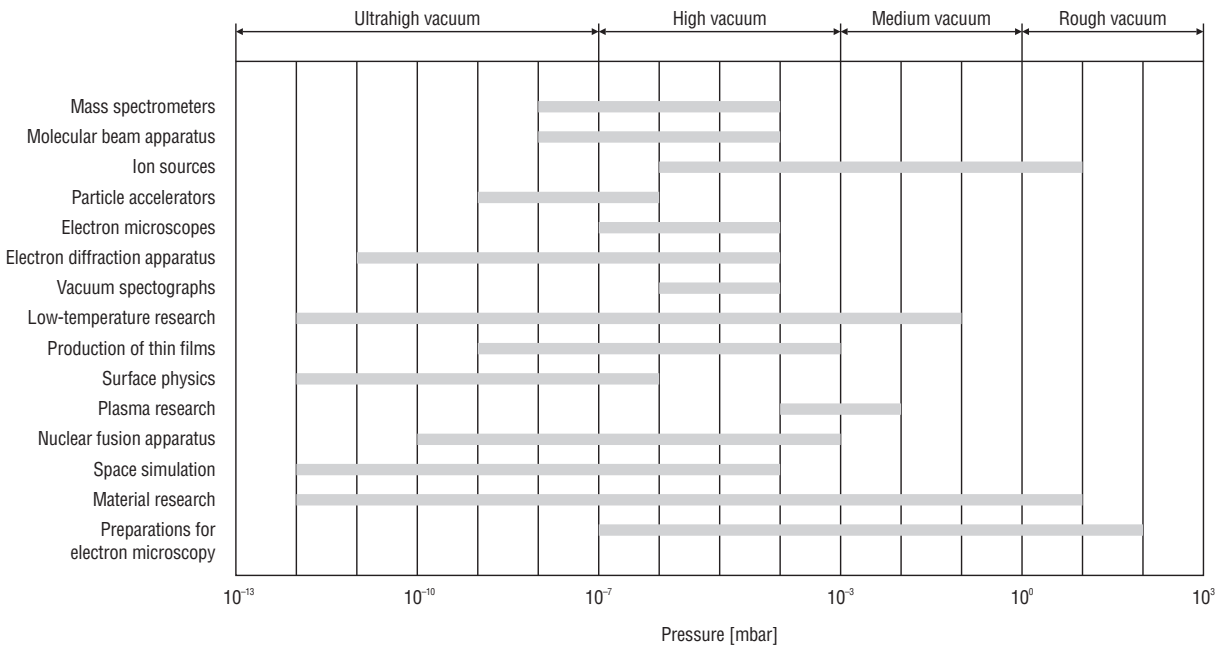

Figure 3.1. Pressure ranges of physical and chemical analytic methods.

would require a written thesis of its own. But this will highlight the types of pumps connected to our MBE system, which is a fairly typical setup for growth of oxides using MBE. Like most other vacuum systems, our MBE is roughed from atmosphere to high vacuum using a series of mechanical pumps Rotary pumps, and turbo molecular pumps. The final stage of pumping is conducted by cryogenic pump which uses ultra pure helium and compresses the gas on a cold head bringing the temperature down to nearly 10^o Kelvin. Not only does a cryopump operate fundamentally differently then most other pumps, but it also is one of few pumps that does not exhaust the gas that captures. Furthermore, but it rather freezes it on the array of carbon discs till a regeneration cycle is able to be conducted. Cryo pumps are effectively able to remove all gases from the system, and if it operates properly, the ultimate pressure of nitrogen in the chamber at 20^o Kelvin should be below $5x10^{-11}$torr. In figure 3.1 you can see the typical pressures that different systems operate at.

3.2 Molecular Beam Epitaxy[4, 5, 6, 7, 8]

You may ask why is a vacuum so important? Semiconductor processing at all steps requires a super clean environment. that includes anything from hair, to tiny dust particles. As consumers demand for more efficient and smaller devices increase, new techniques which miniaturize electronic components need to be deployed. The miniaturization of technology is done either via lithography or through growth of patterned thin film structures. It is then implied that any defects or unwanted molecules that are on the size scale of the wanted pattern will result in high yield loss. MBE is a technique that is both very similar to standard evaporation, and yet it couldn't be more different or complex. That is because MBE is used as a controlled growth method, capable of deposition at atomic resolution, as well as the continuous growth of a single crystal, also known as epitaxy. The films are formed on single-crystal substrates by slowly evaporating the elemental or molecular constituents of the film from evaporation source known as a effusion or Knudsen cell, onto substrates that are at a particular condition, such that the proper reaction and phase is present at the surface of the substrate. The spot size of these cells are on the order of a couple inches, though commercial deployments have been successful at making larger one, in the very recent past. The growths are typically conducted at a rate of 3000Åper hour, thus the importance of ultra high vacuum can not be emphasized enough. Figure 3.2 shows a standard schematic diagram of an MBE chamber. It also shows the most commonly used *in-situ* characterization system including:

- A beam flux monitor which detects the rate at which atoms emerging from an effusion cell impinge onto the substrate.
- A mass spectrometer/residual gas analyzer which can detect with high sensitivity the partial pressure of any give molecule or atom. An electron gun, also known as a RHEED gun, accelerates an electron beam towards the sample where it diffracts off the top couple nm of material revealing dynamic information about the crystal structure and film thickness.

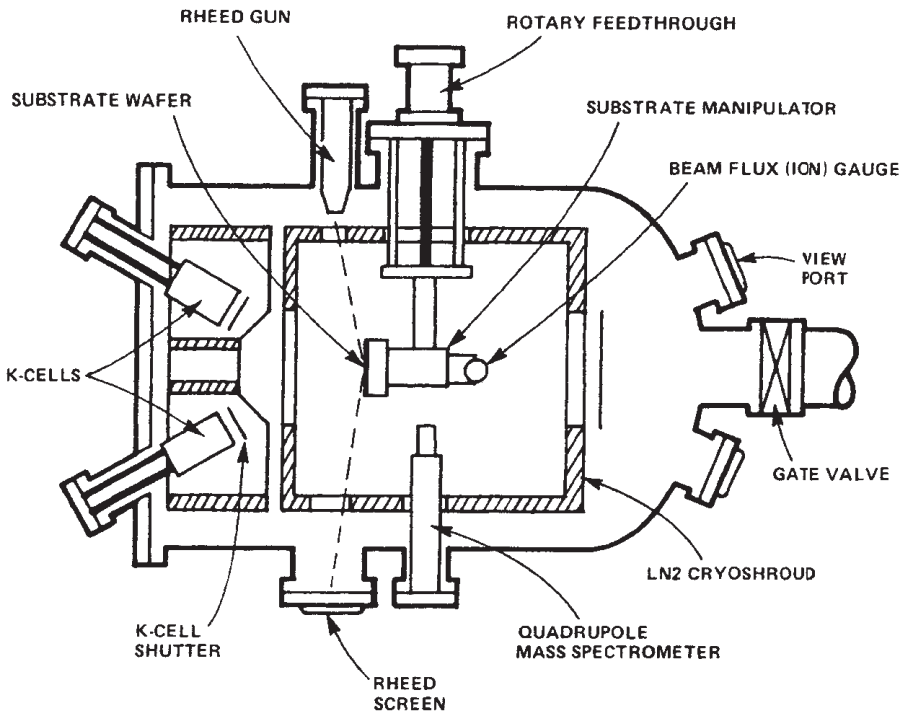

Figure 3.2. Schematic cross-section of a typical MBE Chamber.

3.3 Reflective High Energy Electron Diffraction

Of the three characterization techniques mentioned above, RHEED is the most important technique used during thin-film growth in a MBE system. In RHEED, a high-energy beam of electrons hit the sample at grazing incidence, which reflects off the top couple nanometers of your sample. The reflected beam is scattered, as a result of interacting with atoms on the surface of the sample, and impinges on a phosphorescent screen placed on the other side of the chamber opposite the gun, which displays a diffraction pattern which can be observed. Of course, for diffraction to occur, the electrons that interact with the top layers of material must obey Bragg's law.

$$\lambda = 2dsin(\theta) \tag{3.1}$$

This law relates the wavelength of the electron beam λ, periodicity, d, of the lattice, and the diffraction angle, θ of the beam with respect to the sample surface, in order to construct a diffraction sphere known as a Ewald sphere. The location where the reciprocal lattice rods (probing 2-D planes in k-space produces rods) and the Ewald sphere intersect are where the Bragg conditions are satisfied, and thusly create a diffraction pattern. RHEED intensity oscillations can be recorded during growth in order to resolve atomic resolution of layered growth. During monolayer-by-monolayer growth in an MBE chamber, the surface of the sample changes from smooth to rough (at partial coverage), and back to smooth again in the completion of one monolayer growth cycle. During the periods of the cycle when the sample surface is rough, most of the specular beam incident on the sample is scattered and produces a low intensity spot. When the sample returns to a period where its surface is smooth, the diffracted intensity is at a maximum. The result is that for monolayer-by-monolayer growth, the diffracted RHEED intensity varies sinusoidally with time, with the period of oscillation corresponding to the period of monolayer growth. Counting RHEED oscillations during growth allows one to accurately determine flux rates as well as thicknesses of their layers.

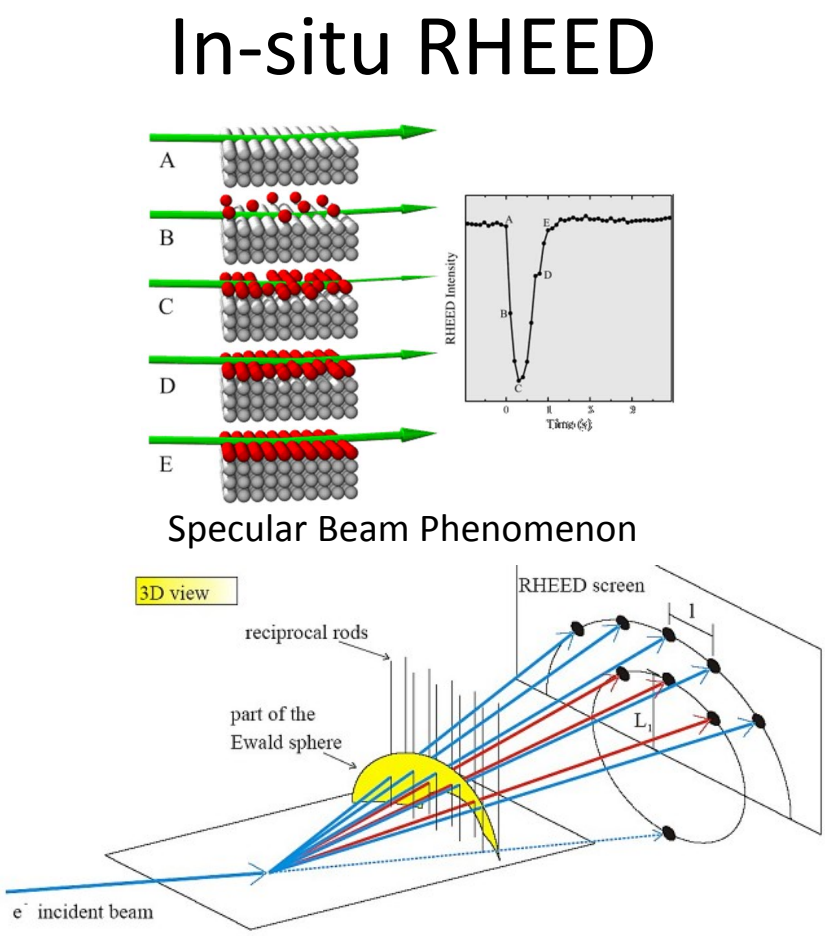

Figure 3.3. Illustration of intensity vs. time in layer by layer growth also known as the specular beam phenomena that produces RHEED oscillations. Below is a depiction of what a RHEED image when the electron beam fulfills the diffraction condition known as Braggs Law.

3.4 Cu_2O Deposition via Plasma Enhanced MBE and Characterization.

Plasma assisted molecular beam epitaxy (MBE) is a promising method for the fabrication of Cu_2O thin films, as it provides the greatest control over critical growth conditions such as temperature, flux, base pressure, and interface sharpness. We used two types of substrates for film growth: 1) cubic magnesium oxide (MgO (001), a=.422nm) and biaxially-texture thin films of $MgO/SiO_2/Si$ grown by ion beam-assisted deposition (IBAD) [51]. A relatively small lattice mismatch of 1.1% between Cu_2O (a=4.27Å) and MgO facilitates epitaxial growth. A copper effusion cell (beam equivalent pressure of $5x10^{-7}$torr) in the presence of a RF oxygen plasma (P=300W) at 10^{-6} torr was used. The MgO substrate was heated to a temperature of T=650^{o}C. All samples were annealed for one hour at T=650^{o}C with varying partial pressures of oxygen from P_{O2}=10^{-4}-10^{-6} torr. The pressure P_{O2}=10^{-6} torr provided the sharpest RHEED. IBAD is a process in which a bi-axially textured thin film of MgO is grown on any atomically smooth surface. We use silicon substrates that have been thermally oxidized to give us a 1μm amorphous SiO_2 layer. Using electron-beam evaporation, thin films of MgO were deposited at room temperature on our SiO_2 substrates at a rate of 0.2nm/sec with simultaneous ion bombardment of a 750 eV Ar^+ ion from an ion gun till the film thickness approximately reaches 10nm. A second e-beam evaporation step is conducted at an elevated substrate temperature without the ion beam to produce a higher quality surface. The surfaces and the evolution of the bi-axially textured film is carefully monitored using RHEED. The second step adds approximately another 10 nm of MgO, making in total 20nm of MgO used in this process to prepare our template substrate. ZnO thin films were grown (growth rate of .2nm/sec) on MgO (001) substrate and on Cu_2O (001)/ MgO (001) by MBE using a zinc effusion cell and an RF oxygen plasma. Prior to the ZnO growth the substrates were thermally cleaned at T=450^{o}C in the presence of the oxygen plasma for 15 minutes. ZnO was then grown at a substrate temperature T=of 350^{o}C in the presence of a RF oxygen plasma (P=200W) at 10^{-4} torr with a beam equivalent

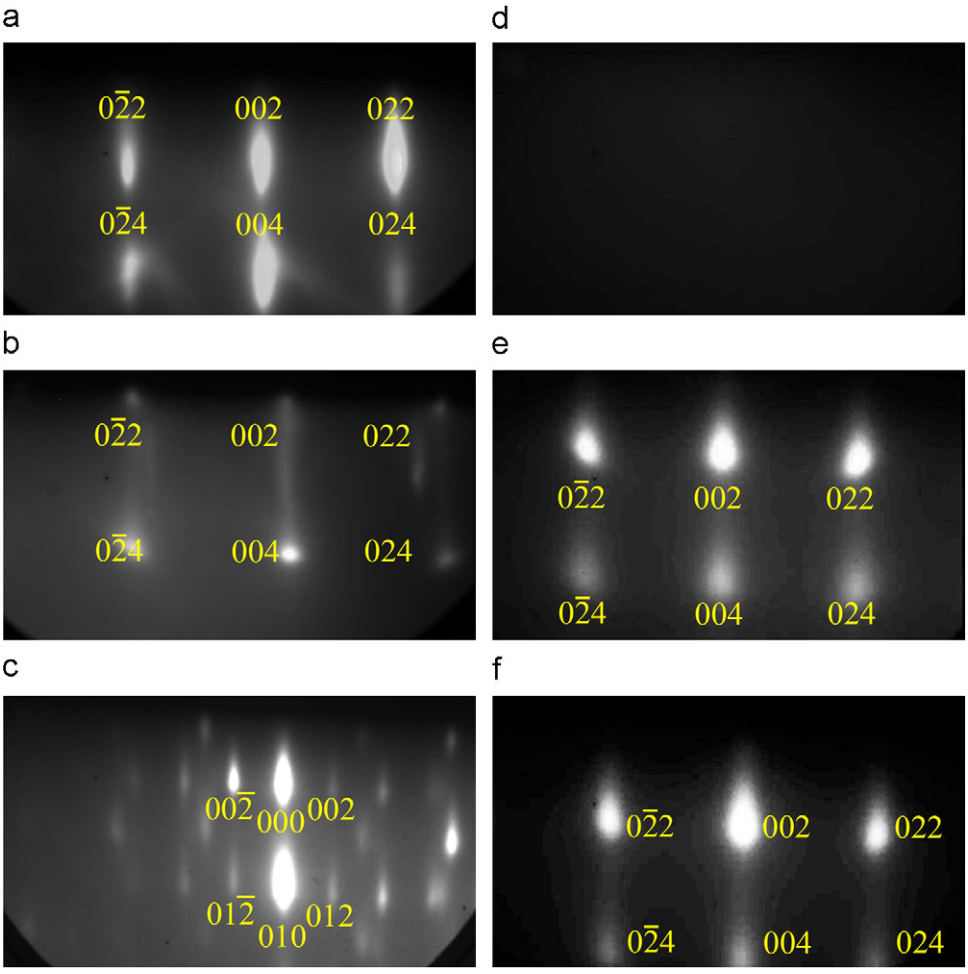

Figure 3.4. On the right hand column are in situ RHEED images from a continuous Cu_2O(001) on MgO(001) where the film thickness is equal to 0nm (a), 30nm (b), and 65nm (c). On the left hand column are in situ RHEED images of a clean SiO2 surface (d), followed by 15nm deposition of IBAD MgO(001) (e), followed by 60nm of Cu_2O (f).

pressure of 1x10^{-6}torr. Slow growths at the beginning stages were critical to obtain m-plane (10$\bar{1}$0) orientation of ZnO as opposed to the typical c-plane (0001) growth of ZnO. In-situ characterizations of our films were done with RHEED. Further analysis was done via x-ray diffraction.

Both the MgO substrate and Cu_2O have a cubic crystal structure and closely matched lattice parameters. Cube on cube epitaxy of Cu_2O (001) was observed to grow on MgO (001). In-situ RHEED was used to confirm the epitaxial growth, which can be seen in figure 3.4. RHEED oscillations (figure 3.5) were observed, indicating that the thin film was growing in a layer-by-layer growth regime, typically seen if growth of the film can be well controlled and grown slowly (approximately 2 Å/sec). The streaky nature of the RHEED images indicated that the Cu_2O films grown were very smooth. X-ray diffraction was conducted on the thin films and confirmed the results seen in the RHEED images. XRD rocking curve analysis also showed epitaxial growth of Cu_2O on MgO with the two peaks at ω=21.58^o and at ω=21.61^o respectively.

IBAD growth of bi-axially textured MgO (001) on SiO_2 (amorphous) was conducted and confirmed via RHEED (figure 3.4). IBAD is a three phase process where a 750 eV Ar^+ ion beam is directed at an amorphous substrate at a 45^o angle during the deposition of MgO using e-beam evaporation. During the first phase an amorphous MgO film is deposited (0-4nm). During the second phase of growth, MgO crystals nucleate via solid phase crystallization with out-of-plane texturing. In the third stage of growth, in-plane texturing is evolved due to the amorphization of grains with misaligned in-plane texturing from the Ar^+ ions. The Ar^+ ions channel in the (011) direction and amorphize the grains not in the (001) direction. When enough material has been deposited, an energetically low surface of (001) is formed and is not damaged due to the channeling of the ions. This Ar^+ ion beam is then turned off and epi MgO is deposited at an elevated substrate temperature to create a near perfect and defect free substrate template. It is then possible to deposit Cu_2O exactly the same way as one would on bulk MgO substrates described above with results and properties of Cu_2O being the same. The advantages of this method are, that it allows a fraction of the substrate material to be used, allows the process of creating very cheap substrates

in comparison to bulk MgO substrates, and allows the growth of any Cu_2O device on top of an already existing device for use in tandem solar cells. In addition, because the template is thin, the resulting film that is grown on top will be less strained and consequently will be of higher quality.

Epitaxial growth of Cu_2O is quite difficult to maintain at very high deposition rates (greater than 120nm/hr of Cu_2O)or thicknesses greater than 1.5 μm. RHEED images in figure 3.6 shows the break down of epitaxy over a 1.5 hour period of time.

In addition to the structural properties of our film being characterized, we took a look at the electronic and optical properties. Energy dispersive x-ray spectroscopy further confirmed the composition of the film and did not indicate impurities in the film. Hall mobility measurements showed mobilities in the range of 50-100 $cm^2/V \cdot sec$ and carrier concentrations typically in the range of 10^{16} cm^{-3}, which is dependent on substrate temperature and oxygen plasma partial pressure. A very smooth film and the ability of in-situ passivation of our interface will hopefully provide the quality interface needed to achieve much higher cell efficiencies. Optical ellipsometry was conducted on the films to determine index of refraction and absorption (figure 3.7). The data measured was subsequently used on other samples to verify film thicknesses and quality post growth. We were also able to extrapolate the band gap of the Cu_2O film grown (figure 3.7) which agrees with previously reported studies. As mentioned previously, heterostructures of Cu_2O are the most promising ways to create photovoltaic devices due to the difficulty in creating homojunctions of Cu_2O that display photovoltaic properties. MgO substrates were also used for the growth of ZnO. Because of the different crystal structures and lattice constants we hoped to develop a technique that would allow textured growth of our films. Oxygen plasma assisted MBE allowed us to gain the control on the growth of the ZnO thin film and allowed us to obtain higher quality material. Upon nucleation of the film, the RHEED pattern transitioned from a streaky to a spotty pattern, indicating a predominate single orientation of growth. The crystalline orientations as determined both by analysis of the RHEED pattern (figure 3.8) and XRD showed a preferential orientation of ZnO in the $(10\bar{1}0)$ with a very weak peak corresponding to the commonly observed (0002) ZnO peak.

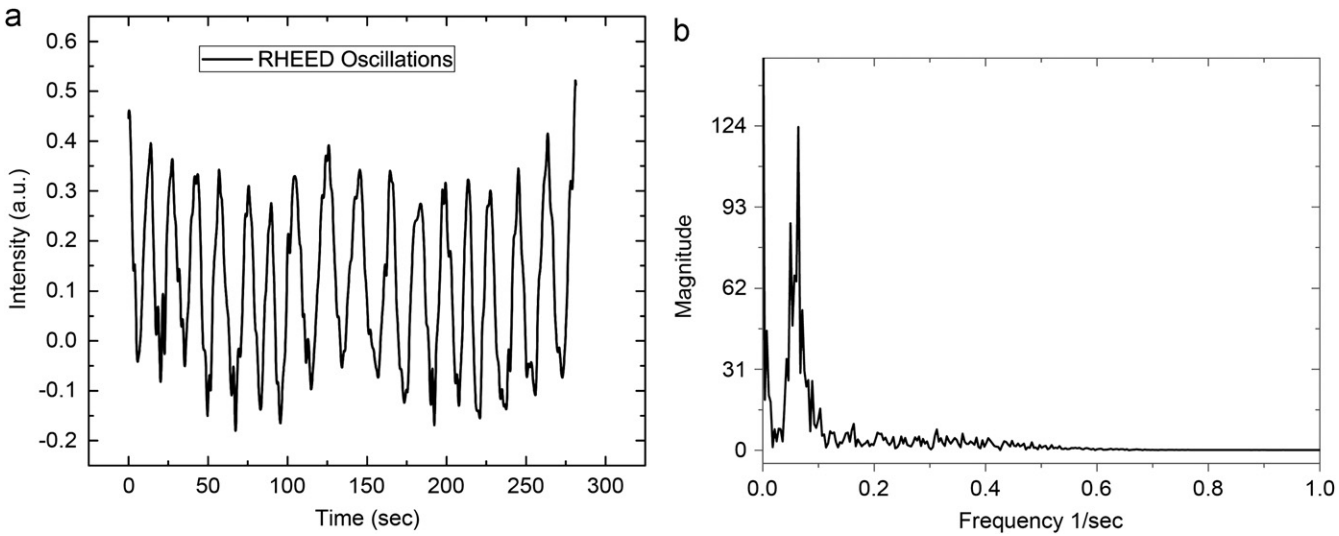

Figure 3.5. (a) RHEED oscillations demonstrating layer by layer epitaxial growth of Cu_2O on MgO. (b) Fourier transform of RHEED oscillations to determine growth rate.

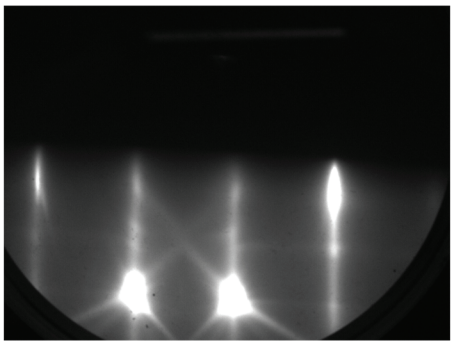

Start with clean MgO Substrate

Copper Oxide Deposition on MgO 001

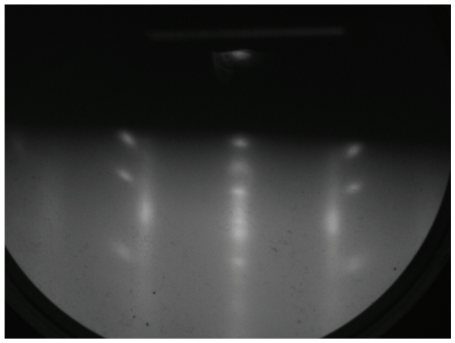

After 1 hour of
deposition at rate 1.5 times usual

Epitaxay breaking down
evident by ring pattern

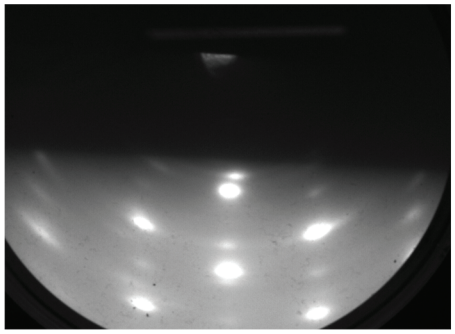

Figure 3.6.

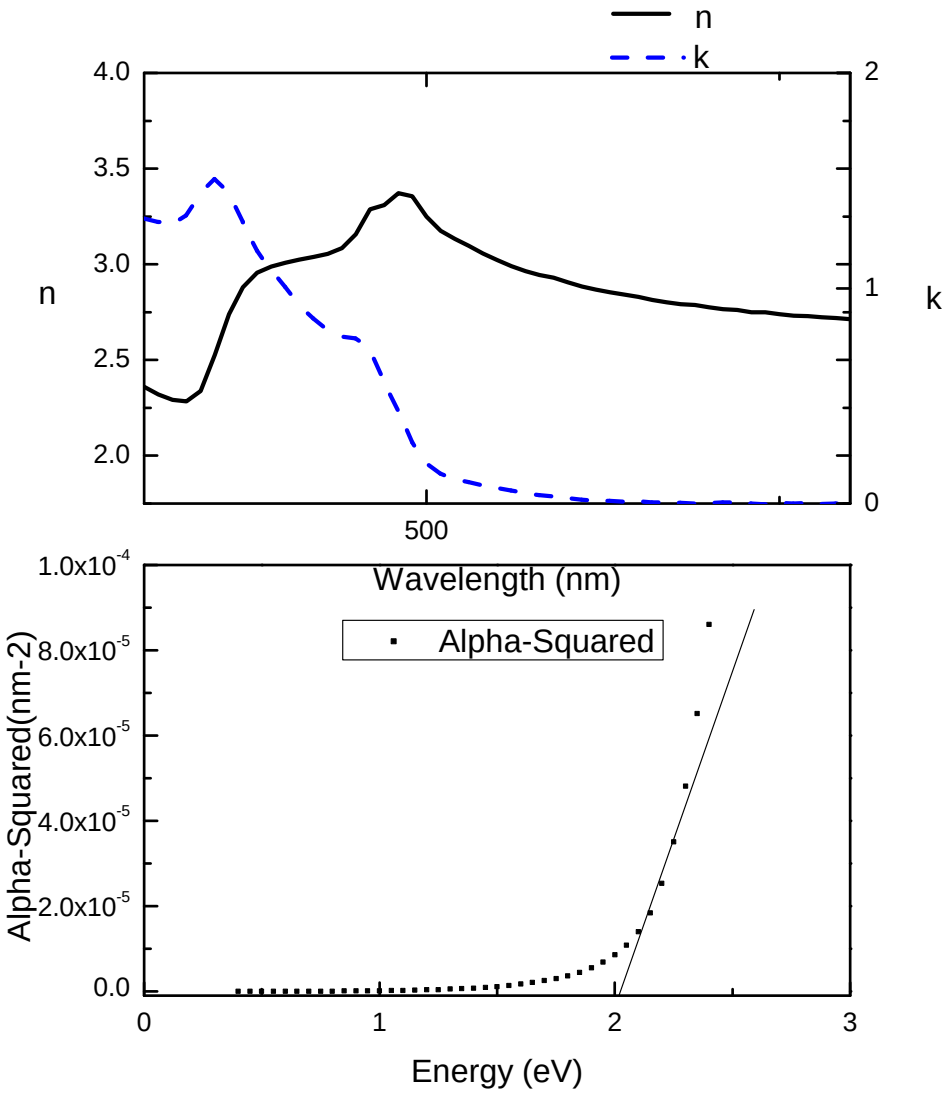

Figure 3.7. Spectroscopic ellipsometry data for real and imaginary index of refraction for Cu_2O thin film. Inset shows alpha square vs. energy which allows extrapolation of band gap of Cu_2O to 2eV.

The dominate peak $(10\bar{1}0)$ is known as the m-plane of ZnO. We believe there is some degree of polycrystallinity near the growth interface that quickly changes and develops into m-plane texturing throughout the entire film. Below are RHEED images of this growth. Similar results were obtained when growing ZnO on Cu_2O thin films that were deposited on MgO.

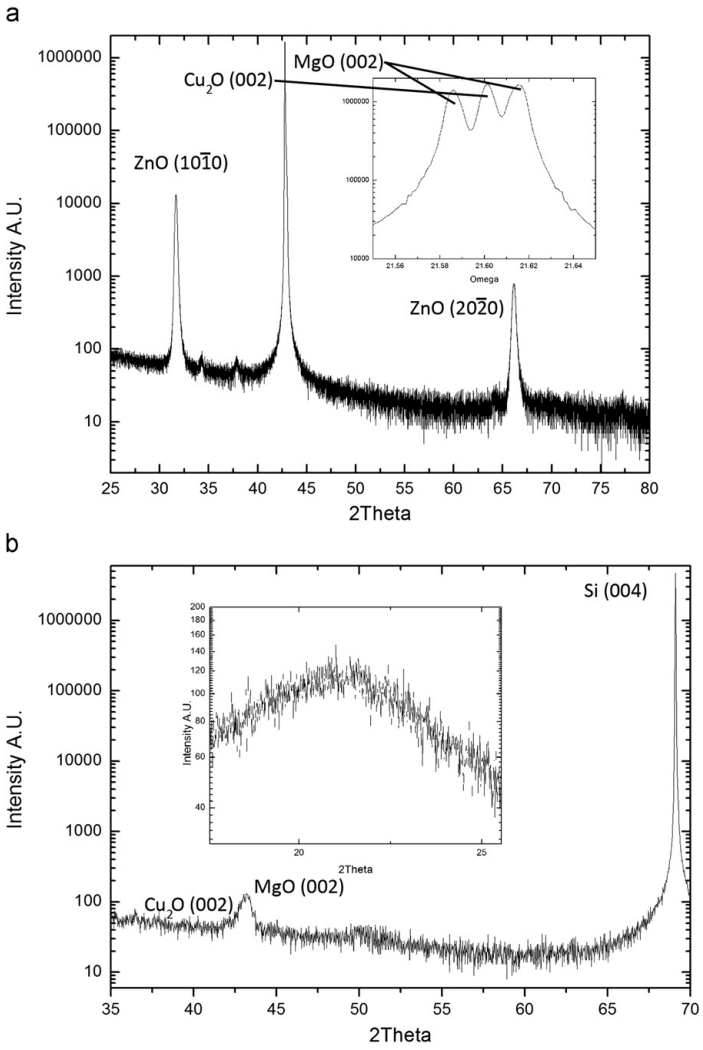

Figure 3.8. In situ RHEED images of (a) $Cu_2O(001)$ on MgO(001) followed by the 30nm deposition of epitaxial m-plane ZnO (b).

3.5 Conclusion of PA-MBE Growth of Cu_2O

We have achieved epitaxial growth of Cu_2O and ZnO on both single crystal MgO and IBAD MgO substrates. MBE growth of the Cu_2O /ZnO heterojunction should allow us to obtain higher V_{oc} and efficiencies due to the high degree of control we have over the crystal orientations of the thin films and the quality of the interface. We have successfully demonstrated MBE growth of epitaxial Cu_2O on (001) bulk MgO and IBAD bi-axially textured MgO. Structural, optical and electrical qualities of the film were characterized using RHEED, x-ray diffraction, EDS, spectroscopic ellipsometry and Hall mobility measurements. These measurements confirmed the high electrical quality of our films and that our Cu_2O had a band gap in accord with the literature. We have successfully demonstrated MBE growth of epitaxial ZnO on $(10\bar{1}0)$ bulk MgO (001) and on top of our Cu_2O films.

3.6 Cu_2O/ZnO heterojunction Design, Metallization, and Results

In this section, we will discuss the design challenges of make a Cu_2O/ZnO heterojunction device, followed by introducing several different device designs, and finally the performance of these devices. Earlier, the idea of using templated substrates was introduced. We demonstrated that MgO films as thin as 5nm could be deposited on any smooth substrate (amorphous, glass, etc) using IBAD to create bi-axially texture thin-film template which can be used in a subsequent Cu_2O deposition step. Yet a barrier to making a device still remains. Traditionally, devices made on bulk substrates or thin films use conductive substrates which facilitates adding front or back contacts. The small lattice mismatch between Cu_2O and ZnO is one of the primary reasons for its use. While an exhaustive literature search revealed several materials with lattice parameters very close to that of Cu_2Os , their lack of structural, mechanical and thermal stability away from standard pressure and temperature automatically

disqualified their use as a choice. Two compounds were discovered that were very soluble in water and that were relatively lattice matched to Cu_2O: cesium chloride (CsCl)[52], with a lattice constant of 4.11Å(4% mismatch), and cesium bromide (CsBr)[53], with a lattice constant of 4.28Å(practically zero mismatch). However, both compounds have melting temperatures in the 600-700 ^oC range, which is too low for Cu_2O growths using the MBE. Several different ideas were considered in order to place a back contact on Cu_2O. These included using lateral contacts, etching through the MgO substrate and even patterning a contact grid on the substrate prior to deposition of the hetero-structure. In theory any of these would work if properly if engineered properly. Cu_2O is pretty resistive therefore lateral contacts would introduce a large amount of series resistance. Pre-patterning back contacts would likely destroy the epitaxial relation between the thin film and substrate as well as diffuse throughout the structure during the deposition process. Etching through the MgO substrate to make contacts is only viable if dry etching is considered as wet chemistry etching would not have enough selectivity to etch away a thick MgO substrate before either damaging or etching away the hetero structure. After giving the issue thoughtful consideration, we decide that photolithography offered the best solution. While MgOs lack of electrical conductivity is the reason why making electrical contacts is difficult to being with, it least offers some advantages in a photolithography process. Because MgO is transparent, the entire cell can be flipped over thus operating the cell in an upside down configuration where the light would pass through the MgO and be absorbed first by Cu_2O. This design automatically provides a protective top layer to the cell (MgO) in addition to not losing current due to shadowing loss of a metal contact grid. Therefore, the focus of creating metallized contacts shifted to using photolithography-assisted etching to create an all-front contact pattern. A photolithography mask pattern was designed to for etching through the ZnO layer ($\approx$ 150 nm thick), exposing Cu_2O to then be contacted. The pattern (figure 3.9) was designed with fingers to minimize the amount of ZnO etched away on the device, while still exposing enough Cu_2O to reduce the distance traveled by carriers and therefore to minimize the sheet resistance. In addition, a complementary pattern was designed

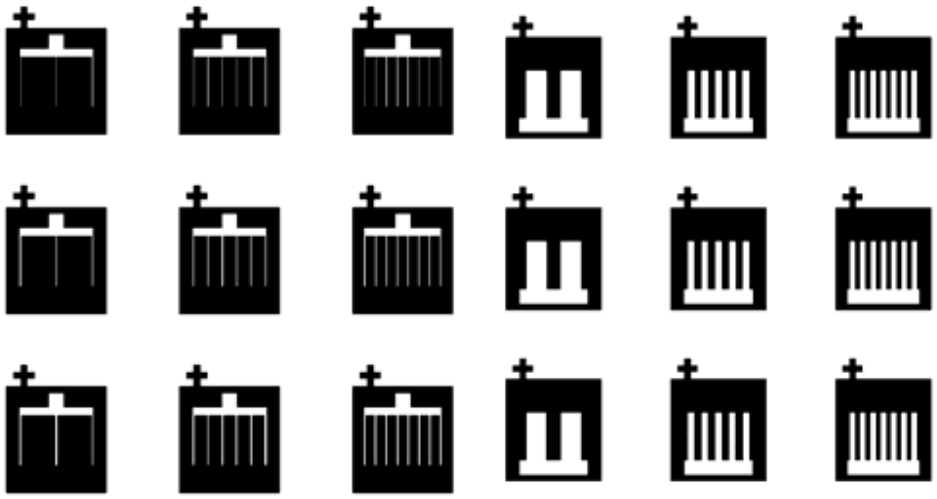

Figure 3.9. Photomask designs used for metallization.

(figure 3.9) for contacting ZnO if an additional metallization step was needed, such that the fingers would interlace with the fingers from the Cu_2O pattern. Markers were located at the top of both patterns, to allow for easy alignment. In order to minimize the number of photolithography steps, the deposition of ITO or another TCO on top of ZnO before any photolithography steps would be sufficient as contacts for ZnO. In order to determine the optimal design, an array of nine patterns was designed with varying finger widths (5, 10, and 15 μm) and finger spacings (150, 200 and 500 μm). The fingers were 700 μm in length, and each pattern was roughly 1 mm in width, which allowed for all 9 devices to be patterned on one 1 cm x 1 cm stack of $MgO/Cu_2O/ZnO$. Additionally, the patterns each have a 200 μm x 200 μm square tab at the top, which allows for easy probing when performing measurements.

Similarly, nine ZnO patterns were aligned on the mask, each corresponding to one Cu_2O pattern.Two different types of photoresist were used in order to create an overhang and avoid shorting the device. First, 3A liftoff resist (LOR) was applied on top of the ZnO, with spin settings of 1500 rpm for 40 seconds, followed by a five minute bake at 160 ^oC. Next, 1813 positive resist was applied, with spin settings of 300 rpm for 60 seconds, and a 120 second bake at 115 ^oC. The samples were then patterned (exposure for 70 seconds) and developed in MF-319 for 80 seconds. Because LOR

3A has a higher dissolution rate than 1813 resist, the result is an overhang therefore, when the ZnO is etched, the feature size will match that of the overdeveloped LOR, whereas when metal contacts are deposited, they will match the smaller feature size of the 1813. This allows for extra space between the contact and the walls of the ZnO layer, avoiding any possibility of shorting the device.

For the etching process, different chemical etchants were explored. It was determined that, as was the case with etchants of MgO, most known etchants of ZnO tend to react with all metal oxides (including Cu_2O). However, because the ZnO layer is on the order of 150 nm and the Cu_2O layer is significantly thicker at roughly 2-3 μm, a timed etch that does not completely eat through the Cu_2O would be possible. Different concentrations of HNO_3 (nitric acid) were used for varying amounts of time, in order to determine the optimal conditions for etching through the ZnO layer. After the etching process was completed, samples were contacted using either metal evaporation or sputtering of gold and Remover PG was used to liftoff the metal from the unpatterned parts of the sample. You may reference appendix B to see a flow diagram of the process described above.

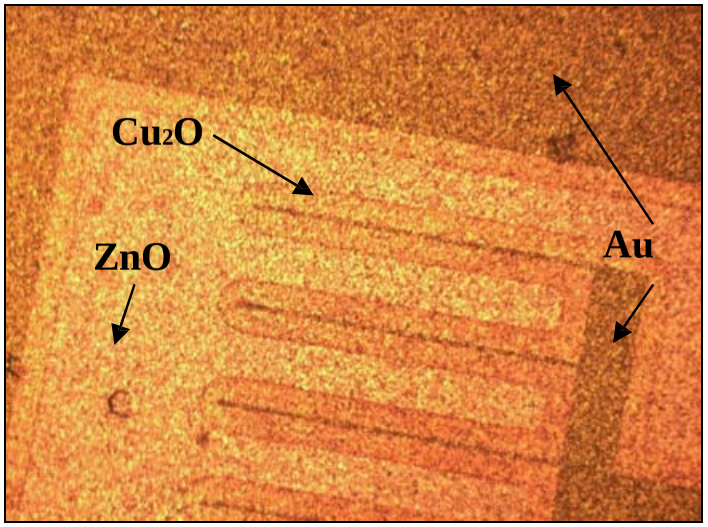

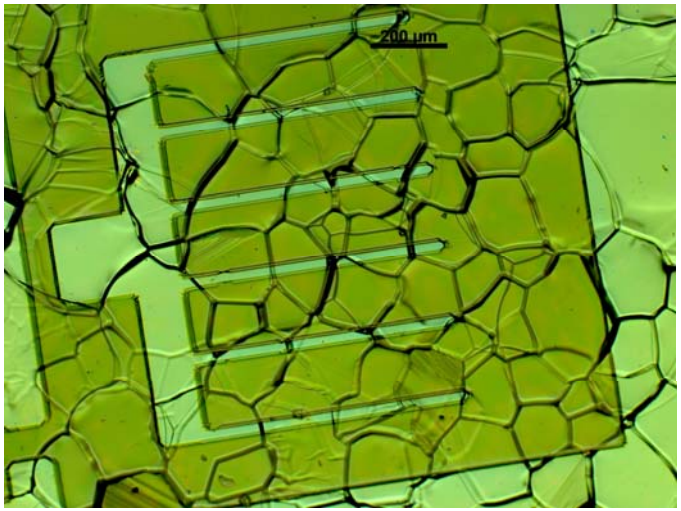

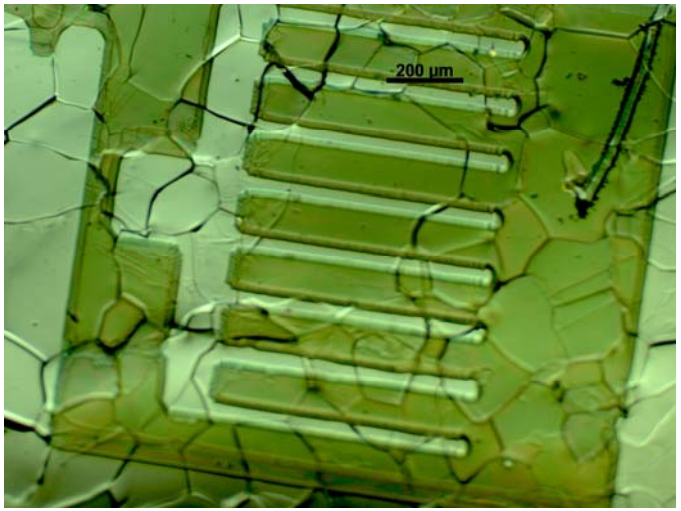

Figure 3.10. Optical micrograph images of heterostructures being paterned.

3.7 Cu_2O/ZnO Hetero-structure Devices

The devices fabricated above were tested contact side up with gold probe tips contacting both the ITO layer (ZnO) and contacting the gold contact pads patterned during photolithography. Many of our samples exhibited no photovoltaic properties. This was likely attributed to some steps during the lithography process as devices made from Cu_2O substrates went from exhibiting photoresponse to no photoresponse right after lithography. The last series of devices fabricated had IV curves that indicated photovoltaic activity was present. Still these devices had very low current densities and fill factors, indicative of series resistance. Figure 3.11 shows the photovoltaic performance of the cell under simulated AM 1.5 illumination. The cell if figure 3.11 has a fill factor of 26% V_{oc}= 515mV and J_{sc} ≈.8, and the cell in figure 3.12 has a fill factor of 35.6% V_{oc}= 520mV and J_{sc} ≈3.78. We would expect slightly greater performance from these cells via increase in open-circuit voltage had the contacts been annealed. Unfortunately the conditions at which the anneal took place damaged the devices.

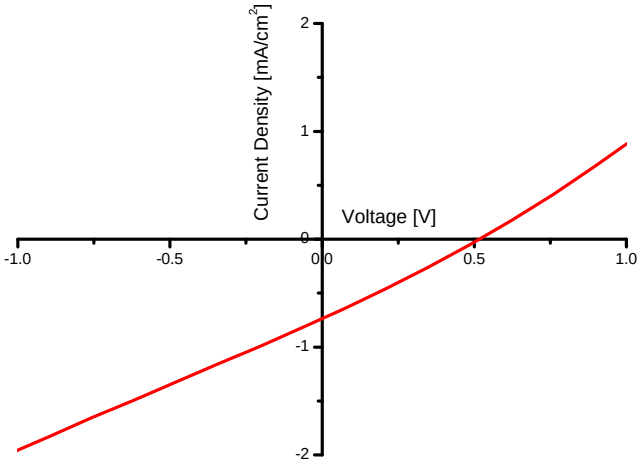

Figure 3.11. FF=26% ,V_{oc}= 515mV, J_{sc} ≈=.8

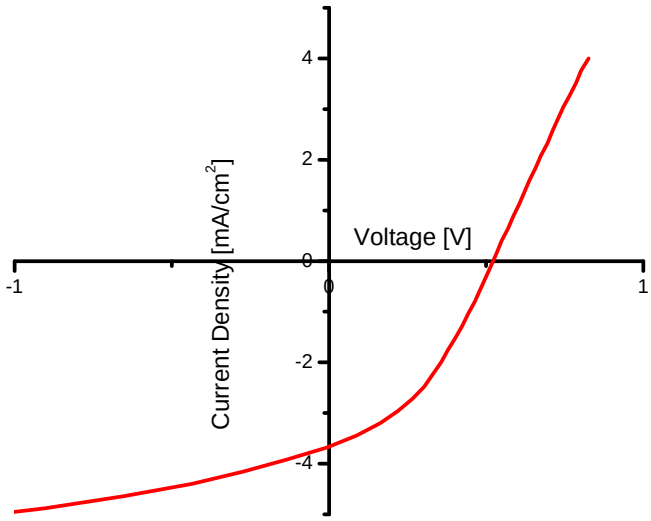

Figure 3.12. FF=35.6% ,V_{oc}= 520mV, J_{sc} ≈3.78

Chapter 4

Synthesis of Cu_2O Templates and Bulk Substrates via Thermal Oxidation

In this chapter we present growth techniques and conditions used to synthesis bulk cuprous oxide samples. Post growth processing of these samples in one of two ways will determine their use. The first way will directly incorporate them into a photovoltaic device therefore we quickly look at methods to dope and increase conductivity of these samples so that they exhibit better performance as the active layer in a photovoltaic device. They may also be used as templates for subsequent homoepitaxy of higher quality Cu_2O material.

4.1 Cu_2O Synthesis from Oxidation of Copper Foils

The most common method and easiest method create Cu_2O is by thermal oxidation of Copper foils in a furnace. Referring back to figure 1.6 and the discussion in section 1.4.3 on the Cu-O phase diagram, we know that it is possible to make Cu_2O in various conditions. Using a vacuum furnace allows us to be practically anywhere in the phase stable region of Cu_2O in the phase diagram and is the most versatile method for oxidation of copper foils. Generally, the procedure involves the oxidation of high purity copper at an elevated temperature for times ranging from few minutes to a few hours depending on the thickness of the starting material. The oxidation process can be carried out either in pure oxygen or air. Commercially available copper foil at a purity of 99.999% was purchased at a variety of different thicknesses ranging from 10 to 500 microns from ESPI metals. As previously discussed, Cu_2O only needs several microns

of material for full absorption but handling foils that thin is impractical. Cu_2O is a brittle material and the sole purpose of using thicker foils was for mechanical stability and handling reasons. The impurity analysis for the foils is provided in table 4.1.

Table 4.1. Impurities concentrations in ppm found in Cu foil.

Element	Purity
Ag	0.3
As	1
Bi	0
Ca	0.1
Fe	0.1
Mn	0.2
Ni	0
Pb	0.1
Sb	1
Si	0.2
Sn	0.2

The copper foils were precut to .5"x.5"squares and had a hole placed along the top of the square. The whole was used to hang the foil to a quartz boat specially designed for this process. Copper wire of the same purity also purchased from ESPI metals was used to hang them. This was done in order to reduce the likelihood of contaminating the substrates as well as to prevent the reaction of copper oxide with quartz which cause the two materials to fuse together. The copper foils were cleaned and packed in a class 10 clean room, therefore no cleaning steps were performed prior to oxidation of the foils. Large grained polycrystalline substrates were synthesized by thermal oxidation of $100\mu m$ thick copper foils. Oxidation was initiated by evacuating the tube furnace to a pressure less than $5x10^{-5}$ torr followed by heating the furnace to a temperature of 1010^oC. Once the system reached a stable 1010^oC., the temperature

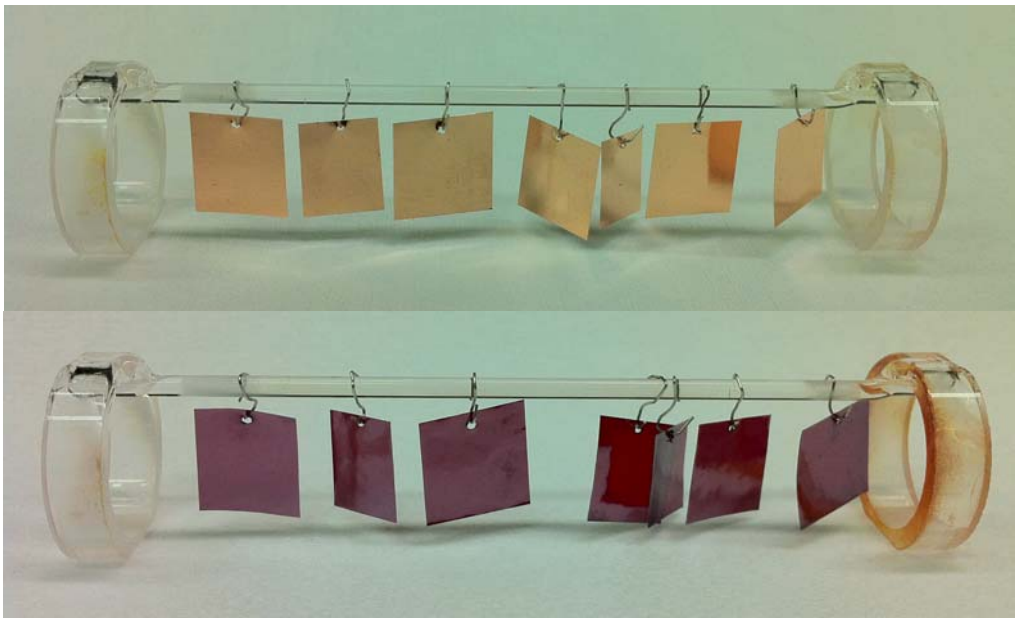

Figure 4.1. Cu foils pre and post oxidation in a vacuum furnace at 1010^{o}C.

at which our oxidation takes place, a leak valve introducing ultra high purity oxygen in the tube was opened where the oxidation of the copper foils commenced at a pressure of 5 torr for 2 hours. following oxidation, the vacuum furnace was quarreled through a stepwise process down to room temperature under successively decreasing oxygen pressures in order to stay within the phase stable region of Cu_2O in the Cu-O phase diagram. A schematic for our process is shown in figure 4.2.

Using a vacuum furnace is far more advantageous than a traditional tube furnace because one is able to control both pressure and temperature of the sample whereas in a standard tube furnace one really only has control over temperature. This allows samples of varying electronic properties and grain sizes to easily be made. Remember that electronic properties of the substrates depend on the region in the phase diagram they were processed at and by processing samples at lower temperatures fewer defects are introduced and therefore the samples have higher mobilities and are more conductive. In addition the ability to control the oxygen pressure prevents the deleterious side reaction of cuprous oxide going to cupric oxide. In the case where cupric oxide is formed on the surface a quick dip high molarity nitric acid removes

it immediately. Other etch methods such as bromine methanol or hydrochloric acid has been used by others in literature, but we found that they are not necessary and often times leave behind other impurities or form new surfaces that are even harder to remove than CuO such as CuCl. A photograph showing Cu foils before oxidation and the resulting cuprous oxide substrates after oxidation is show in figure 4.1. The following are observational notes and hints for making bulk substrates using thermal oxidation.

- Grain sizes on the order of cm's may be obtained by annealing samples at high temperature for a long period of time.
- Impurities largerly influence grain size and microstructure below 1000^oC[**?**].
- The oxidation process is one where V_{Cu} diffuse into the substrate and for sufficient thickness forms a plane of voids called the inner porous layer.
- It is interesting to note that even at 450C the copper vacancies can diffuse up to 70μm, the minimum distance to to reach the surface of our 150 μm thick samples in about two minutes.
- Without a doubt thin layers of Cu_2O are the way to go but it is important to handle the samples with lots of care otherwise they disintegrate into powder. Using a handle substrate after the initial oxidation saves a lot of time .

4.1.1 Characterization of Cu_2O substrates

X-ray diffraction data was collected by a Philips XRD with Cu Kα radiation was collected and plotted (figure 4.3). All the peak present were indexed and they indicated that our substrates were composed of phase pure Cu_2O. Subsequently a substrate was cut down to size and had gold contacts evaporated at room temperature to its four corners using a shadow mask in order to conduct room temperature Van der Pauw and Hall effect measurements. As expected, the polycrystalline Cu_2O substrates were found to be p-type with a hole concentration

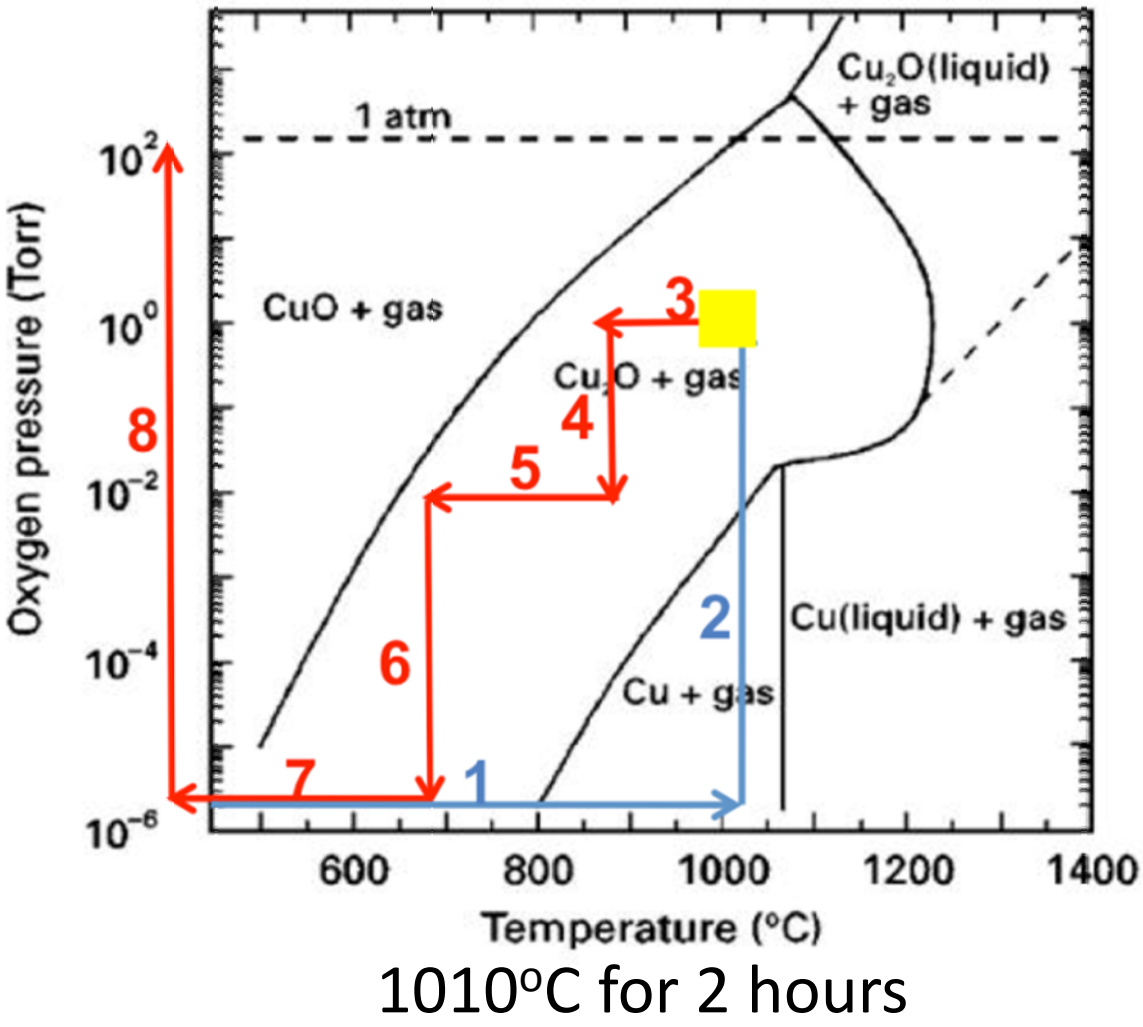

Figure 4.2. A detailed schmatics illustrating the process and conditions for oxidation of copper foils to Cu_2O

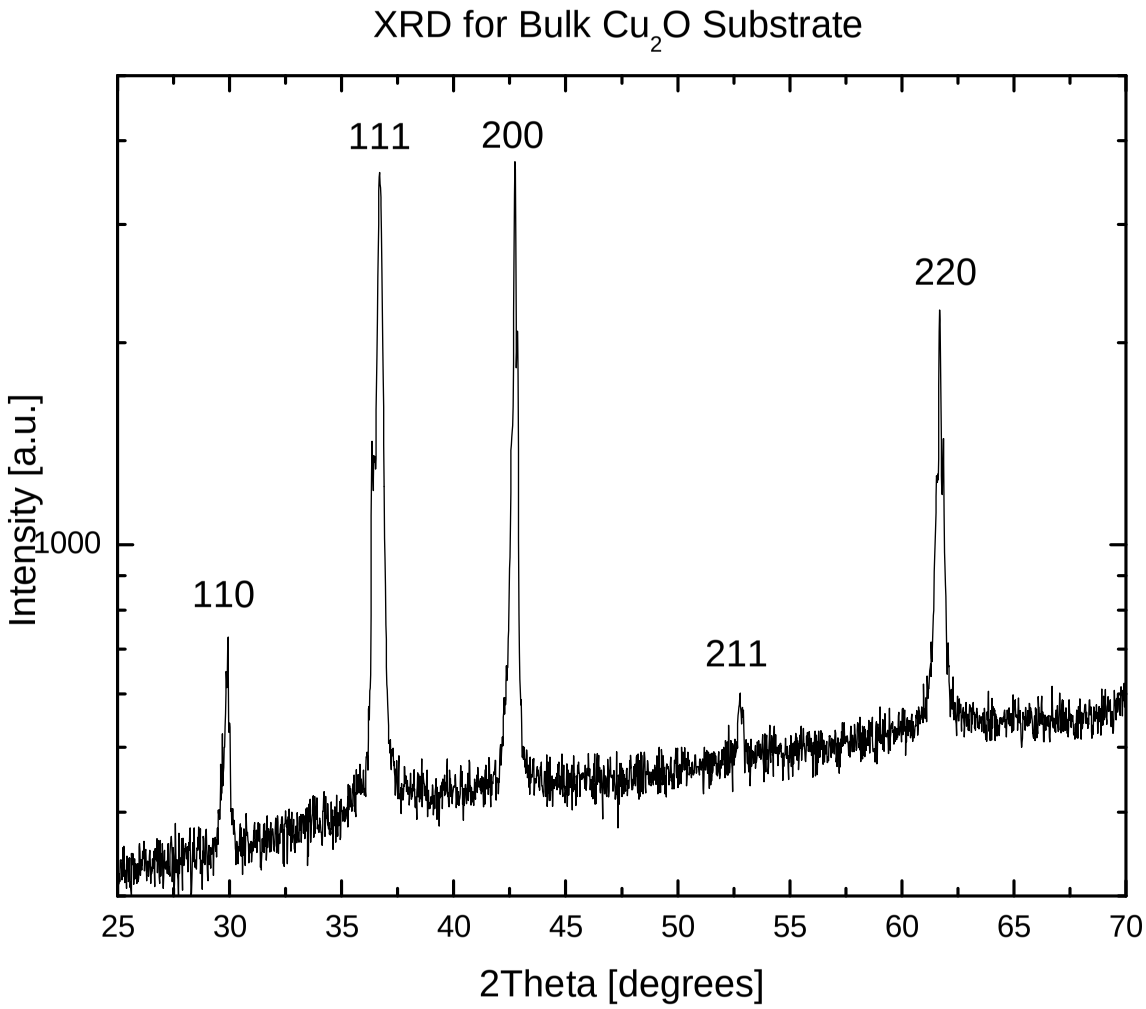

Figure 4.3. X-ray diffraction measurement of a bulk substrate showing phase pure Cu_2O

of $7x10^{13}\frac{\text{atoms}}{\text{cm}^3}$ and a Hall mobility of roughly 60 $\text{cm}^2 \cdot V^{-1} \cdot \text{sec}^{-1}$ which compared to literature values[37, 54] as well as measured values for our own thin films. Spectroscopic ellipsometry was performed in a procedure identical to the one done for our thin film samples (this procedure will be detailed in its own section) and the resulting absorption data was consistent with the reported bandgap of 2.0eV.

4.2 Extrinsic Doping of Cu_2O Substrate

The substrate that were produced and described above turn out to be quite similar to our "base-structure" used in our simulations in chapter 2. Because of this, it should be quite obvious that the next step in processing the samples in order to make a device involves finding methods to extrinsically dope our material. Many attempts have been made to further dope copper oxide without destroying minority carrier diffusion lengths[55, 56, 57]. Among the impurities investigated up to now, only three of them have given a a slight increase in conductivity: silicon, nitrogen and chlorine though their mode of action is still not understood. As for other elements, there are several that increase p-type carrier concentration even by several orders of magnitude but do it at the expensive of decreasing carrier mobility near zero thus conductivity remains unchanged or is even worse. Our first attempts at doping Cu_2O involved either evaporating a thin film of our dopant material or measuring a small amount of the dopant material and placing it in a sealed tube along with a prepared Cu_2O substrate and annealing the sample in a furnace. This method is also known as the "drive-in" method that is most commonly used with silicon semiconductor devices. As previously mentioned Cu_2O is metastable at room temperature and the reason why it does not spontaneously transform to CuO is because of extremely slow reaction kinetics. But at slightly elevated temperatures (above 200 degrees C) kinetics no longer are a barrier to the diffusion of Cu around the lattice and instead of incorporating our dopant atom into our Cu_2O lattice, Cu drives out of the

lattice and either reacts with the alloy material thus being reduced from Cu^{+} to Cu or dependent on the dopant source the exact opposite can happen where Cu^{+} transforms to Cu^{2+}, and based on how the results are very similar to the deleterious reactions that occur at occur at the heterojunction interface, we have concluded that this method, at least done this way, is not a viable method for doping Cu_2O with any element. Our simulations also taught us that doping is extremely important due to the fact that cuprous oxide homojunctions are impossible to make, but at the same time introducing "dopants" into the material will likely create a more compensated Cu_2O substrate that has poor electrical properties. In order to avoid allowing the system to equilibrate post introduction of the dopant atoms, two methods for doping Cu_2O were tried. The first method involved starting with foils of Cu alloyed with whatever we wanted our dopant to be as opposed to pure copper foils. Then the rest of the oxidation steps were identical to that of oxidizing a pure copper foil. Using this method, we hoped the system would avoid creating extra point defects to compensate the dopant atoms. We specifically focused used Ni and Zn as our dopant atoms as they sit directly to the right and left of copper in the periodic table.

Table 4.2. Hall Measurements of Alloyed Substrates

Dopant	Carrier Conc. [cm^{-3}]	Mobility [$cm^2 \cdot V^{-1} \cdot sec^{-1}$]	Carrier Type
Ni	$2.45x10^{13}$	24.8	p-type
Zn	$7x10^{10}$	5.1	p-type

The results summarized in the table 4.2 were quite disappointing.In addition the morphology of the substrates looked different when compared to the same process done to pure Cu foil. We decided to use time of flight secondary ion mass spectroscopy, or TOF-SIMS[58] to probe the chemical composition of the surface as well as obtain a chemical composition vs thickness of sample plot to see if our dopant atoms were doing anything unexpected such as segregating at

surfaces or grain boundaries or if they were starting to precipitate out of solution. The TOF-SIMS measurement were conducted by Lynelle Takahashi at the Dow Chemical Company. Because of the amount of work, time and cost involved in these measurements we started with our Zn doped samples as they seemed most interesting.The following are general notes about the SIMS method.

- ToF-SIMS can detect the positive or negative ions from a surface from the top few nm.
- A 25 keV Bi+ probe is used to for imaging and can focus down to to sizes below 100 nm.
- There is a tradeoff between spatial resolution and mass resolution, thus knowing either the species your are looking for or the area you are searching you will obtain much better data.
- Similar to ion beam milling, Cs atoms are used to sputter away layers for depth profiles.

The measurements taken using the TOF-SIMS threw another twist into this already difficult problem. SIMS analysis was unable to detect amy dopant atoms in our Cu_2O substrates after the alloyed foils were oxidized. Because of the the large concentration of impurity atoms we started with it was surprising that we saw none at all. We prepared SIMS standards which needed to be used in order to determine the detection limit of each element in our lattice. The detection limit is a function of the lattice being looked at so standards must be created for each and every sample that one wants to look at and get conclusive quantitative results. The SIMS standards were created by sending our copper oxide substrates to a commercial ion-implantation foundry to have a specific dose and energy of our dopant atoms implanted into our samples. Then using the free software SRIM and TRIM[59] we were able to conduct ion implantation monte-carlo simulations with the same conditions that our real samples were being subjected

to. Finally the ion implanted samples once again were submitted for analysis to determine at what point did the system no longer detect the implanted ion (i.e. when the detection level reaches the background noise level) and it turned out to be much higher than we thought. This number corresponds to $1.98x10^{10}cm^3$ while we are interested in detecting doping levels 5 to six orders of magnitude below that value concluding that this method is not viable for further use for our purposes. The last interesting thought to note is that most of these methods required some sort heating step or treatment step that made knowing the carrier concentration and profile almost impossible, especially with copper's ability to diffuse around the lattice quite quickly (several microns a minute at 500 degrees celcius). Ion implantation of dopants has not been studied or reported on at all for Cu_2O, and using light elements like Lithium who also have an electronic configuration like that of Cu in Cu_2O needs further investigation. Typically ions as light and small as Li^+ get implanted in interstitial lattice sites. The implantation conditions can be conducted such that there is no heating of the substrate during implantation and thus no chance for Li^+ to move around and no chance for the Cu_2Os crystal to thermodynamically equilibrate thus preventing self compensation mechanism from happening. It is clear to me that Cu_2O solar cells will not see progress above the 6-8% efficiency range if an extrinsic dopant is not part of the heterojunction cell design.

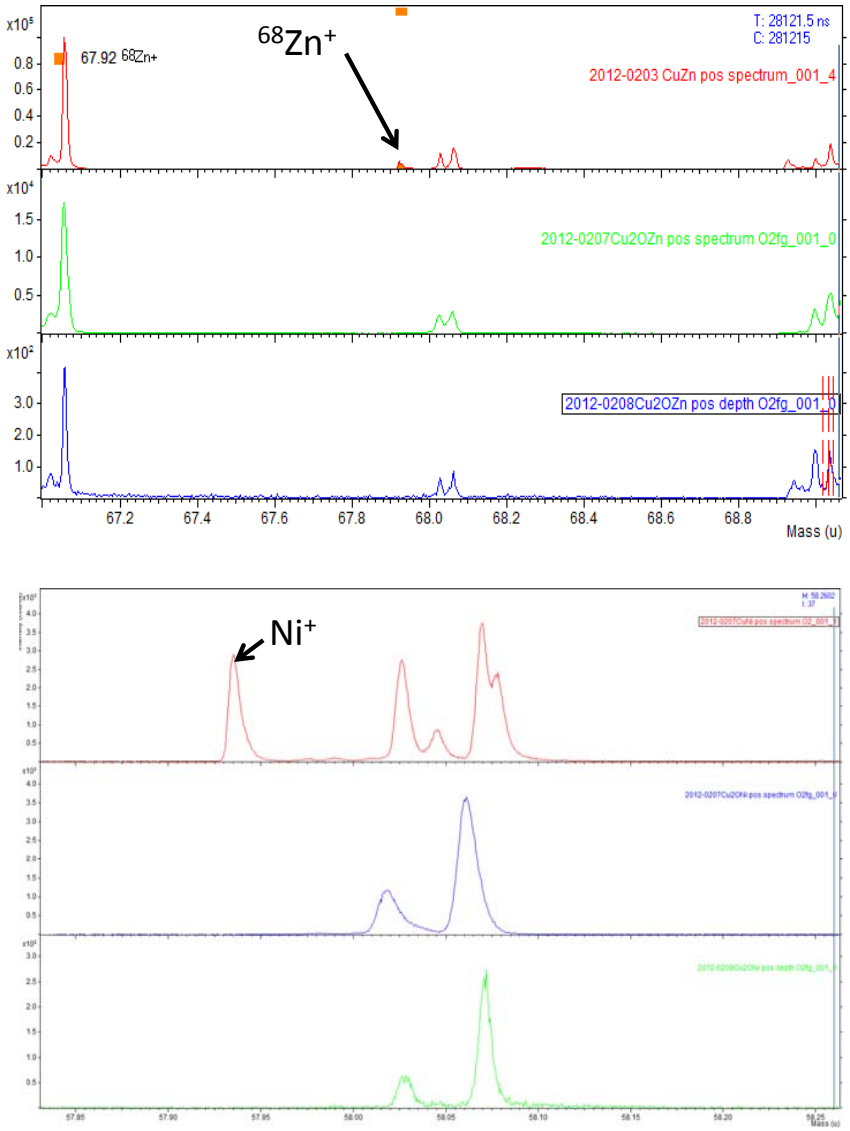

Figure 4.4. TOF-SIMS data showing dopant atom detection prior to but not after oxidation of alloyed films.

4.3 Cu_2O Templates Fabricated by Thermal Oxidation

In this section, the motivation and background work laid out by others, for other materials systems, will be presented. Then preliminary work and proof of concept work done for Cu_2Os will be shown.

A templated substrates would be a thin film process engineers dream. That is because they provide a lattice matched substrate for the subsequent deposition material to grown on, they can infinitely simplify the method needed to create contact to said layer, and can dramatically decrease the cost of a cell by replacing the bulk substrate used with one that is composed of much cheaper materials or creating only a thin layer of the template on top of a cheap substrate like glass such that only a small fraction of expensive material is being used in comparison to before. The essential goal is to create a template substrate that is cheaper than the substrate material it is going to replace, that can be used for subsequent epitaxial thin film growth.

The first approach involved direct utilization of the Cu_2O substrates as the templates. In order for this to work the samples needed to be etched with a quick dip nitric acid or if they were not specular or planar enough then they would need to be lapped using diamond abrasive films, and polished in a colloidal silica slurry (South Bay Technology), to produce substrates that had a specular finish. Another method for use of bulk substrates as templates was the use of in-situ ion beam sputtering which under the right conditions would allow one to both to both clean and somewhat planarize the surface of our substrate prior to thin film deposition of the active layer[60, 61, 62]. Figure 4.3 has a series of RHEED images that shows the transformation of morphology from a dirty pretty much amorphous surface to a cleaned deposition ready surface as evident by the appearance of diffraction spots and ring that were not there moments before.

The last approach I would like to discuss is a method known as surface oxidation epitaxy[63]. It is method that is most commonly used with Ni metal in the

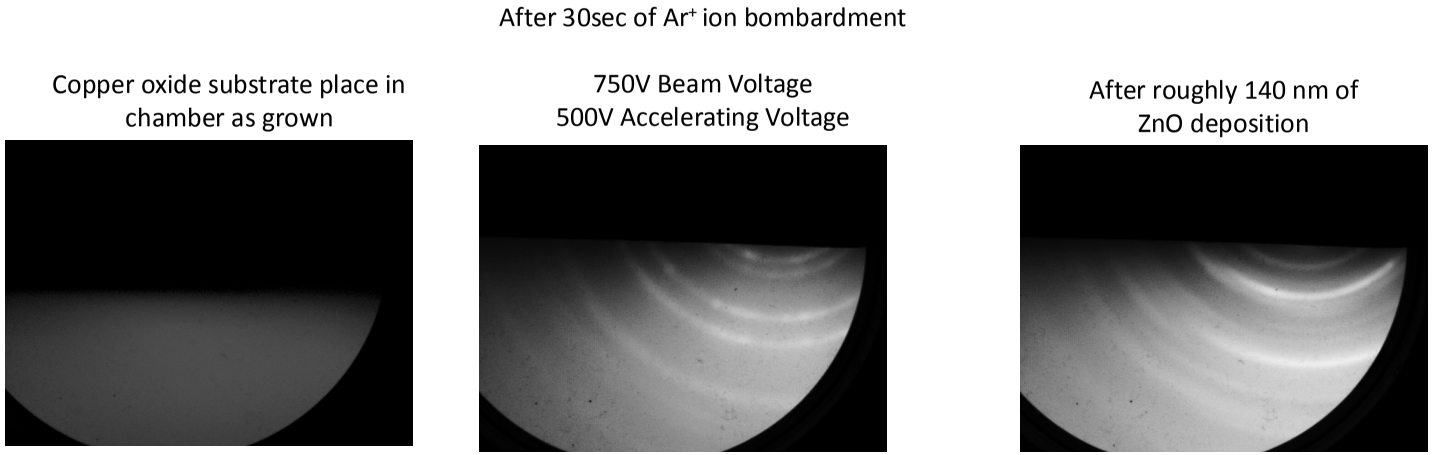

Figure 4.5. In-situ ion beam sputtering used to clean an as grown thermally oxidized substrate followed by subsequent deposition

superconductor field of research but the methods can be extended to be used with Cu as well. Using either nickel foils or nickel thin films deposited via evaporation as the starting material, very great care and attention is paid to avoid pre-oxidation of the surface at lower temperatures. Then sample then goes through a surface treatment and annealing all pre-oxidation before conditions in the furnace are set at such that nucleation control surface oxidation epitaxy is favored over competitive grain growth. Shi et. al. mentioned that they believed the critical steps for ensuring the method worked and that it was reproducible was to place the samples at very high temperature and anneal then for several hours in forming gas. Consequently, cube textured epitaxial NiO layers of around 1μm were grown on pure Ni. In figure 4.6 the top two plots show results from Shi et. al. and below are results from applying the very same principals to form cube on cube copper and to suppress as many different crystallographic orientations as possible.

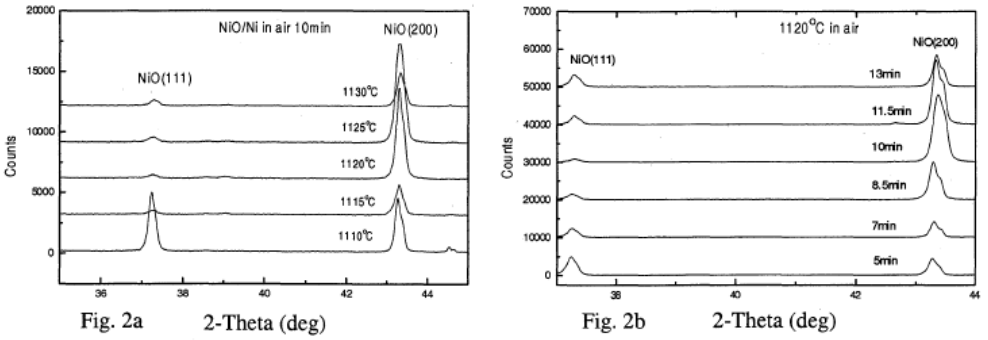

Fig. 2a Fig. 2b

1hr forming gas anneal at 1000°, followed by 3hr oxidation in Air. Cooled during high flow nitrogen purge.

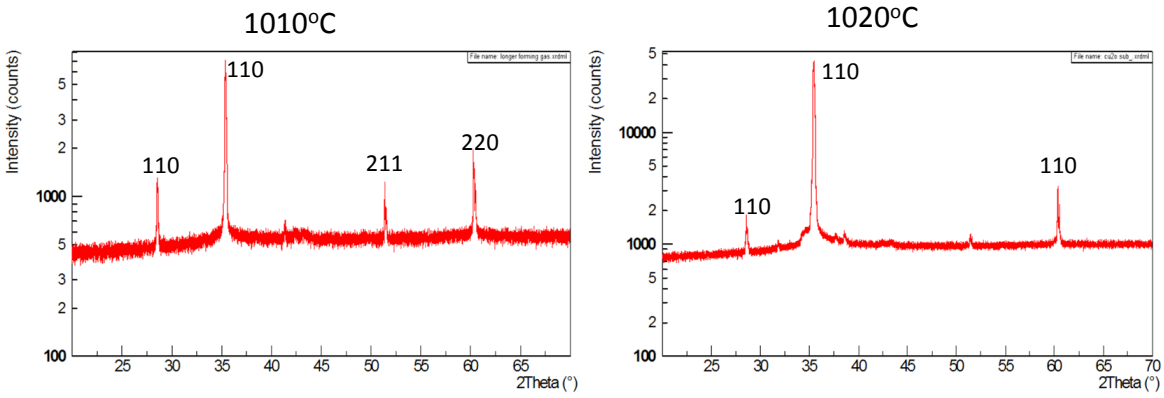

Figure 4.6. An example of orientation suppression and cube on cube epitaxy using Surface oxidation Epitaxy both on Ni and Cu to produce NiO and Cu_2O

Chapter 5

Final Thoughts

This work tried to better understand the fundamental reasons why Cu_2O solar cells have been unable to reach much higher efficiencies. Clearly, intrinsic defects are holding progress back because they are necessary in order to have a conductive sample and at the same time unwanted because they decrease the minority carrier lifetime and cause lots of recombination. It is the battle between high open circuit voltage or a larger current and it looks like that problem is close to being maximized. In order to get over this hump, I believe a majority of the efforts should go toward doping experiments or methods of engineering ultra thin layers. We can conclude from the simulation in chapter two that there is no substitute for finding an extrinsic dopant if we want to process samples easily by using foils in a furnace. Molecular beam epitaxy has allowed single crystal like material to be grown while both kinetically controlling defect concentrations and allowing films to stay ultra thin. We have achieved epitaxial growth of Cu_2O and ZnO on both single crystal MgO and IBAD MgO substrates. In addition more recently we have been successful in textured growth of MBE grown Cu_2O on Cu_2O bulk substrates. While MgO is a good substrate, nothing can replace a Cu_2O substrate for subsequent Cu_2O thin film deposition. While MgOs lack of conductivity has made it a less than popular choice of substrate when making contacts, our interdigitated contact design seems to get around all barriers and as a bonus provides the benefit of protecting our heterostructure. It is clear that the demand for clean and cheap energy is here and is not leaving. Whether or not Cu_2O turns out to a major part of that solution remains to be seen but it is

certain that no matter what, the fundamental of science that we learn from our research of Cu_2O will play a big role in how we study other materials. It is clear that both the need and demand for clean and cheap energy is present and is not leaving. Whether or not Cu_2O turns out to play a major role in solving the worlds energy needs remains to be seen, but it is certain that no matter what the fundamental science learned from the research of Cu_2O will play a big role in how we study other materials.

Appendix A

Matlab Code for Detailed Balance Model

```
function [Ei,Es,J,V,P,Jn,Vn,Pn] = detailedbalance_multi(T,C,Eg,ni_top,ni_bot,

% Detailed Balance Calculations for a 'N' multi-junction Solar Cell
% Determine number of junctions
Nj=length(Eg);

% Constants
hbar=1.05457148e-34; %m2kg/s
c=299792458; %m/s
k=1.3806503e-23; % m2kg/s2K
q=1.60217646e-19; %C
kT=k*T/q;

% First define the refractive index of the substrate the cell is on
% If on a solid reflective back metal contact, nibottom=0, otherwise, use n o
% substrate material.  The etendue defines the total escape area for
% radiative emission from the cell.  Radiative emission is the only loss
% mechanism in detailed balance calculations.

% The total current in the cell is equal to the difference between the genera
% electron hole pairs from photons and radiative recombination of electron
% hole pairs.  For every photon that enters the material greater than or
% equal in energy to the band gap of the material, one electron hole pair is
```

```
% created.

etendue=ni_top*pi+pi*ni_bot.^2;

load E_flux                                          % E in eV and flux in 1/cm2eV
Ltot = 1240./E;                                     % wavelength in nm
Pdens = E.^3.*flux*10000*1.6E-19/1240;               % Power density in W/(cm2 nm)


% Number of electron-hole pairs photogenerated, Ngen [=] 1/cm2-s and
% photocurrent Jgen [=] C/cm2-s [=] A/cm2
num=1000;
n=length(flux);

% for Eg(1) must calculate separately...
m(1)=length(E(E≤Eg(1)));
Ngen(1,1)=C*trapz(E(m(1):end),flux(m(1):end));
if Nj>1
    for i=2:Nj
        m(1,i)=length(E(E≤Eg(i)));
        if Eg(i)≥Eg(i-1)
            Ngen(1,i)=0;
        else
            Ngen(1,i)=C*trapz(E(m(i):m(i-1)),flux(m(i):m(i-1)));
        end
    end
end
Jgen=q*Ngen;


v=zeros(num,Nj);
x=zeros(num,Nj);
for i=1:Nj
    v(:,i)=linspace(0,Eg(i)-0.001,num)';
    x(:,i)=logspace(log10(Eg(i)),log10(Eg(i)+10),num)';
end
```

```
60
61
62 N=zeros(num,Nj);                    % N is in units of eV^3
63 Nc=zeros(n-1,num,Nj);
64 Jrad=N; Jtot=N; Pn=N;
65 for j=1:Nj
66     for i=1:num
67         N(i,j)=trapz(x(:,j),x(:,j).^2./(exp(x(:,j)/kT)-1)-x(:,j).^2./(exp((x(
68     end
69     Jrad(:,j)=(q^3*N(:,j)).*etendue(j).*q./(4*pi^3*hbar^3*c^2*100^2);       %
70     Jtot(:,j)=Jgen(j)+Jrad(:,j);
71     Pn(:,j)=Jtot(:,j).*v(:,j);
72 end
73
74
75
76 % Meshing the current vectors and splining the V to add them
77 dJn=diff(Jtot);
78 Jn=NaN(n,Nj);
79 Vn=NaN(n,Nj);
80 for i=1:Nj
81     Ji=Jtot(:,i);
82     Vi=v(:,i);
83     o=length(Ji(dJn(:,i)~=0));
84     Jn(1:o+1,i)=[Ji(dJn(:,i)~=0); Ji(end)];
85     Vn(1:o+1,i)=[Vi(dJn(:,i)~=0); Vi(end)];
86 end
87
88 J=[];
89 for i=1:Nj
90     J=[J; Jn(:,i)];
91 end
92 J=sort(J); J=-J;
93 J=sort(J); J=-J;
94 dJ=diff(J);
95 J=[J(dJ~=0); J(end)];
```

```
96
97  for i=1:Nj
98      Jv=Jn(:,i); Jv(isnan(Jn(:,i)))=[];
99      Vv=Vn(:,i); Vv(isnan(Jn(:,i)))=[];
100     Vinterp(:,i)=interp1(Jv,Vv,J,'nearest');
101 end
102 V=sum(Vinterp,2);
103
104 % Power = J*V
105 P=J.*V;
106 xmax=find(P==max(P));
107 Pmax=P(xmax);
108 Vmax=V(xmax);
109 Jmax=J(xmax);
110
111
112 %Efficiency
113 Psun=q*C*trapz(E,flux.*E);
114 En=max(Vn.*Jn)/Psun;
115 Ei=sum(En);
116 Es=Pmax/Psun;
117
118
119
120 if figson==1
121     figure
122     plot(Ltot,Pdens,'k-','LineWidth',1.2); hold on
123     fill([Ltot(m(1));Ltot(m(1):end);Ltot(end)],[0;En(1).*Pdens(m(1):end);0],s
124     if Nj<2
125     else
126         for i=2:Nj;
127             fill([Ltot(m(i));Ltot(m(i):m(i-1));Ltot(m(i-1))],...
128                 [0;En(i).*Pdens(m(i):m(i-1));0],...
129                  spectrumRGB(mean(Ltot(m(i):end))))
130         end
131     end
```

```
132     Leg(1)={'Solar spectrum'};
133     for i=1:Nj; Leg(i+1)=strcat({num2str(Eg(i))},{'eV'}); end
134     legend(Leg)
135     ylabel('W m^{-2} s^{-1} nm^{-1}')
136     xlim([200,2000])
137 else
138 end
139
140
141 % Meshing the current vectors and splining the V to add them
142 % % % J1=Jtot(:,1);
143 % % % J2=Jtot(:,2);
144 % % % dJ1=diff(J1);
145 % % % dJ2=diff(J2);
146 % % % J1=[J1(dJ1≠0); J1(end,1)];
147 % % % J2=[J2(dJ2≠0); J2(end,1)];
148 % % %
149 % % % v1=V(:,1);
150 % % % v2=V(:,2);
151 % % % v1=[v1(dJ1≠0);v1(end)];
152 % % % v2=[v2(dJ2≠0);v2(end)];
153 % % %
154 % % % J=[J1;J2];
155 % % % J=sort(J); J=-J;
156 % % % J=sort(J); J=-J;
157 % % % dJ=diff(J);
158 % % % J=[J(dJ≠0); J(end)];
159 % % %
160 % % % V1=interp1(J1,v1,J,'nearest');
161 % % % V2=interp1(J2,v2,J,'nearest');
162 % % %
163 % % % V=V1+V2;
164 % % % P=J.*V;
165 % % % maxP=max(P);
166 % % %
167 % % % Psun=q*C*trapz(E,flux.*E);
```

```
168 % % % IndEff=(max(v1.*J1)/Psun)+(max(v2.*J2)/Psun)
169 % % % SeriesEff=maxP/Psun
170
171
172 % x_oc=find(Jtot≤0,1,'first')
173 % maxP=P(x_max)
174 % maxV=V(x_max)
175 % maxJ=Jtot(x_max)
176 %
177 % Voc=V(x_oc)
178 %
179 % figure
180 % plot(V,Jtot,'k-','LineWidth',1.5); hold on
181 % plot(maxV,maxJ,'ro','MarkerSize',6,'MarkerFaceColor','r')
182 % plot([0,maxV],[maxJ,maxJ],'r--');
183 % plot([maxV,maxV],[0,maxJ],'r--');
184 % plot(Voc,0,'ko','MarkerFaceColor','k')
185 % ylim([0,1.2*max(Jtot)])
186 % xlim([0,1.1*max(Voc)])
187 %
188 % %Efficiency
189 % Psun=q*C*trapz(E,flux.*E)
190 % Eff=maxP/Psun
```

Appendix B

Photolithography Flow Process

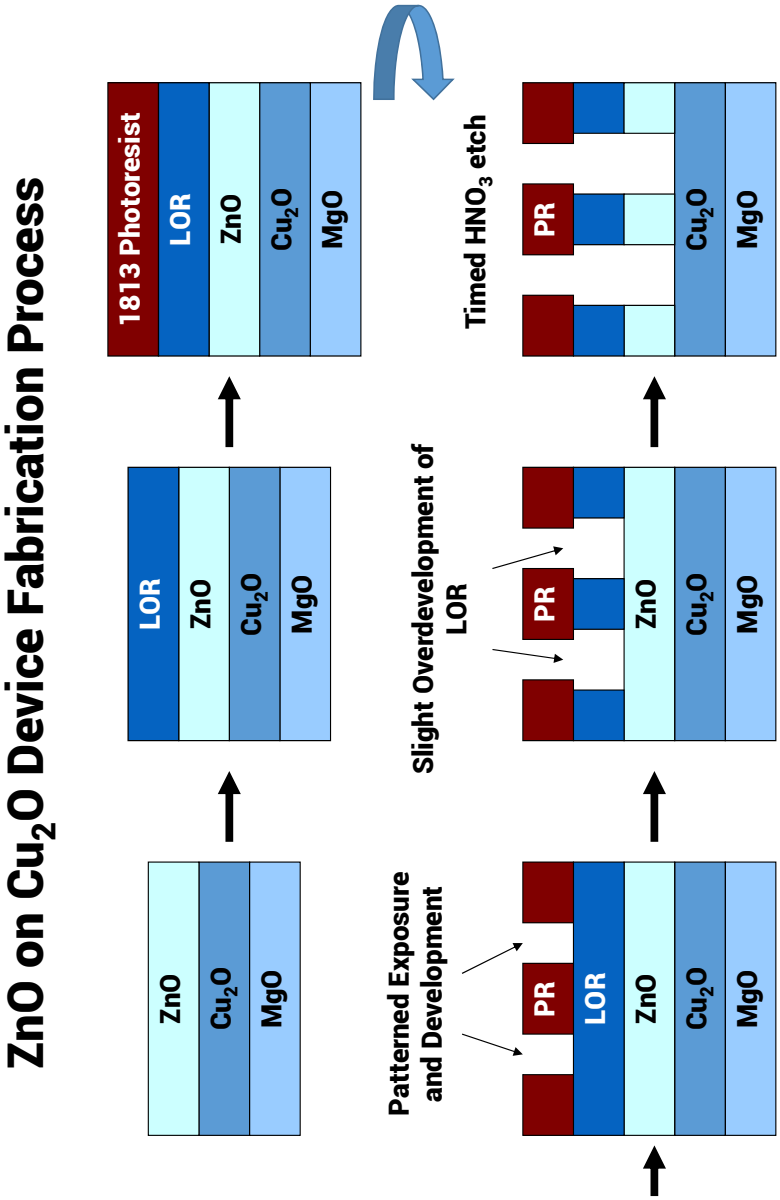

ZnO on Cu_2O Device Fabrication Process

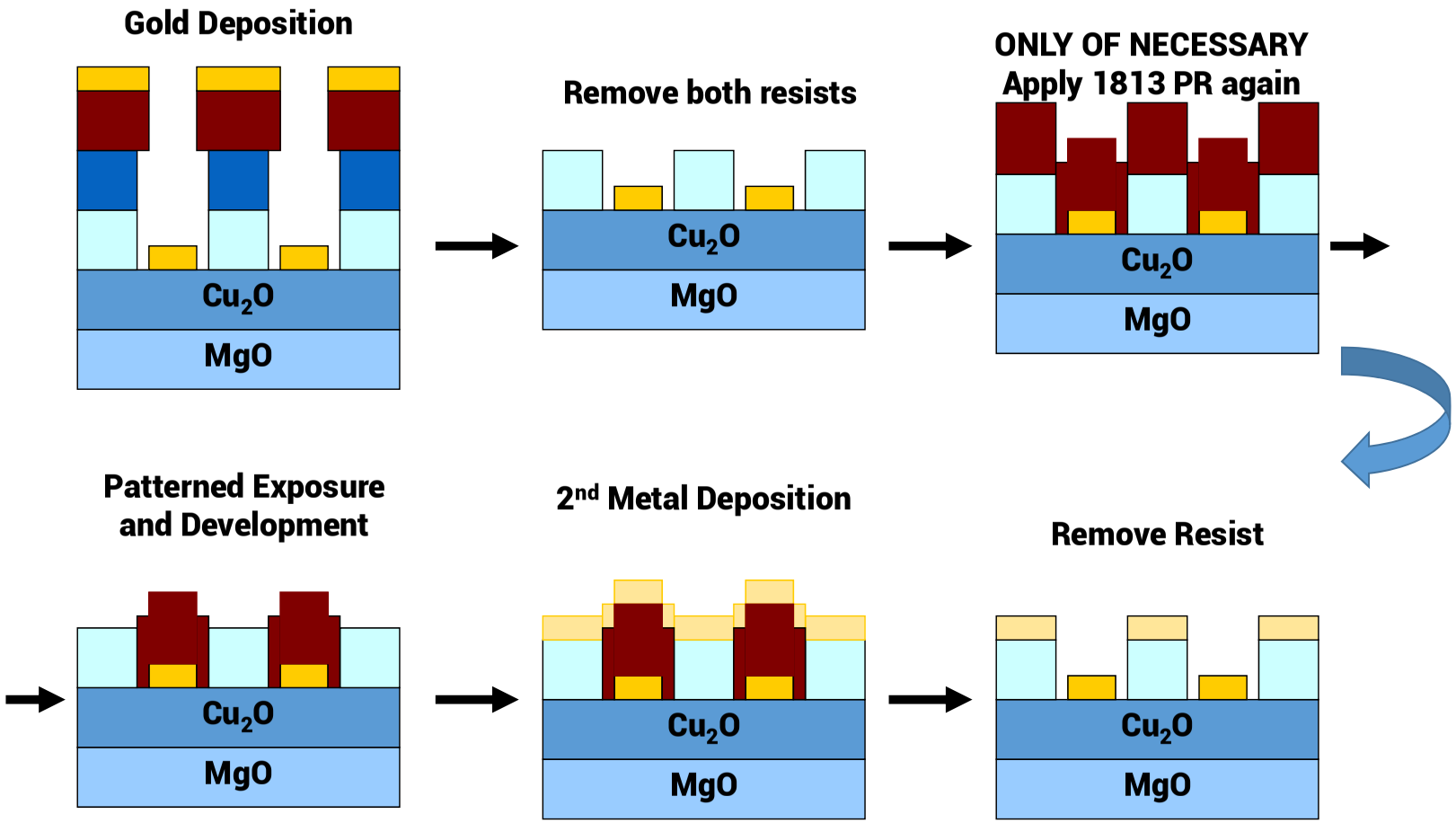

Appendix C

AFORS-Het

simulation hetero
printed at 12/13/2012

results:
Voc=691.4 mV Jsc=11.24 mA/cm^2 FF=58.75 % Eff=4.566 %

working conditions:

calculation mode: dc
T: 300 K temperature
/illumination
illumination side: front
spectral illumination: on
spectral file: AM15.in lambda[nm],flux[1/(cm^2*s*nm)]
i_spectral: 1 spectral intensity factor
monochromatic illumination: off
/end of illumination
fix potential at: front
v_ext: 0 V boundary external voltage
j_ext: 0 A/cm^2 external current
/end of working conditions

cell parameter:

/general parameters
Rs: 17 Ohm*cm^2 serial resistance
MISf: 17 Ohm*cm^2 fraqtion
initialvaluesfromfile: false
initialgridfromfile: false
/end of general parameters

/layer
name: vacuum/air
width: 1E-6 cm layer thickness
incoherent: false incoherent calculation
n: 1 optical coefficient n
k: 0 optical coefficient k
/end of layer

/layer
name: ZnO
width: 1E-5 cm layer thickness
incoherent: false incoherent calculation
nk-file: ZnO_thinfilm.nk lambda[nm],n[-],k[-]
/end of layer

/frontcontact
name: Frontcontact
BandBending: Band-bending
phi: 4.23 eV metal work function
ref: 0 constant reflection
abs: 0 constant absorption
int_ref: 0 constant internal reflection
/end of frontcontact

/interface
interfacename: Schottky interface Sn1e7 Sp1
numeric-model: 0 MS-Schottky-Contact
/modelparameters
model-name: MS-Schottky-Contact
sn: 100000 cm/s electron surface recombination velocity
sp: 100000 cm/s hole surface recombination velocity
/end of modelparameters
Qif: 0 cm^-3 Interface Charge

no defects
/end of interface

/layer
name: Cu2O
numeric-model: 0 standard
functional_dependance: Constant
xd_dk: 1E99
xd_chi: 1E99
xd_Eg: 1E99
xd_Egopt: 1E99
xd_Nc: 1E99
xd_Nv: 1E99

xd_me: 1E99
xd_mh: 1E99
xd_Na: 1E99
xd_Nd: 1E99
xd_ve: 1E99
xd_vh: 1E99
xd_rho: 1E99
xd_rae: 1E99
xd_rah: 1E99
xd_rbb: 1E99
decr_type: rightside
xD: 0.05
width: 0.005 cm layer thickness
dk: 7.2 dielectric constant
chi: 3.3 eV electron affinity
Eg: 2.05 eV bandgap
Egopt: 2.05 eV optical bandgap
Nc: 2.44E19 cm^-3 effective conduction band density
Nv: 1.104E19 cm^-3 effective valence band density
me: 110 cm^2/Vs effective electron mobility
mh: 65 cm^2/Vs effective hole mobility
Na: 10000000000000 cm^-3 doping concentration acceptors
Nd: 50000000000 cm^-3 doping concentration donators
ve: 67920 cm/s electron thermal velocity
vh: 88520 cm/s hole thermal velocity
rho: 6.09 g*cm^-3 layer density
rae: 2.2E-31 cm^6/s auger electron recombination coefficient
rah: 9.9E-32 cm^6/s auger hole recombination coefficient
rbb: 1E-10 cm^3/s band to band recombination coefficient
nk-file: GregNewCu2O.nk lambda[nm],n[-],k[-]
incoherent: false incoherent calculation

/defect
name: Defect_1
text: Cu Vacancy
type: single
charge: acceptor
hurkx: off
cn: 1E-9 cm^2 electron thermal cross section
cp: 1E-9 cm^2 hole thermal cross section
meff: 0.25 cm^2 efective tunneling mass
cnplus: 1E-12 cm^2 electron thermal cross section
cpminus: 1E-12 cm^2 hole thermal cross section
cnzero: 1E-15 cm^2 electron thermal cross section
cpzero: 1E-15 cm^2 hole thermal cross section
cno: 0 cm^2 electron optical cross section
cpo: 0 cm^2 hole optical cross section
Ntr: 10000000000000 cm^-3 trap density
E: 0.45 eV characteristic energy
Ntr specific: 10000000000000 cm^-3/eV specific trap density
Taun: 1.47232037691402E-9 s mean electron lifetime
Taup: 1.47232037691402E-9 s mean hole lifetime
Ln: 6.4706037271029E-5 cm mean electron diffusion length
Lp: 4.97399265137983E-5 cm mean hole diffusion length
/end of defect

/defect
name: Defect_2
text: Cu Di Vacancy
type: single
charge: acceptor
hurkx: off
cn: 1E-15 cm^2 electron thermal cross section
cp: 1E-15 cm^2 hole thermal cross section
meff: 0.25 cm^2 efective tunneling mass
cnplus: 1E-12 cm^2 electron thermal cross section
cpminus: 1E-12 cm^2 hole thermal cross section
cnzero: 1E-15 cm^2 electron thermal cross section
cpzero: 1E-15 cm^2 hole thermal cross section
cno: 0 cm^2 electron optical cross section
cpo: 0 cm^2 hole optical cross section
Ntr: 4E16 cm^-3 trap density
E: 0.25 eV characteristic energy
Ntr specific: 4E16 cm^-3/eV specific trap density
Taun: 3.68080094228504E-7 s mean electron lifetime
Taup: 3.68080094228504E-7 s mean hole lifetime
Ln: 0.00102309228070099 cm mean electron diffusion length
Lp: 0.000786457292165006 cm mean hole diffusion length
/end of defect

/defect

name: Defect_3
text: Oxygen Vac
type: single
charge: donor
hurkx: off
cn: 1E-15 cm^2 electron thermal cross section
cp: 1E-15 cm^2 hole thermal cross section
meff: 0.25 cm^2 efective tunneling mass
cnplus: 1E-12 cm^2 electron thermal cross section
cpminus: 1E-12 cm^2 hole thermal cross section
cnzero: 1E-15 cm^2 electron thermal cross section
cpzero: 1E-15 cm^2 hole thermal cross section
cno: 0 cm^2 electron optical cross section
cpo: 0 cm^2 hole optical cross section
Ntr: 100000000000000 cm^-3 trap density
E: 0.91 eV characteristic energy
Ntr specific: 100000000000000 cm^-3/eV specific trap density
Taun: 0.000147232037691402 s mean electron lifetime
Taup: 0.000147232037691402 s mean hole lifetime
Ln: 0.0204618456140197 cm mean electron diffusion length
Lp: 0.0157291458433001 cm mean hole diffusion length
/end of defect
/end of layer

/interfacebackside
interfacename: Interface back
numeric-model: 0 MS-Schottky-Contact
/modelparameters
model-name: MS-Schottky-Contact
sn: 10000000 cm/s electron surface recombination velocity
sp: 10000000 cm/s hole surface recombination velocity
/end of modelparameters
Qif: 0 cm^-3 Interface Charge

no defects
/end of interface

/backcontact
name: Backcontact
BandBending: Flat-band
ref: 0 constant reflection
abs: 0 constant absorption
int_ref: 0 constant internal reflection
/end of backcontact

/layer
name: vacuum/air
width: 1E-6 cm layer thickness
incoherent: false incoherent calculation
n: 1 optical coefficient n
k: 0 optical coefficient k
/end of layer

/end of all layers

Bibliography

[1] Simon R. Bare and G.A. Somorjai. Surface chemistry. In Editor in Chief: Robert A. Meyers, editor, *Encyclopedia of Physical Science and Technology (Third Edition)*, pages 373 – 421. Academic Press, New York, third edition edition, 2003. ISBN 978-0-12-227410-7. doi: 10.1016/B0-12-227410-5/00757-2. URL http://www.sciencedirect.com/science/article/pii/B0122274105007572. viii, 46

[2] James M. Lafferty. Vacuum technology. In Editor in Chief: Robert A. Meyers, editor, *Encyclopedia of Physical Science and Technology (Third Edition)*, pages 385 – 410. Academic Press, New York, third edition edition, 2003. ISBN 978-0-12-227410-7. doi: 10.1016/B0-12-227410-5/00806-1. URL http://www.sciencedirect.com/science/article/pii/B0122274105008061. viii, 46

[3] J.B. Grotberg. Dynamics of gas flow and pressureflow relationships. In Geoffrey J. Laurent and Steven D. Shapiro, editors, *Encyclopedia of Respiratory Medicine*, pages 59 – 64. Academic Press, Oxford, 2006. ISBN 978-0-12-370879-3. doi: 10.1016/B0-12-370879-6/00510-X. URL http://www.sciencedirect.com/science/article/pii/B012370879600510X. viii, 46

[4] K. Alavi. Molecular beam epitaxy. In Editors in Chief: K. H. Jrgen Buschow, Robert W. Cahn, Merton C. Flemings, Bernard Ilschner (print), Edward J. Kramer, Subhash Mahajan, , and Patrick Veyssire

(updates), editors, *Encyclopedia of Materials: Science and Technology (Second Edition)*, pages 5765 – 5780. Elsevier, Oxford, second edition edition, 2001. ISBN 978-0-08-043152-9. doi: 10.1016/B0-08-043152-6/01002-0. URL http://www.sciencedirect.com/science/article/pii/B0080431526010020. viii, 48

[5] Mark Yeadon and J.Murray Gibson. Molecular beam epitaxy, semiconductors. In Editor in Chief: Robert A. Meyers, editor, *Encyclopedia of Physical Science and Technology (Third Edition)*, pages 113 – 121. Academic Press, New York, third edition edition, 2003. ISBN 978-0-12-227410-7. doi: 10.1016/B0-12-227410-5/00457-9. URL http://www.sciencedirect.com/science/article/pii/B0122274105004579. viii, 48

[6] M. Peressi. Semiconductor heterojunctions, electronic properties of. In Editors in Chief: Franco Bassani, Gerald L. Liedl, , and Peter Wyder, editors, *Encyclopedia of Condensed Matter Physics*, pages 273 – 281. Elsevier, Oxford, 2005. ISBN 978-0-12-369401-0. doi: 10.1016/B0-12-369401-9/01136-0. URL http://www.sciencedirect.com/science/article/pii/B0123694019011360. viii, 48

[7] P. Frigeri, L. Seravalli, G. Trevisi, and S. Franchi. 3.12 - molecular beam epitaxy: An overview. In Editors in Chief:Pallab Bhattacharya, Roberto Fornari, , and Hiroshi Kamimura, editors, *Comprehensive Semiconductor Science and Technology*, pages 480 – 522. Elsevier, Amsterdam, 2011. ISBN 978-0-444-53153-7. doi: 10.1016/B978-0-44-453153-7.00099-7. URL http://www.sciencedirect.com/science/article/pii/B9780444531537000997. viii, 48

[8] A. Bakin and A. Waag. 3.10 - zno epitaxial growth. In Editors in Chief:Pallab Bhattacharya, Roberto Fornari, , and Hiroshi Kamimura, editors, *Comprehensive Semiconductor Science and Technology*, pages

368 – 395. Elsevier, Amsterdam, 2011. ISBN 978-0-444-53153-7. doi: 10.1016/B978-0-44-453153-7.00102-4. URL http://www.sciencedirect.com/science/article/pii/B9780444531537001024. viii, 48

[9] Xiliang Nie, Su-Huai Wei, and S. B. Zhang. First-principles study of transparent p -type conductive srcu$_2$o$_2$ and related compounds. *Phys. Rev. B*, 65:075111, Jan 2002. doi: 10.1103/PhysRevB.65.075111. URL http://link.aps.org/doi/10.1103/PhysRevB.65.075111. ix, 9, 10, 11

[10] F. Biccari. *Defects and doping in Cu_2O*. PhD thesis, University of Roma, Italy, 2009. ix, 17

[11] M.L. Foo, Q. Huang, J.W. Lynn, Wei-Li Lee, Tomasz Klimczuk, I.S. Hagemann, N.P. Ong, and R.J. Cava. Synthesis, structure and physical properties of ru ferrites: Bamru5o11 (m=li and cu) and bam2ru4o11 (m=mn, fe and co). *Journal of Solid State Chemistry*, 179(2):563 – 572, 2006. ISSN 0022-4596. doi: 10.1016/j.jssc.2005.11.014. URL http://www.sciencedirect.com/science/article/pii/S0022459605005396. xiii, 7, 8

[12] A. H. Pfund. The light sensitiveness of copper oxide. *Phys. Rev.*, 7:289–301, Mar 1916. doi: 10.1103/PhysRev.7.289. URL http://link.aps.org/doi/10.1103/PhysRev.7.289. 1

[13] L. O. Grondahl. The copper-cuprous-oxide rectifier and photoelectric cell. *Rev. Mod. Phys.*, 5:141–168, Apr 1933. doi: 10.1103/RevModPhys.5.141. URL http://link.aps.org/doi/10.1103/RevModPhys.5.141. 2

[14] L. C. Olsen, F. W. Addis, and W. Miller. Experimental and theoretical studies of cu2o solar cells. *Solar Cells*, 7(3):247–279, 1982. 5, 40

[15] Tadatsugu Minami, Yuki Nishi, Toshihiro Miyata, and Jun-ichi Nomoto. High-efficiency oxide solar cells with zno/cu2o heterojunction fabricated on thermally oxidized cu2o sheets. *Applied Physics Express*, 4:062301, 2011. 5

[16] Bodie Douglas and Shih-Ming Ho. *Structure and Chemistry of Crystalline Solids*. SpringerLink, 2007. 7

[17] A. Werner and H. D. Hochheimer. High-pressure x-ray study of cu_2o and ag_2o. *Phys. Rev. B*, 25:5929–5934, May 1982. doi: 10.1103/PhysRevB.25.5929. URL http://link.aps.org/doi/10.1103/PhysRevB.25.5929. 7, 8

[18] Davis S. Darvish and Harry A. Atwater. Epitaxial growth of cu2o and zno/cu2o thin films on mgo by plasma-assisted molecular beam epitaxy. *Journal of Crystal Growth*, 319(1):39–43, 2011. 7

[19] R. J. Elliott. Symmetry of excitons in cu_2o. *Phys. Rev.*, 124:340–345, Oct 1961. doi: 10.1103/PhysRev.124.340. URL http://link.aps.org/doi/10.1103/PhysRev.124.340. 9

[20] M. M. Beg and S. M. Shapiro. Study of phonon dispersion relations in cuprous oxide by inelastic neutron scattering. *Phys. Rev. B*, 13:1728–1734, Feb 1976. doi: 10.1103/PhysRevB.13.1728. URL http://link.aps.org/doi/10.1103/PhysRevB.13.1728. 9

[21] Ch. Uihlein, D. Fröhlich, and R. Kenklies. Investigation of exciton fine structure in cu_2o. *Phys. Rev. B*, 23:2731–2740, Mar 1981. doi: 10.1103/PhysRevB.23.2731. URL http://link.aps.org/doi/10.1103/PhysRevB.23.2731. 9

[22] P. Hohenberg and W. Kohn. Inhomogeneous electron gas. *Phys. Rev.*, 136:B864–B871, Nov 1964. doi: 10.1103/PhysRev.136.B864. URL http://link.aps.org/doi/10.1103/PhysRev.136.B864. 9

[23] W. Kohn and L. J. Sham. Self-consistent equations including exchange and correlation effects. *Phys. Rev.*, 140:A1133–A1138, Nov 1965. doi: 10.1103/PhysRev.140.A1133. URL http://link.aps.org/doi/10.1103/PhysRev.140.A1133. 9

[24] J W Hodby, T E Jenkins, C Schwab, H Tamura, and D Trivich. Cyclotron resonance of electrons and of holes in cuprous oxide, cu 2 o. *Journal of Physics C: Solid State Physics*, 9(8):1429, 1976. URL http://stacks.iop.org/0022-3719/9/i=8/a=014. 13, 20

[25] M. Zouaghi, M. Tapiero, J.P. Zielinger, and R. Burgraf. Hall mobility and hole density in photoactivated cu2o single crystals. *Solid State Communications*, 8(22):1823 – 1825, 1970. ISSN 0038-1098. doi: 10.1016/0038-1098(70)90325-X. URL http://www.sciencedirect.com/science/article/pii/003810987090325X. 13

[26] R. Kuzel and F. L. Weichman. Surface and bulk conductivities of cu[sub 2]o single crystals. *Journal of Applied Physics*, 41(1):271–279, 1970. doi: 10.1063/1.1658333. URL http://link.aip.org/link/?JAP/41/271/1. 13

[27] Stephen James Angello. Hall effect and conductivity of cuprous oxide. *Phys. Rev.*, 62:371–377, Oct 1942. doi: 10.1103/PhysRev.62.371. URL http://link.aps.org/doi/10.1103/PhysRev.62.371. 13

[28] Josef Pastrk and Radomr Kuel. The influence of illumination on the conductivity and photo-conductivity of cu₂o. *Czechoslovak Journal of Physics*, 6:235–236, 1956. ISSN 0011-4626. URL http://dx.doi.org/10.1007/BF01687731. 10.1007/BF01687731. 13

[29] Hiroshi Shimada and Taizo Masumi. Hall mobility of positive holes in cu_2o. *Journal of the Physical Society of Japan*, 58(5):1717–1724, 1989. doi: 10.1143/JPSJ.58.1717. URL http://jpsj.ipap.jp/link?JPSJ/58/1717/. 13

[30] V. T. Agekyan, I. P. Kuz'mina, A. N. Lobachev, B. S. Predtechenskii, L. S. Starostina, and N. M. Khaidukov. Optical properties of cuprous oxide crystals grown by various methods. *Journal of Applied Spectroscopy*, 22:562–566, 1975. ISSN 0021-9037. URL http://dx.doi.org/10.1007/BF00614717. 10.1007/BF00614717. 14

[31] M.T. Clavaguera-Mora, J.L. Touron, J. Rodr?guez-Viejo, and N. Clavaguera. Thermodynamic description of the cuo system. *Journal of Alloys and Compounds*, 377(12):8 – 16, 2004. ISSN 0925-8388. doi: 10.1016/j.jallcom.2004.01.031. URL http://www.sciencedirect.com/science/article/pii/S0925838804000817. 15

[32] Sanjeev Aggarwal, Jrg Tpfer, Tse-Lun Tsai, and Rdiger Dieckmann. Point defects and transport in binary and ternary, non-stoichiometric oxides. Volumes 101103:321331, 1997. 17

[33] Rdiger Dieckmann. Point defects and transport in non-stoichiometric oxides: Solved and unsolved problems. 59(4):507525, 1998. 17

[34] Kouji Mimura, Jae-Won Lim, Minoru Isshiki, Yongfu Zhu, and Qing Jiang. Brief review of oxidation kinetics of copper at 350 c to 1050 c. *Metallurgical and Materials Transactions A*, 37:1231–1237, 2006. ISSN 1073-5623. doi: 10.1007/s11661-006-1074-y. URL http://dx.doi.org/10.1007/s11661-006-1074-y. 18

[35] Colleen M. McShane, Withana P. Siripala, and Kyoung-Shin Choi. Effect of junction morphology on the performance of polycrystalline cu2o homojunction solar cells. *The Journal of Physical Chemistry Letters*, 1(18):2666–2670, 2010. doi: 10.1021/jz100991e. URL http://pubs.acs.org/doi/abs/10.1021/jz100991e. 18

[36] Aloysius Soon, Xiang-Yuan Cui, Bernard Delley, Su-Huai Wei, and Catherine Stampfl. Native defect-induced multifarious magnetism in nonstoichiometric cuprous oxide: First-principles study of bulk and surface properties of cu_2-δO. *Phys. Rev. B*, 79 : 035205, *Jan*2009. *doi* :10.1103/PhysRevB.79.035205. URL http://link.aps.org/doi/10.1103/PhysRevB.79.035205. 18

[37] Alberto Mittiga, Enrico Salza, Francesca Sarto, Mario Tucci, and Rajaraman Vasanthi. Heterojunction solar cell with 2substrate. *Applied Physics Letters*, 88 (16):163502–2, 2006. 20, 37, 73

[38] Yukiko Ebisuzaki. Preparation of monocrystalline cuprous oxide. *Journal of Applied Physics*, 32(10):2027–2028, 1961. 10.1063/1.1728282. URL http://link.aip.org/link/?JAP/32/2027/1. 20

[39] Tomoyasu Nakano, Kazumasa Ohtani, Akira Kinoshita, and Tuneo Okuda. Growth of cuprous oxide (cu_2o) crystal. *Japanese Journal of Applied Physics*, 3(2):124–124, 1964. 10.1143/JJAP.3.124. URL http://jjap.jsap.jp/link?JJAP/3/124/. 20

[40] J. Katayama, K. Ito, M. Matsuoka, and J. Tamaki. Performance of Cu 2 O/ZnO Solar Cell Prepared By Two-Step Electrodeposition. *Journal of Applied Electrochemistry*, 34(7):687–692, July 2004. ISSN 0021-891X. 10.1023/B:JACH.0000031166.7366 URL http://link.springer.com/article/10.1023/B%3AJACH.0000031166.73660.c1. 20, 21

[41] W. Siripala, L.D.R.D. Perera, K.T.L. De Silva, J.K.D.S. Jayanetti, and I.M. Dharmadasa. Study of annealing effects of cuprous oxide grown by electrodeposition technique. *Solar Energy Materials and Solar Cells*, 44(3):251 – 260, 1996. ISSN 0927-0248. 10.1016/0927-0248(96)00043-8. URL http://www.sciencedirect.com/science/article/pii/0927024896000438. 20, 21

[42] S. Ishizuka, K. Suzuki, Y. Okamoto, M. Yanagita, T. Sakurai, K. Akimoto, N. Fujiwara, H. Kobayashi, K. Matsubara, and S. Niki. Polycrystalline n-zno/p-cu2o heterojunctions grown by rf-magnetron sputtering. *physica status solidi (c)*, 1(4):1067–1070, 2004. 20

[43] J.F. Pierson, A. Thobor-Keck, and A. Billard. Cuprite, paramelaconite and tenorite films deposited by reactive magnetron sputtering. *Applied Surface Science*, 210(34):359 – 367, 2003. ISSN 0169-4332. 10.1016/S0169-4332(03)00108-9. URL http://www.sciencedirect.com/science/article/pii/S0169433203001089. 20

[44] Akira Kinoshita and Tomoyasu Nakano. Cu_2o crystal growth by hydrothermal

technique. *Japanese Journal of Applied Physics*, 6(5):656–657, 1967. 10.1143/JJAP.6.656. URL http://jjap.jsap.jp/link?JJAP/6/656/. 20

[45] S.S. Jeong, A. Mittiga, E. Salza, A. Masci, and S. Passerini. Electrodeposited zno/cu2o heterojunction solar cells. *Electrochimica Acta*, 53(5):2226 – 2231, 2008. ISSN 0013-4686. 10.1016/j.electacta.2007.09.030. URL http://www.sciencedirect.com/science/article/pii/S0013468607011723. 21

[46] William Shockley and Hans J. Queisser. Detailed balance limit of efficiency of p-n junction solar cells. *Journal of Applied Physics*, 32(3):510–519, 1961. 10.1063/1.1736034. URL http://link.aip.org/link/?JAP/32/510/1. 24

[47] C. H. Henry. Limiting efficiencies of ideal single and multiple energy gap terrestrial solar cells. *Journal of Applied Physics*, 51(8):4494–4500, 1980. 10.1063/1.328272. URL http://link.aip.org/link/?JAP/51/4494/1. 25, 30

[48] L. Wang and et al. Simulation of high efficiency heterojunction solar cells with afors-het. In *Journal of Physics: Conference Series, vol. 276, p. 012177*, 2011. 30

[49] Chengxiang Xiang, Gregory M. Kimball, Ronald L. Grimm, Bruce S. Brunschwig, Harry A. Atwater, and Nathan S. Lewis. 820 mv open-circuit voltages from cu2o/ch3cn junctions. *Energy & Environmental Science*, 4(4):1311–1318, 2011. 39

[50] K. Jacobi, G. Zwicker, and A. Gutmann. Work function, electron affinity and band bending of zinc oxide surfaces. *Surface Science*, 141(1):109–125, 1984. 40

[51] R. Brewer. Rapid biaxial texture development during nucleation of mgo thin films during ion beam-assisted deposition. *Appl. Phys. Lett.*, 80(18):3388, 2002. 52

[52] D. Schmitt, P. Morin, and J. Pierre. Magnetic structure and crystal field in cerium compounds with cscl-type structure. *Journal of Magnetism and Magnetic*

Materials, 8(3):249 – 256, 1978. ISSN 0304-8853. 10.1016/0304-8853(78)90128-2. URL http://www.sciencedirect.com/science/article/pii/0304885378901282. 61

[53] V Ganesan and KS Girirajan. Lattice parameter and thermal expansion of cscl and csbr by x-ray powder diffraction. ii. thermal expansion of csbr from room temperature to 78.2 k. *Pramana*, 27:475–478, 1986. ISSN 0304-4289. 10.1007/BF02846873. URL http://dx.doi.org/10.1007/BF02846873. 61

[54] A.O Musa, T Akomolafe, and M.J Carter. Production of cuprous oxide, a solar cell material, by thermal oxidation and a study of its physical and electrical properties. *Solar Energy Materials and Solar Cells*, 51(34):305 – 316, 1998. ISSN 0927-0248. 10.1016/S0927-0248(97)00233-X. URL http://www.sciencedirect.com/science/article/pii/S092702489700233X. 73

[55] D. Trivich. Cuprous oxide photovoltaic cells (final report). Technical Report DOE/ET/23010T10,, Department of Chemistry, Wayne State University,, 1981. 73

[56] Yoed Tsur and Ilan Riess. Doping of ionic compounds: solubility limit and self-compensation. *Solid State Ionics*, 119(14):37 – 42, 1999. ISSN 0167-2738. 10.1016/S0167-2738(98)00480-9. URL http://www.sciencedirect.com/science/article/pii/S0167273898004809. 73

[57] U. Rau and H.W. Schock. Electronic properties of cu(in,ga)se2 heterojunction solar cellsrecent achievements, current understanding, and future challenges. *Applied Physics A*, 69:131–147, 1999. ISSN 0947-8396. 10.1007/s003390050984. URL http://dx.doi.org/10.1007/s003390050984. 73

[58] Rana N. S. Sodhi. Time-of-flight secondary ion mass spectrometry (tof-sims):-versatility in chemical and imaging surface analysis. *Analyst*, 129 Issue 6:483–487, 2004. 74

[59] Helmut Paul. *The Stopping Power of Matter for Positive Ions, Modern Practices in Radiation Therapy*. InTech, 2012. 75

[60] N. Toyoda. Ultra-smooth surface preparation with gas cluster ion beams. In *Microprocesses and Nanotechnology Conference, 2001 International*, 2001. 78

[61] J. D. Klein, A. Yen, and S. L. Clauson. Ion beam sputtering of in situ superconducting y-ba-cu-o films. *Journal of Applied Physics*, 67(10):6389–6393, 1990. 10.1063/1.345161. URL http://link.aip.org/link/?JAP/67/6389/1. 78

[62] Hideyuki Takahashi, Ayako Sato, Masaru Takakura, Norihisa Mori, Juergen Boerder, Walter Knoll, and John Critchell. A new method of surface preparation for high spatial resolution epma/sem with an argon ion beam. *Microchimica Acta*, 155:295–300, 2006. ISSN 0026-3672. 10.1007/s00604-006-0559-0. URL http://dx.doi.org/10.1007/s00604-006-0559-0. 78

[63] D. Q. Shi, M. Ionescu, J. McKinnon, W. M. Chen, and S. X. Dou. Research of surface-oxidation epitaxy of nio films on cube textured ni tapes. *AIP Conference Proceedings*, 614(1):525–530, 2002. 78